A Computational Study of the Earth's Lower Mantle Thermal Structure and Composition

A THESIS
SUBMITTED TO THE FACULTY OF THE GRADUATE SCHOOL
OF THE UNIVERSITY OF MINNESOTA
BY

Juan José Valencia Cardona

IN PARTIAL FULFILLMENT OF THE REQUIREMENTS
FOR THE DEGREE OF
Doctor of Philosophy

Renata M. Wentzcovitch

May, 2018

Acknowledgements

I want start by thanking my adviser, Prof. Renata M. Wentzcovitch, for her support and guidance. Her passion for research was fundamental to achieve the goals of this study. Also, thank you to my committee members: Prof. Perry Leo, Prof. Ryan Elliott, and Prof. David Yuen, for their help, comments, and suggestions. Thank you to Jan Morse, Prof. Christopher Cramer, Prof. Perry Leo, and Prof. Victor Barocas for their help and advise during difficult times.

I want to thank my lab colleagues: Dr. Gaurav Shukla, Dr. Kanchan Sarkar, Dr. Michel Marcondes, Dr. Pedro da Silveira, Dr. Joelson Cott, Dr. Mehmet Topsakal, and Tian Qin, for their friendship and eagerness to discuss and help me with important research aspects. Special thanks to Dr. Gaurav Shukla, from whom I learned a great deal of the fundamentals in mineral physics and thermodynamics of materials. His collaboration was key to obtain the results shown in this work. I would also like to thank Prof. Quentin Williams (UCSC), Prof. Zhongqing Wu (USTC), and Prof. Christine Houser (ELSI-TIT), for their collaboration, guidance, and ideas.

During my stay in Minnesota I had the chance to meet amazing people, which always lent me their hand during difficult times and made graduate school an enjoyable experience. Thank you to: Vivek Dabade, Savio Poovathingal, Karthik Ginnavaram, Shaokai Zheng, John Kohler, Kevin Sebesta, Carlos Garavito, David Escobar, Claudia Moreno, Christian Perea, and Andres Acosta. Also, thank you to my wonderful partner, Catalina Luna. Her love and support always kept me motivated.

I want to thank my previous advisers at National University of Colombia - Manizales: Prof. Andres Rosales-Rivera, Prof. Oscar H. Giraldo, and Prof. Nayda Arias-Duque. Their insights, guidance, and advise, have always been essential for my academic and personal development.

Thank you to all my family and friends. Thank to my aunt and uncle Martha and Jerry Peterson. Their fatherly love and unconditional support always made me feel as if I was never away from home. Thank you to my uncle, Douglas Caro-Olaya (1956-2014). An outstanding father and brilliant individual who always encouraged my interest in science. Thank you to my grandpa, Pedro N. Valencia (1918-1996). My first math teacher and life hero. Thank you to my mother: Marleny Valencia-Cardona. Her bravery and determination to overcome difficulties in life will always be my greatest motivation.

This work was supported primarily by grants NSF/EAR 1319368 and NSF/EAR 1348066. Computations were performed at the Minnesota Supercomputing Institute (MSI).

Dedication

To my mother. An example of love, discipline, bravery, and perseverance. Muchas gracias, mamá!

Abstract

An enhanced determination of the internal dynamic processes that take place in our planet's interior could be achieved if its composition and thermal structure are well resolved. However, its extreme pressure and temperature conditions make this task a grand challenge in the geophysical sciences. Alternate methods of study are required to overcome such physical constraints. In this work, we use the thermoelastic properties of various minerals, computed from *ab initio* calculations, to study the composition and thermal structure of the Earth's lower mantle. The mineral phases of this region of the Earth are: (Fe, Al)-bearing $MgSiO_3$ bridgmanite, (Fe, Al)-bearing $MgSiO_3$ post-perovskite, (Mg, Fe)O ferropericlase, and $CaSiO_3$ perovskite. The thermoelastic properties of different lower mantle aggregates are computed by varying the molar concentration of these mineral phases, whose seismic velocities and densities are compared to one-dimensional seismic models, for validation, along their self-consistent temperature gradient. We particularly focus on the effect of a pressure-induced reordering of the electronic structure of Fe in ferropericlase, known as spin-crossover, on the temperature profile of the lower mantle. The anomalous behavior caused by spin-crossover has not been observed in one-dimensional seismic studies. Thus, we present a novel way to achieve this by using a common seismic observable known as the Bullen's parameter. Finally, we study the seismic and thermodynamic signatures of a major phase transition, bridgmanite to post-perovskite, which are of vital importance to shed light on the enigmatic behavior of the deep lower mantle, otherwise known as the D" region.

Contents

List of Tables

List of Figures

Chapter 1

Introduction

Astronomical observations allows us to understand and unravel planetary bodies' features such as their mass, size, and moment of inertia. For instance, from a planet's gravitational field, we can infer its mass distribution, while from its magnetic field, information about the metallic core. Furthermore, spectroscopic observations can be used to determine the abundances of the different chemical elements as well as the chemical differentiation, during the accretion processes, to which a particular planet undergoes from the nebula [3]. The latter is important because knowledge about a planet's composition broadens our understanding of its internal dynamics and evolution. However, finding the composition of a planet poses significant challenges in most of the studies in geological sciences, because of the demand of evaluating materials properties in extreme conditions: Temperatures that can be hotter than the surface of the sun, and pressures that can go over two million times the ambient pressure.

The schematic shown in Figure 1.1 depicts how the Earth is compositionally divided into different layers. The most accessible layer is the Earth's outer solid shell (not shown in Figure 1.1) known as the crust, which can be continental or oceanic. The continental crust has a thickness of ~ 100 km and can be compositionally heterogeneous, while the oceanic is more uniform with a lower thickness of ~ 10 km. Then comes the upper mantle. This layer spans up to a depth of ~ 410 km and various minerals such as olivine (Ol), garnet (Gt), and pyroxenes (Px) can be found here. At 410 km in depth, we reach the so-called transition zone. Here, an isochemical phase change dominated by $(\mathrm{Mg}, \mathrm{Fe})_2\mathrm{SiO}_4$ olivine occurs: Olivine (α spinel) becomes wadsleyite (β spinel) and wadsleyite, at 520 km depth, transforms into ringwoodite (γ spinel). Lastly, at 660 km, Mg_2SiO_4 ringwoodite becomes unstable and dissociates into $MgSiO_3$ + MgO. This phenomenon is reflected in seismic discontinuities that will be discussed later.

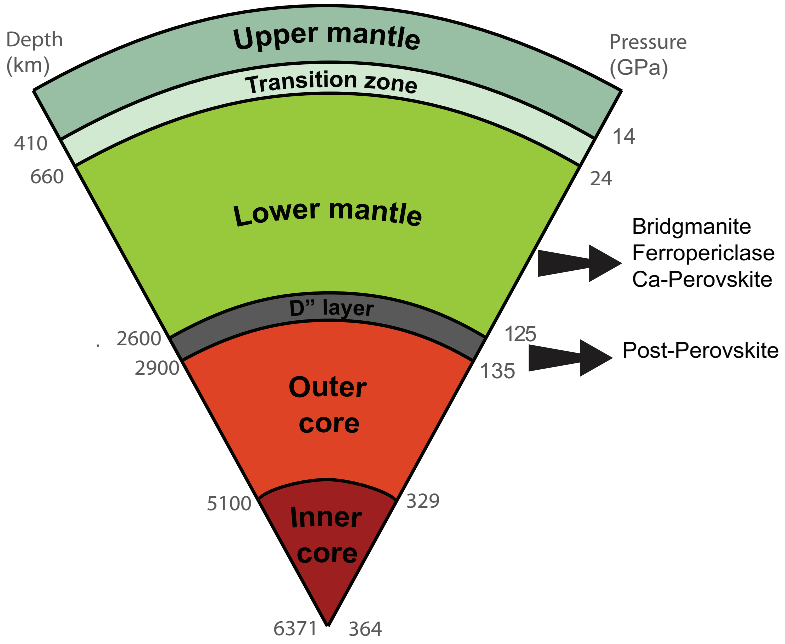

Figure 1.1: Schematic of the compositionally divided Earth.

We now move into the lower mantle, which spans from 660 km to 2900 km. Three major mineral phases are believed to be found in here: (Al, Fe)- $MgSiO_3$ bridgmanite (bdg), $CaSiO_3$ perovskite (CaPv), and (Mg, Fe)O ferropericlase (fp) [47,49,71]. Furthermore, at a depth of $\sim$ 2600 km, bdg becomes unstable and goes from its perovskite phase to a lamellar phase known as post-perovskite. This is a characteristic feature of the D" region, which is located 300 km above the core mantle boundary (CMB). Consequences on seismic observables and thermodynamic properties due to the post-perovskite phase transition are discussed in better detail in chapter 5. Moreover, information on the mineral phases and lower mantle rocks are discussed in chapters 2 and 3. After the lower mantle, we reach the core (outer and inner core). The liquid outer core is believed to be a mixture of Fe and Ni along with one or more light elements (Si, O, H, K, C, S), while the inner core is a solid sphere, mainly made of pure Fe. After this brief compositional review of the planet, the question that follows is: How do we study the thermoelastic properties of our planet's interior? Because of the extreme conditions of the Earths interior, direct sampling of mantle rocks with our current technology is nearly impossible and demands alternative methods of study. The first method in our list is seismological observations, where images of the mantle are constructed from the velocities of the waves recorded from earthquakes and controlled explosions. Discontinuities in the recorded velocities indicate at which depths the rocks and minerals are changing their morphology. The second method is to recreate the lower mantle temperature and pressure conditions in the lab, and examine the crystal structure of the rocks and minerals. This is achieved by laser heating the samples and compressing them using diamond-anvil cells. The sample can be then probed using techniques such as transmission electron microscopy TEM, Mössbauer spectroscopy, Brillouin scattering, X-ray diffraction, ultrasonic spectroscopy, or neutron scattering. However, these sophisticated experimental techniques are difficult to perform, tend to be expensive, and data recollection from them at such extreme conditions is usually scarce. This brings us to the third method, where high-performance computing and quantum mechanics come into play. First principle calculations, also known as *ab-initio* calculations, are quantum mechanical computations that allow us to obtain highly reliable data of mantle minerals at extreme pressure and temperature conditions. This work is dedicated to the use of quantum-mechanical, elastic, and thermodynamic calculations, to improve our current knowledge of the interior of our planet, more specifically, the Earth's lower mantle.

As previously discussed, an exceptional way to probe the Earth's interior is via seismic models and tomographic maps. Perhaps, the most commonly used one dimensional seismic model is the Preliminary Reference Earth Model (PREM) [29]. Proposed by Dziewonski in 1982, this model is still considered robust and is used to estimate different physical properties of the Earth, e.g., elastic moduli and density, as a function of its radius. A comprehensive diagram displaying the seismic velocities, compressional (V_P) and shear (V_S), and density (ρ) are shown in Figure 1.2. The discontinuities on the aforementioned properties mark the presence of phase transitions and consequently,

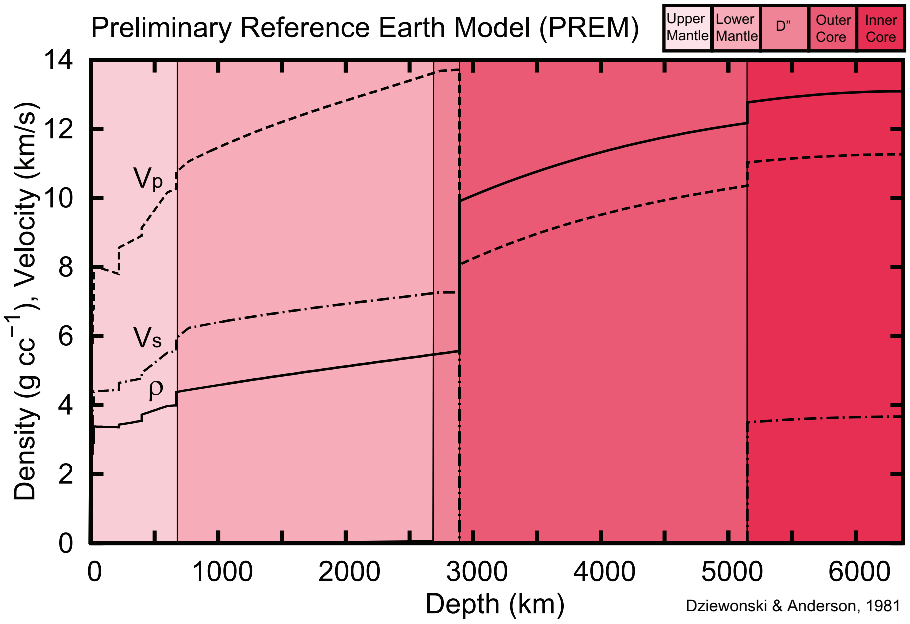

Figure 1.2: Preliminary Reference Earth Model (PREM) [29]. Earth's layers are shown in different intensities of red.

the location of the different layers. For instance, V$_S$ is zero throughout the outer core, which indicates that this region is liquid. PREM is used as a reference model for our calculations and is revisited in some of the subsequent chapters of this manuscript.

The pressure at depth can be computed from the density profiles of one-dimensional seismic models, e.g., PREM. However, is it possible to calculate the temperature? Many different approximations have been performed from various sources. Figure 1.3 shows some of the different lower mantle temperature profiles, also known as geotherms. These were calculated from various sources such as seismic input, experimental mineral physics, and geodynamic simulations. While there is some agreement about the temperature at the base of the lower mantle, at deep lower mantle conditions, differences among these profiles can be up to 650 K. In this work, we use Brown and Shankland geotherm [15] as a reference temperature for our calculations. Details about these geotherms and calculations of temperature profiles are discussed in chapter 3.

Temperature gradients are of great importance as they drive the convection processes responsible for tectonics. Cold pieces of land, or slabs, sink into the mantle, while the hot material that sits atop the CMB becomes buoyant and rises to the surface in the form

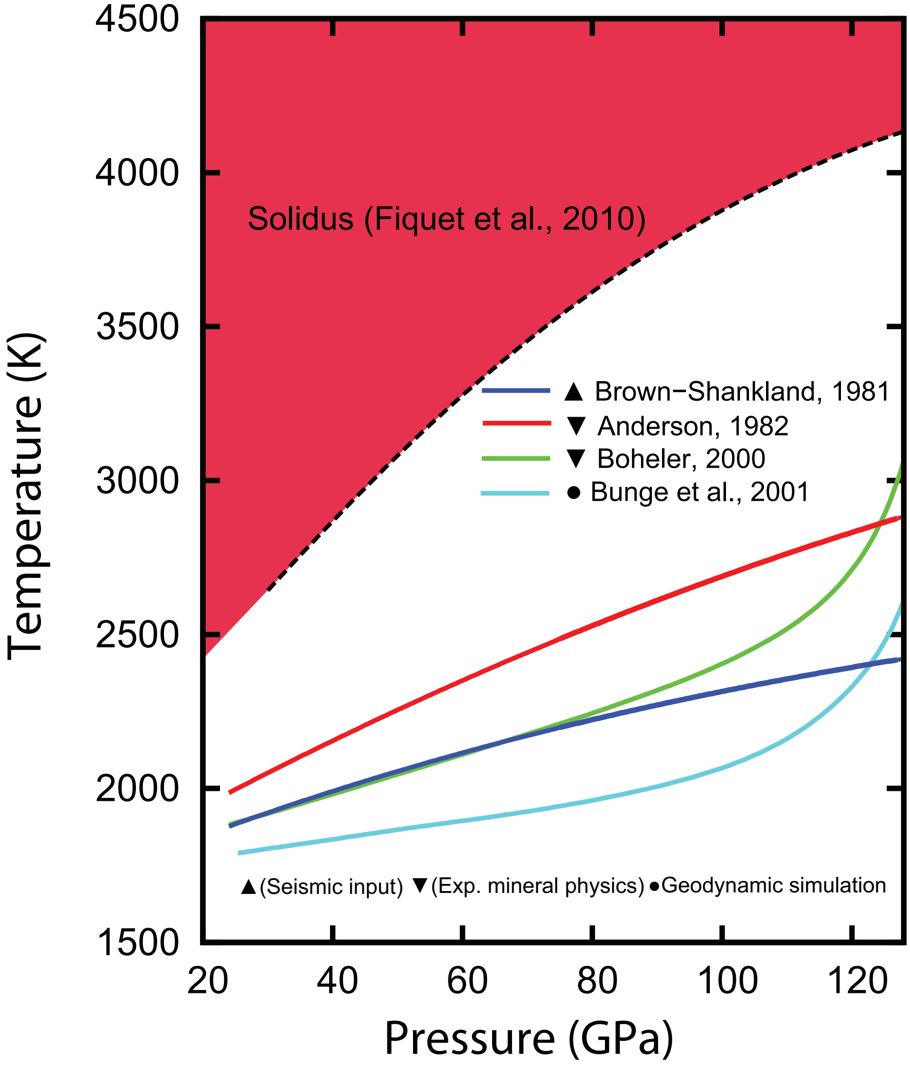

Figure 1.3: Lower mantle geotherms. The solidus is indicated by the dotted line.

of plumes (See Figure 1.4). This convection process occurs at a geological timescale ($\sim 10^6$ years). Therefore, it's considered to be isentropic and adiabatic. Deviations from adiabaticity have relevant implications on geodynamic processes, e.g., how the mantle can conduct or dissipate heat. Hence, it's important to test for adiabaticity. An observable that allow us to achieve the latter is the Bullen's parameter. In this work, we use the Bullen's parameter to evaluate such adiabaticity deviations for different possible mantle compositions (See chapter 4). From Figure 1.4 it can also be observed that the seismic velocities are affected by lateral temperature heterogeneities. However, there is no consensus on how the temperature varies laterally since these variations are not yet well-constrained in the deep mantle [41]. Deviations from adiabaticity are also tested, via Bullen's parameter, for a laterally thermal heterogeneous mantle (See chapter 4).

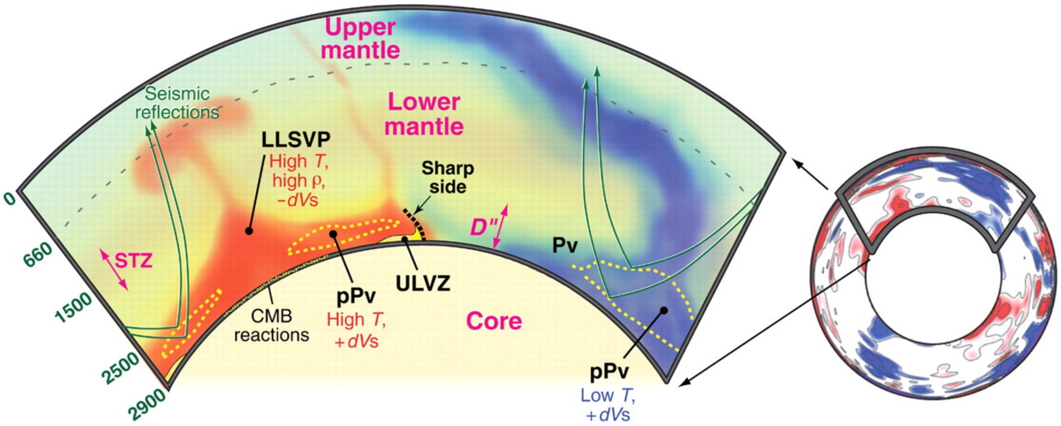

Figure 1.4: Equatorial cross section (right) viewed from the south, along with an enlarged panel (left) depicting shear velocity variations in Earth's mantle. High and low V_S variations are in blue and red, respectively. Cold subducting slabs (blue) and a hot plumes (red) carry the mantle convection. STZ is the spin transition zone. LLSVP depicts the large low-shear-velocity provinces and the ultralow-velocity zone (ULVZ, yellow) material sits atop the CMB. Taken from [31]

The effects of another important phenomenon on the lower mantle temperature, known as spin-crossover, are studied in detail in chapter 3. The ferric iron (Fe^{3+}) in bdg's B site, and ferrous iron (Fe^{2+}) in fp, change their spin state with increasing pressure. This is known as spin-crossover. Hence, spin-crossover is a pressure induced reordering of the electronic structure of the iron. If Fe is in an octahedral arrangement (Figure 1.5) surrounded by O atoms, the Fe $3d$-orbitals that overlap with oxygen orbitals have higher energy (e_g) than those that point away from the O-orbtials (t_{2g}). This energy difference is known as crystal field energy E_{CF}. On the other hand, the energy difference between parallel and anti-parallel spins is called exchange energy E_X. At lower pressures, E_X is typically larger than E_{CF}. However, as pressure increases, E_{CF} overcomes E_X. As a consequence of the latter, the magnetic moment varies from a high spin (HS) to a low spin (LS) state. An schematic showing the net magnetic moment of Fe in HS and LS is shown in Figure 1.5a). This was first seen experimentally by Badro et al. [9], using X-ray emission spectroscopy. Figure 1.5c) shows how the kβ' line, the first satellite, characteristic of the 3-d magnetic moment of Fe, disappears with increasing pressure. This pressure induced spin state change will lead to a volume collapse of the crystal structure and also affect the thermoelastic properties of the minerals. A discussion about this anomalous behavior is presented in chapter 2. Spin crossover has not yet been resolved in global seismic models. Thus, in an attempt to reconcile mineral physics with seismic observations, we used the Bullen's parameter as a seismic observable to detect spin-crossovers in the lower mantle (See chapter 4).

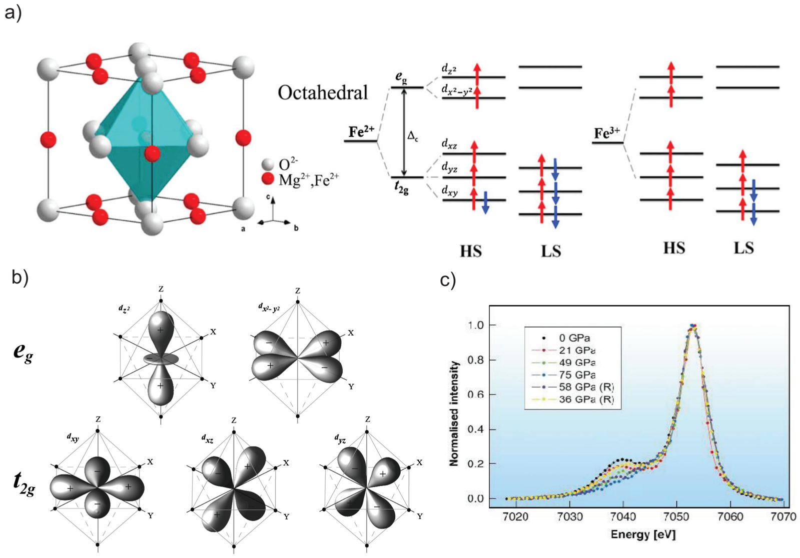

Figure 1.5: a) Octahedral site in ferropericlase. b) $3d$-orbitals configurations in a octahedral site. a) and b) are taken from [59]. c) X-ray emission spectra of ferropericlase $Mg_{0.83}Fe_{0.17}O$ at different pressures. Taken from [9]

This thesis is divided as follows: Chapter 2 shows the theoretical aspects involved in the calculations presented in this work. Chapter 3 discusses the details involved in the calculations of temperature profiles, from the thermodynamic properties of lower mantle minerals, and the effects of spin-crossovers on the lower mantle temperature gradient. Chapter 4 discusses the importance of computing deviations from adiabaticity and how these can be used to resolve spin-crossovers in the lower mantle. Chapter 5 depicts the effects, due to the post-perovskite phase transition, on the seismic observables of the deep mantle, and the influence of bearing atoms such as Fe and Al across this important phase transformation. Chapter 6 presents a summary of the results shown in this manuscript.

Chapter 2

Theoretical Outline

This chapter briefly discusses some of the theoretical aspects involved in the calculation of thermodynamic properties of the lower mantle minerals, aggregates, temperature profiles, and phase boundaries. We start by reviewing some of the quantum mechanical details involved in *ab initio* calculations, followed by the elasticity principles and constitutive relations needed to compute the thermoelastic properties. Finally, we review some of the structural parameters of lower mantle minerals and the thermodynamics behind phase transitions of binary systems.

2.1 Many-body systems and density functional theory

2.1.1 The Born-Oppenheimer approximation

Our starting point to solve the many body system is to write down its Hamiltonian explicitly

$$\begin{split}\hat{H} = -\frac{\hbar^2}{2m_e}\sum_i \nabla_i^2 + \frac{1}{2}\sum_{i\neq j} e^2/(|\mathbf{r}_i - \mathbf{r}_j|) + \sum_{i,\alpha} Z_\alpha e^2/(|\mathbf{r}_i - \mathbf{R}_\alpha|) - ...\\ ... - \sum_\alpha \frac{\hbar^2}{2M_\alpha}\nabla_\alpha^2 + \frac{1}{2}\sum_{\alpha\neq\beta} Z_\alpha Z_\beta e^2/(|\mathbf{R}_\alpha - \mathbf{R}_\beta|)\end{split} \tag{2.1}$$

In equation (2.1), the electron and ion (Nuclei) positions are indicated by $\mathbf{r}$,$\mathbf{R}$, with charges e and Z, and are represented by the indices i,j, and α, β, respectively. The first term of equation (2.1) corresponds to the electron kinetic energy ($\hat{T}_r$), the second is the electron-electron interaction ($\hat{V}_{ee}$), the third term is the ion Coulomb potential acting on the electrons ($\hat{V}_{ext}$), the fourth depicts the ion kinetic energy ($\hat{T}_R$), and the fifth term the ion-ion interaction ($\hat{V}_{II}$). Since the proton to electron mass ratio is $M/m_e \sim 1836$, $\hat{T}_R$ can be regarded to be negligible compared to $\hat{T}_r$. This known as the Born-Oppenheimer (B-O) approximation [62]. This approximation has proven to work sufficiently well when used to perform structural relaxations to find optimized (stable) crystal structures under pressure. After applying the B-O approximation, the Hamiltonian can then be rewritten as

$$\hat{H} = \hat{T}_r + \hat{V}_{ee} + \hat{V}_{ext} + \hat{V}_{II} \tag{2.2}$$

and its solution could be found by solving the eigenvalue problem given by the Schrödinger equation

$$\hat{H}\Psi(\mathbf{r}, \mathbf{R}) = E\Psi(\mathbf{r}, \mathbf{R}) \tag{2.3}$$

where $\Psi(\mathbf{r}, \mathbf{R})$ represents the coupled ionic-electronic many-body wave function. Due the complexity of (2.3), its exact solution is not achievable in real life. Hence, to simplify this problem, $\Psi(\mathbf{r}, \mathbf{R})$ is decoupled thanks to the B-O approximation

$$\Psi(\mathbf{r}, \mathbf{R}) = \phi(\mathbf{R})\psi_{\mathbf{R}}(\mathbf{r}) \tag{2.4}$$

with $\phi(\mathbf{R})$ and $\psi_{\mathbf{R}}(\mathbf{r})$ as the ionic and electronic wave functions, respectively. This decoupling allows us to write the Schrödinger equation for the electrons under a external potential due ions as

$$\begin{aligned}\left(-\frac{\hbar^2}{2m_e}\sum_i \nabla_i^2 + \frac{1}{2}\sum_{i\neq j}\frac{e^2}{(|\mathbf{r}_i - \mathbf{r}_j|)} + \sum_{i,\alpha} Z_\alpha \frac{e^2}{(|\mathbf{r}_i - \mathbf{R}_\alpha|)} + \frac{1}{2}\sum_{\alpha\neq\beta}\frac{Z_\alpha Z_\beta e^2}{(|\mathbf{R}_\alpha - \mathbf{R}_\beta|)}\right)\psi_{\mathbf{R}}(\mathbf{r}) = \\ = E(\mathbf{R})\psi_{\mathbf{R}}(\mathbf{r})\end{aligned} \tag{2.5}$$

and for the ions

$$\left(-\sum_{\alpha}\frac{\hbar^2}{2M_\alpha}\nabla_\alpha^2 + E(\mathbf{R})\right)\phi(\mathbf{R}) = \mathscr{E}\phi(\mathbf{R}) \tag{2.6}$$

where $E(\mathbf{R})$ is known as the Born-Oppenheimer potential energy surface, i.e., $E(\mathbf{R})$ is the ground state energy of the electrons for a given fixed ionic configuration. While the B-O approximation simplifies the problem significantly, equation (2.5) is still extremely complicated to solve exactly due to the electron-electron interactions. It is here where density functional theory comes into play, in order to find a solution for a real system.

2.1.2 Density functional theory

The fundamental advantage of the density functional theory (DFT) is that it allows determining any property of a many body system as a functional of its ground state electron density $n_o(\mathbf{r})$. In other words, a scalar function $n_o(\mathbf{r})$ can, in principle, resolve all the properties within the many body wave functions of the ground and excited states. The latter is thanks to Hohenberg and Kohn, who demonstrated that for any system with interacting particles inside an external potential $V_{ext}(\mathbf{r})$, such potential is uniquely determined (except by a constant) by $n_o(\mathbf{r})$. This implies that the hamiltonian of (2.5) is fully determined and therefore all the many body wavefunctions (ground and excited) are determined. This one to one correspondence between V_{ext} and $n_o(\mathbf{r})$ also implies that there exists a universal functional form of the energy $E[n(\mathbf{r})]$, whose global minimum will then provide the exact ground state energy. Moreover, the density that minimizes such functional is the exact ground state density $n_o(\mathbf{r})$ [62]. This functional form of the energy can be defined as

$$E[n(\mathbf{r})] = F[n(\mathbf{r})] + \int V_{ext}(\mathbf{r})n(\mathbf{r})d\mathbf{r} + E_{II} \tag{2.7}$$

with $F[n(\mathbf{r})]$ carrying the kinetic energy plus the electron-electron Coulomb interaction, and E_{II} the interaction between ions. If the total amount of electrons is preserved, i.e.

$$\int n(\mathbf{r})d\mathbf{r} = N \tag{2.8}$$

then the minimization of $E[n(\mathbf{r})]$ gives the ground state energy and the ground electron density of the many body system. Moreover, if the density $n(\mathbf{r'})$ is not the ground state, then $E[n(\mathbf{r'})] > E[n(\mathbf{r})]$. This is known as the variational principle. DFT became a practical theory only after Kohn and Sham [57] provided an appropriate definition of $F[n(\mathbf{r})]$. What Kohn and Sham did was to propose an auxiliary non-interacting form of the many body interacting system, as in equation (2.5), that can be described with the single particle Schrödinger equation in an effective local potential. The idea is to let the ground state electron density of the auxiliary non-interacting system to be the same as that of the original interacting one, and because the auxiliary system also obeys Hohenberg and Kohn theorem, i.e. the global minimum of $E[n(\mathbf{r})]$ provides the exact ground state energy, the functional $F[n(\mathbf{r})]$ of this new non-interacting system is the kinetic energy of non-interacting electrons. The question now is: what is the form of $F[n(\mathbf{r})]$?. First, one needs to recall that the electron density is given by

$$n(\mathbf{r}) = \sum_{i=1}^{N} |\psi_i(\mathbf{r})|^2 \tag{2.9}$$

and thus, the functional $F[n(\mathbf{r})]$ can be defined as

$$F[n(\mathbf{r})] = T_o[n(\mathbf{r})] + E_{hart}[n(\mathbf{r})] + E_{xc}[n(\mathbf{r})] \tag{2.10}$$

The first term of (2.10) is the kinetic energy of non-interacting electrons $T_o[n(\mathbf{r})]$, which is given by the expression

$$T_o[n(\mathbf{r})] = \frac{\hbar^2}{2m_e} \sum_{i=1}^{N} \langle \psi_i | \nabla_i^2 | \psi_i \rangle \tag{2.11}$$

The second term in (2.10), known as the Hartree functional $E_{hart}[n(\mathbf{r})]$, contains the classical Coulombic interaction of $n(\mathbf{r})$ with itself, i.e.

$$E_{hart}[n(\mathbf{r})] = \frac{e^2}{2} \int \frac{n(\mathbf{r})n(\mathbf{r'})}{|\mathbf{r} - \mathbf{r'}|} d\mathbf{r} d\mathbf{r'} \tag{2.12}$$

and the third term of (2.10) is the so-called exchange-correlation energy $E_{xc}[n(\mathbf{r})]$, which accounts for all the effects due the interacting electrons. This exchange-correlation energy is defined as the difference of the energies (kinetic and potential) between the real interacting many body system and the fictitious non-interacting system

$$\begin{aligned} E_{xc}[n(\mathbf{r})] &= F[n(\mathbf{r})] - (T_o[n(\mathbf{r})] + E_{hart}[n(\mathbf{r})]) \\ &= (\hat{T}_r - T_o[n(\mathbf{r})]) + (\hat{V}_{ee} - E_{hart}[n(\mathbf{r})]) \end{aligned} \tag{2.13}$$

With the latter, we now can construct the total (Kohn-Sham) energy of the interacting many body system as

$$E_{KS}[n(\mathbf{r})] = T_o[n(\mathbf{r})] + E_{hart}[n(\mathbf{r})] + E_{xc}[n(\mathbf{r})] + \int V_{ext}(\mathbf{r})n(\mathbf{r})d(\mathbf{r}) + E_{II} \tag{2.14}$$

and the auxiliary non-interacting system as

$$E^0_{KS}[n(\mathbf{r})] = T_o[n(\mathbf{r})] + \int V_{KS}(\mathbf{r})n(\mathbf{r})d(\mathbf{r}) + E_{II} \tag{2.15}$$

Both, (2.14) and (2.15) are to be minimized under the constraint in (2.8) and with the same electron density $n(\mathbf{r})$. The Kohn-Sham potential energy V_{KS} is defined as

$$V_{KS}(\mathbf{r}) = V_{ext}(\mathbf{r}) + \left(e^2 \int \frac{n(\mathbf{r'})}{|\mathbf{r} - \mathbf{r'}|} d\mathbf{r'}\right) + \frac{\delta E_{xc}[n(\mathbf{r})]}{\delta n(\mathbf{r})} \tag{2.16}$$

If the exchange energy $E_{xc}[n(\mathbf{r})]$ is known, then the many body system could be seen as a non-interacting electron gas under a Kohn-Sham potential $V_{KS}(\mathbf{r})$. Moreover, $E^0_{KS}[n(\mathbf{r})]$ can be defined in terms of a single particle wave function $\psi_i(\mathbf{r})$, once (2.9) and (2.11) are implemented into (2.15). This implies that minimization of $E^0_{KS}[n(\mathbf{r})]$ with (2.8), along with the orthonormality constraint

$$\int \psi^*_i(\mathbf{r})\psi_j(\mathbf{r})d\mathbf{r} = \delta_{i,j} \tag{2.17}$$

is the same as minimizing the energy with respect to the wave function

$$\frac{\delta E^0_{KS}}{\delta \psi^*_i} = 0 \tag{2.18}$$

Thus, one obtains a Kohn-Sham hamiltonian $\hat{H}_{KS}$, which can be solved with single particle Schrödinger-like equations

$$\hat{H}_{KS}\psi_i(\mathbf{r}) = \left(-\frac{\hbar^2}{2m_e}\nabla^2_i + V_{KS}\right)\psi_i(\mathbf{r}) = E_i\psi_i(\mathbf{r}) \tag{2.19}$$

where E_i are the eigenvalues of the Kohn-Sham hamiltonian and $\psi_i(\mathbf{r})$ the wave functions with no physical meaning. The reason of this is that $\psi_i(\mathbf{r})$ are eigenfunctions of the fictitious non-interacting system, where only the ground state electron density is equivalent to that of the real system. Equations (2.9),(2.16), and (2.19) are known as the Kohn-Sham equations.

We can see then that the advantage of the Kohn-Sham formulation is that one can solve the interacting many body system with single particle Schrödinger-like equations. Nevertheless, such equations are highly non linear because the potential V_{KS} depends on its own solutions. This is why V_{KS} needs to be solved self-consistently, i.e., use the resulting density to find the new potential. Furthermore, the calculation of the ground state properties is achievable as far as $E_{xc}[n(\mathbf{r})]$ is known. However, the exchange-correlation energy is unknown and one needs to rely on approximate definitions of that functional, i.e.

$$E_{xc}[n(\mathbf{r})] = \int n(\mathbf{r})\epsilon_{xc}[n(\mathbf{r}), \mathbf{r}]d\mathbf{r} \tag{2.20}$$

where $\epsilon_{xc}[n(\mathbf{r}), \mathbf{r}]$ is known as the exchange-correlation energy per electron, at point $\mathbf{r}$, which depends on the density $n(\mathbf{r})$ in the vicinity of $\mathbf{r}$. One can approximate exchange-correlation energy to depend only on the density, i.e., $\epsilon_{xc}[n(\mathbf{r})]$, since solids can often be considered, according to Kohn and Sham, to be close to the limit of a homogeneous electrons gas. This is known as the local density approximation (LDA). Therefore

$$E_{xc}^{LDA} = \int n(\mathbf{r})\epsilon_{xc}[n(\mathbf{r})]d\mathbf{r} \tag{2.21}$$

The LDA formulation has proven to be a good approximation to determine structural and vibrational properties of metals, semiconductors, and insulators. Cons about LDA is that it tends to fail when used to compute, for instance, band gaps for insulators and semiconductors, and the ground states of some transition metals. To overcome this, the gradient of the density $|\nabla n(\mathbf{r})|$ is included in the LDA approximation. This is known as the generalized gradient approximation (GGA)

$$E_{xc}^{GGA} = \int n(\mathbf{r})\epsilon_{xc}[n(\mathbf{r}), |\nabla n(\mathbf{r})|]d\mathbf{r} \tag{2.22}$$

This approximation does improve estimations of energy band gaps in insulators and semiconductors, but works poorly to compute structural and elastic properties.

2.1.3 Fundamentals of Phonons and Lattice Vibrations

Phonons, or lattice vibrations, are described by Bose-Einstein statistics. They fall into the category of Bosons since they carry spin zero [55]. For a 3D crystal, there are 3N independent vibrational modes. For instance, a crystal with two atoms per unit cell will have two different dispersion relations (Acoustic and optical), which at the same time are divided into longitudinal (LA, LO) phonons and transverse (TA,TO) phonons. For every N atoms in the primitive cell, there will be 3N acoustic branches and 3N - 3 optical. The corresponding dispersion relations in this case are

$$\omega^2 \approx 2C\left(\frac{1}{M_1}+\frac{1}{M_2}\right) \qquad (optic) \tag{2.23}$$

$$\omega^2 \approx \frac{\frac{1}{2}C}{M_1+M_2} \qquad (acoustic) \tag{2.24}$$

with M_1 and M_2 as the masses of the atoms and C as the elastic constant. The above are, of course, very simple approximations. In practice, to compute the vibrational modes from a real system using *ab initio* calculations, the energies found from solving (2.19) are used to obtain the forces exerted on the ions, i.e.

$$\mathbf{F}_\alpha = -\frac{\partial E(\mathbf{R})}{\partial \mathbf{R}_\alpha} \tag{2.25}$$

with $E(\mathbf{R})$ as the ground state Kohn-Sham energy for the ionic configuration. One can also define the forces as

$$\mathbf{F}_\alpha = -\sum_i \left\langle \psi_i \left| \frac{\partial \hat{H}(\mathbf{R})}{\partial \mathbf{R}_\alpha} \right| \psi_i \right\rangle \tag{2.26}$$

This is known as the Hellmann-Feynman theorem: The change of energy with respect to a given parameter is equal to the expectation value of the change of the hamiltonian with respect to the same parameter. The phonons ω can be found from the eigenvalues of the Hessian

$$det\left|\frac{1}{\sqrt{M_\alpha M_\beta}}\frac{\partial^2 E(\mathbf{R})}{\partial \mathbf{R}_\alpha \partial \mathbf{R}_\beta} - \omega^2\right| = 0 \tag{2.27}$$

where

$$\frac{\partial^2 E(\mathbf{R})}{\partial \mathbf{R}_\alpha \partial \mathbf{R}_\beta} = -\frac{\partial \mathbf{F}_\alpha}{\partial \mathbf{R}_\beta} \tag{2.28}$$

2.1.4 Quasi-Harmonic Approximation

With ω, it is now possible to access all the thermodynamic potentials. To do so, we used the Quasi-Harmonic Approximation (QHA) to calculate the free energy of the system. QHA is a corollary of the harmonic model approximation (HA), which assumes that the interatomic forces of a crystal are harmonic only. However, HA fails to describe thermal expansion of the crystalline system, since it considers the equilibrium distance between atoms to be temperature independent. In contrast, the QHA phonon frequencies are volume-dependent ($\omega(V)$). QHA treats the system as a group of independent harmonic oscillators, i.e. a phonon "gas", each of those vibrating with a particular frequency $\omega(V)$, which determines the quantum mechanical energy levels of the system. These energy levels are then used to find the partition function Z and the Helmholtz free energy F [107].

The partition function of one oscillator is the summation of Boltzmann factors as

$$Z_i = \sum_n e^{-E_n/k_B T} \tag{2.29}$$

where k_B is the Boltzmann constant. Since the energy is $E_n = (n + 1/2)\hbar\omega$ for a quantum harmonic oscillator with n energy levels, we have

$$\begin{aligned} Z_i &= \sum_n e^{-(n+1/2)\hbar\omega_i/k_B T} \\ Z_i &= e^{(1/2)\hbar\omega_i/k_B T} \sum_n e^{-\hbar\omega_i n/k_B T} \end{aligned} \tag{2.30}$$

Using the approximation

$$\sum e^x = \frac{1}{1-x} \tag{2.31}$$

then

$$Z_i = \frac{e^{-(1/2)\hbar\omega_i/k_BT}}{1-e^{-\hbar\omega_i/k_BT}} \tag{2.32}$$

and from the statistical definition for the Helmholtz free energy

$$F_i = -k_BTlnZ_i = -k_BTln\left(\frac{e^{-\hbar\omega_i/2k_BT}}{1-e^{-\hbar\omega_i/k_BT}}\right) = \frac{\hbar\omega_i}{2} + k_BTln\left(1-e^{-\hbar\omega_i/k_BT}\right) \tag{2.33}$$

Therefore, for a lattice with normal mode frequencies ω_i, the total free energy is

$$F = \sum_i F_i = U + \sum_i \frac{\hbar\omega_i}{2} + \sum_i k_BTln\left(1-e^{-\hbar\omega_i/k_BT}\right) \tag{2.34}$$

where U is the internal energy. From the Helmholtz free energy F, all other thermodynamic properties can be found using the thermodynamic potentials, i.e.

$$U = TS - PV \qquad H = U + PV \qquad G = F + PV \tag{2.35}$$

QHA is known for being an effective approximation to calculate the thermodynamics properties of solids. However, it has some limitations. For instance, QHA at low temperatures requires a more complete quantum treatment, whereas for the high temperature limit is not appropriate due to the phonon-phonon interactions. The conventional upper temperature limit is the Debye temperature. Nonetheless, the validity of the QHA can also be determined from the second derivative of the thermal expansion coefficient $\alpha = \frac{1}{V}\left(\frac{\partial V}{\partial T}\right)_P$. Results that $\frac{\partial^2\alpha(P,T)}{\partial T^2} \geq 0$ are not within the range of the validity of the QHA [107].

2.2 Linear Elasticity and Equations of State

2.2.1 The stress-strain relation, elastic moduli, and seismic velocities

The strain tensor in the linear elastic regime, is defined as

$$\epsilon_{ij} = \frac{1}{2}(\frac{u_i}{x_j} + \frac{u_j}{x_i}) \tag{2.36}$$

where u_i are the components of the displacement vector. The trace of the strain tensor is known as the dilatation of a deformed body

$$\epsilon_{ii} = \frac{\Delta V}{V} \tag{2.37}$$

The stress-strain relation is given by

$$\sigma_{ij} = c_{ijkl}\epsilon_{kl} \tag{2.38}$$

where c_{ijkl} is known as the stiffness tensor and it contains the elastic constants of the system [78]. The hydrostatic pressure P can be found from the trace of the stress tensor

$$P = \frac{1}{3}\sigma_{kk} \tag{2.39}$$

Another important constitutive relation that invokes the stiffness tensor is the strain energy density function

$$w(\epsilon) = \frac{1}{2}c_{ijkl}\epsilon_{ij}\epsilon_{kl} \tag{2.40}$$

We now notice that c_{ijkl} has 81 components, which can be reduced to 21 independent constants after using the symmetries of the stress tensor $c_{ijkl} = c_{jikl}$, strain tensor $c_{ijkl} = c_{ijlk}$, and that the strain energy density is invariant under $c_{ijkl} = c_{klij}$ [78]. Moreover, Voigt notation allows us to express the elastic constants in a reduced form, i.e. $ij \to \alpha, 11 \to 1, 22 \to 2, 33 \to 3, (23, 32) \to 4, (13, 31) \to 5, (12, 21) \to 6$. Hence, the stiffness or elasticity tensor will be given by

$$C_{\alpha\beta} = \begin{pmatrix} c_{11} & c_{12} & \cdots & c_{16} \\ c_{21} & c_{22} & \cdots & c_{26} \\ \vdots & \vdots & \ddots & \vdots \\ c_{61} & c_{62} & \cdots & c_{66} \end{pmatrix} \tag{2.41}$$

Computing the elastic constants of a crystal is relevant to study its elastic behavior. To calculate them, we need to consider the symmetry of the crystal. Minerals have different symmetries such as cubic (MgO) and orthorhombic ($MgSiO_3$), among others. Due to the symmetry of these structures, the amount of elastic constants that need to be found varies: Let a, b, c be the lattice parameters of a given crystal. In a cubic structure, the lattice parameters $a = b = c$, and in this case we only need to find c_{11}, c_{12} and c_{44} since $c_{11} = c_{22} = c_{33}$ (modulus of axial compression), $c_{44} = c_{55} = c_{66}$ (shear modulus) and $c_{12} = c_{13} = c_{23}$ (modulus of dilation or compression), while the others $c_{ij} = 0$ (This is due to rotation and reflection arguments not discussed here).

$$C_{\alpha\beta} = \begin{pmatrix} c_{11} & c_{12} & c_{12} & 0 & 0 & 0 \\ c_{12} & c_{11} & c_{12} & 0 & 0 & 0 \\ c_{12} & c_{12} & c_{11} & 0 & 0 & 0 \\ 0 & 0 & 0 & c_{44} & 0 & 0 \\ 0 & 0 & 0 & 0 & c_{44} & 0 \\ 0 & 0 & 0 & 0 & 0 & c_{44} \end{pmatrix} \tag{2.42}$$

The lattice parameters for an orthorhombic structure are $a \neq b \neq c$. For this symmetry we are required to find nine different elastic constants: c_{11}, c_{22}, c_{33}, c_{44}, c_{55}, c_{66}, c_{12}, c_{13} and c_{23}. Hence

$$C_{\alpha\beta} = \begin{pmatrix} c_{11} & c_{12} & c_{13} & 0 & 0 & 0 \\ c_{12} & c_{22} & c_{23} & 0 & 0 & 0 \\ c_{13} & c_{23} & c_{33} & 0 & 0 & 0 \\ 0 & 0 & 0 & c_{44} & 0 & 0 \\ 0 & 0 & 0 & 0 & c_{55} & 0 \\ 0 & 0 & 0 & 0 & 0 & c_{66} \end{pmatrix} \tag{2.43}$$

By only applying the infinitesimal strains ϵ_{11} and ϵ_{12}, is sufficient to compute the 3 elastic constants of the cubic crystal. However, the same cannot be done for the orthorhombic system, and all the strains (normal and shear) must be applied to get the 9 elastic constants.

The stress-strain relation for an isotropic system can be written as

$$\sigma_{ij} = \lambda \delta_{ij} \epsilon_{kk} + 2\mu \epsilon_{ij} \tag{2.44}$$

where $\lambda + 2\mu = c_{11}$ and $\mu = c_{44}$ are known as the Lamé coefficients [77].

To measure the compressibility of a given system, we need to compute another important quantity known as the bulk modulus K, which is given by the ratio of the change in pressure with respect to the fractional volume compression, or density ρ, as

$$K = -V\frac{dP}{dV} = -\frac{dP}{dlnV} = \frac{dP}{dln\rho} \tag{2.45}$$

which in the linear elastic regime leads to

$$\frac{\Delta V}{V} = -\frac{P}{K} \tag{2.46}$$

and therefore, we can define K in terms of the Lamé coefficients as

$$K = \frac{3\lambda + 2\mu}{3} \tag{2.47}$$

The negative ratio between normal strains is known as the Poisson ratio ν

$$\nu = -\frac{\epsilon_{22}}{\epsilon_{11}} = -\frac{\epsilon_{33}}{\epsilon_{11}} \tag{2.48}$$

For instance, if only uniaxial stress σ_{11} is considered and $\sigma_{22} = \sigma_{33} = 0$, we get

$$\nu = \frac{\lambda}{2(\lambda + \mu)} = \frac{3(K/\mu) - 2}{2[3(K/\mu) + 1]} \tag{2.49}$$

According to Poirier [77], for most of the Earth's crust $\lambda = \mu$, and therefore $\nu = 0.25$. The velocities of a wave propagating through an isotropic solid, i.e., the longitudinal V_p and transverse V_s velocities, are also a function of the Lamé coefficients

$$V_p = \left(\frac{\lambda + 2\mu}{\rho}\right)^{1/2} \qquad V_s = \left(\frac{\mu}{\rho}\right)^{1/2} \tag{2.50}$$

with ρ as the specific mass. Also, one can notice that

$$\frac{V_p}{V_S} = \left(\frac{\lambda + 2\mu}{\mu}\right)^{1/2} \tag{2.51}$$

The velocities are commonly written as

$$V_p = \sqrt{\frac{K + \frac{4}{3}G}{\rho}}, V_\phi = \sqrt{\frac{K}{\rho}}, V_s = \sqrt{\frac{G}{\rho}} \tag{2.52}$$

where V_ϕ is known as the bulk velocity. From equation (2.51) it is possible to write ν in terms of the velocities

$$\nu = \frac{\left(\frac{V_p}{V_S}\right)^2 - 2}{2\left[\left(\frac{V_p}{V_S}\right)^2 - 1\right]} \tag{2.53}$$

since $\nu = 0.25$, we get $V_p = V_s\sqrt{3}$, which according to Poirier [77] is a common relation for the Earth's crust.

Other important elasticity relations are: The seismic parameter ϕ

$$\phi = \frac{dP}{d\rho} = \frac{K}{\rho} = V_p^2 - \frac{4}{3}V_s^2 \tag{2.54}$$

The isothermal bulk modulus and adiabatic bulk modulus

$$K_T = \left(-V\frac{\partial P}{\partial V}\right)_T \qquad K_S = \left(-V\frac{\partial P}{\partial V}\right)_S \tag{2.55}$$

$$K_S - K_T = \alpha K_T T\left(\frac{\alpha K_s V}{C_p}\right) \tag{2.56}$$

where the fraction inside the brackets is known as the Grüneisen parameter

$$\gamma = \frac{\alpha K_S V}{C_p} = \frac{\alpha K_T V}{C_V} \tag{2.57}$$

and therefore

$$\frac{K_s}{K_T} = 1 + \gamma\alpha T = \frac{C_p}{C_V} \tag{2.58}$$

The isobaric and isochoric specific heat are represented by C_p and C_V, respectively.

2.2.2 The Voigt-Reuss-Hill Average

The elastic moduli (Bulk K and shear G) can be determined from the elastic constants (C$_{i,j}$) and compliances (S$_{i,j}$) of the crystal. A common approach is to estimate the upper and lower bounds of the elastic moduli, namely, assuming uniform stress and uniform strain states, and then obtain the arithmetic mean of these quantities. This is known as the Voigt-Reuss-Hill (VRH) averaging scheme [105]. The Voigt average assumes that strain is uniform throughout the system (upper bound). For a polycrystalline system is defined as

$$K_V = \frac{1}{9}[(C_{11} + C_{22} + C_{33}) + 2(C_{12} + C_{23} + C_{13})] \tag{2.59}$$

$$G_V = \frac{1}{15}[(C_{11} + C_{22} + C_{33}) - (C_{12} + C_{23} + C_{13}) + 3(C_{44} + C_{55} + C_{66})] \tag{2.60}$$

The Reuss bound assumes uniform stress and can be computed as

$$\frac{1}{K_R} = [(S_{11} + S_{22} + S_{33}) + 2(S_{12} + S_{23} + S_{13})] \tag{2.61}$$

$$\frac{15}{G_R} = [4(S_{11} + S_{22} + S_{33}) - 4(S_{12} + S_{23} + S_{13}) + 3(S_{44} + S_{55} + S_{66})] \tag{2.62}$$

with the compliances S_{ij} coming from inverting the elastic constant matrix C_{ij} from equation (2.43). Furthermore, for a given aggregate or 'rock', the Voigt and Reuss bounds depend on the molar fraction ζ of each mineral and can be calculated as

$$\begin{aligned} K_V &= \sum_i \zeta_i K_i \\ G_V &= \sum_i \zeta_i K_i \\ \frac{1}{K_R} &= \sum_i \zeta_i \frac{1}{K_i} \\ \frac{1}{G_R} &= \sum_i \zeta_i \frac{1}{G_i} \end{aligned} \tag{2.63}$$

where the subscript i indicates the number of different species in the sample. The arithmetic average of the Voigt and Reuss bounds is known as the Hill average. Thus, the VRH average of the elastic moduli are

$$K_{VRH} = \frac{K_V + K_R}{2} \qquad G_{VRH} = \frac{G_V + G_R}{2} \tag{2.64}$$

The VRH average method is known to provide a very good estimate of the Earth's lower mantle aggregate moduli.

2.2.3 Birch-Murnahgan Equation of State

In thermodynamics, the state of matter is determined by equations relating properties such as volume V, density ρ, pressure P, and temperature T. These equations are known as equations of state (EoS). According to Poirier [77], the simplest isothermal EoS is given by the bulk modulus relation of equation (2.45). Although, this relation is not valid at high temperatures as it doesn't take into account the strong dependence of K with respect to temperature. Integrating the differential equation and letting $K = K_0$, we get

$$V = V_0 e^{-P/K_0} \tag{2.65}$$

which describes the volume dependence with respect to pressure. However, a better approximation for the effective local bulk modulus was proposed by Murnahgan

$$K = \frac{1}{3}(3\lambda + 2\mu + P_0) \tag{2.66}$$

Assuming that λ and μ are linear functions of P_0, we get

$$K = \frac{1}{3}(3\lambda_0 + 2\mu_0) + kP_0 \tag{2.67}$$

Using equation (2.45), we get

$$dln\rho = \frac{dP}{K_0 + kP_0} \tag{2.68}$$

Integrating and letting $P_0 = P$ and $K_0' = (dK/dP)_{P=0}$,

$$\rho = \rho_0 \left(1 + \frac{K_0'}{K_0}\right)^{1/K_0'} \tag{2.69}$$

which is known as the Murnahgan's linear EoS [77]. Other EoS that can be obtained in the linear elastic regime, is the Birch-Murnahgan EoS. For infinitesimal strains it can be shown that

$$\frac{\rho_0}{\rho} = \frac{V}{V_0} = (1+2f)^{-3/2} \approx 1 - 3f \tag{2.70}$$

with $f = -\epsilon$ (compression). Therefore $f \to 0$ for infinitesimal strains, and thus, the differential volume of equation (2.70) would be $dV \approx -3V_0 df$. The latter implies

$$9K_{0T}V_0 = \lim_{P\to 0}\left(\frac{1}{f}\frac{\partial F}{\partial f}\right)_T \tag{2.71}$$

where K_{0T} is the isothermal bulk modulus and F the Helmholtz free energy.

We now expand F in powers of f. Considering the unstrained energy to be zero and recalling that the elastic energy is quadratic for infinitesimal strains, we get

$$F = a(T)f^2 + b(T)f^3 + c(T)f^4 + ... \tag{2.72}$$

For the second order BM equation we have $F \approx af^2$, with $a = (9/2)K_{0T}V_0$. Since the pressure is

$$P = -\left(\frac{\partial F}{\partial V}\right)_T = -\left(\frac{\partial F}{\partial f}\right)_T \frac{df}{dV} \tag{2.73}$$

Also, differentiating (2.70), we get

$$\frac{dF}{dV} = -\frac{1}{3V_0}(1+2f)^{5/2} \tag{2.74}$$

thus

$$P = 3K_{0T}f(1+2f)^{5/2} \tag{2.75}$$

From (2.70), the compression in terms of the density ratio is

$$f = \frac{1}{2}\left[\left(\frac{\rho}{\rho_0}\right)^{2/3} - 1\right] \tag{2.76}$$

and replacing into (2.75), we get the second order Birch-Murnaghan (BM) EoS

$$P_{BM2} = \frac{3K_{0T}}{2}\left[\left(\frac{\rho}{\rho_0}\right)^{7/3} - \left(\frac{\rho}{\rho_0}\right)^{5/3}\right] \tag{2.77}$$

For the third order BM equation one simply includes the third order term of the Helmholtz free energy as

$$F = a(T)f^2 + b(T)f^3 \tag{2.78}$$

and following a similar derivation process as for the second BM EoS we obtain

$$\begin{aligned} P_{BM3} = \frac{3K_{0T}}{2}&\left[\left(\frac{\rho}{\rho_0}\right)^{7/3} - \left(\frac{\rho}{\rho_0}\right)^{5/3}\right] \\ &\left[1 + \frac{3}{4}(K'_0 - 4)\left[\left(\frac{\rho}{\rho_0}\right)^{2/3} - 1\right]\right] \end{aligned} \tag{2.79}$$

which is the third BM EoS.

2.2.4 The Mie-Debye-Grüneisen Model

An alternative approach to calculate the thermoelastic properties of minerals at high P-T conditions, is to use the Mie-Debye-Grüneisen (MDG) model. This formulation is based on the idea of the thermal pressure, which is the thermal contribution to P_{BM3} (2.79) and can be written as

$$P = P_{BM3} + \Delta P_{th} \tag{2.80}$$

with ΔP_{th} as the change in thermal pressure. This thermal pressure depends on the Grüneisen parameter and the change in thermal energy E_{th} as

$$\Delta P_{th} = \frac{\gamma(V)}{V}(E_{th}(V,T) - E_{th}(V,T_0)) \tag{2.81}$$

where the subscript zero designates the thermodynamic variable at ambient or initial condition. The Grüneisen coefficient, in this case, depends on the volume via

$$\gamma(V) = \gamma_0 \left(\frac{V}{V_0}\right)^q \tag{2.82}$$

with q as a material constant. Furthermore, the thermal energy E_{th} is given by the well known Debye energy expression [55]

$$E_{th} = \frac{9k_B T^4}{\theta^3} \int_0^{x_D} \frac{x^3}{e^x - 1} dx \tag{2.83}$$

with θ as the Debye temperature

$$\theta = \theta_0 exp \left(\frac{\gamma_0 - \gamma}{q}\right) \tag{2.84}$$

and $x_D = \theta/T$. Hence, from (2.80), it can be shown that the bulk and shear moduli are [90, 91]

$$K = (1+2f)^{\frac{5}{2}} \left[K_0 + (3K_0K_0' - 5K_0)f + \frac{27}{2}(K_0K_0' - 4K_0)f^2\right] + (\gamma+1-q)\gamma\Delta E_{th} - \gamma^2\rho\Delta(C_vT) \tag{2.85}$$

$$G = (1+2f)^{\frac{5}{2}} \left[G_0 + (3K_0G_0' - 5G_0)f + (6K_0G_0' - 24K_0 - 14K_0 + \frac{9}{2}K_0K_0')f^2\right] - n_s\rho\Delta E_{th} \tag{2.86}$$

where

$$n_s = -\gamma + \frac{1}{2}\frac{\theta_0}{\theta}(2f+1)^2(2\gamma_0 + n_{so}) \tag{2.87}$$

and n_{so} as a material constant. Also, recalling that the isochoric Debye specific heat is given by

$$C_V = \frac{9k_B T^3}{\theta^3} \int_0^{x_D} \frac{x^4 e^x}{(e^x - 1)^2} dx \tag{2.88}$$

and

$$\Delta(C_VT) = TC_V(V,T) - T_0C_V(V,T_0) \tag{2.89}$$

Other thermodynamic properties such as the thermal expansion coefficient α and isobaric specific heat C_P can be computed as

$$\alpha = \frac{\gamma C_V}{KV} \tag{2.90}$$

and

$$C_P = C_V(1 + \alpha\gamma T) \tag{2.91}$$

The MDG parameters for lower mantle minerals can be found in Table 2.1

Table 2.1: MDG parameters listed in Stixrude et al. [91] (*) and Kawai-Tsuchiya [52] (**) for lower mantle minerals

Mineral	V_0(cc mol^{-1})	K_{T0} (GPa)	K'_{T0}	θ_0 (K)	γ_0	q_0	G_0 (GPa)	G'_0	n_{s0}
*$MgSiO_3$	24.45	251(3)	4.1 (1)	905(5)	1.57 (5)	1.1(3)	173(2)	1.7(0)	2.6(3)
*MgO	11.24	161(3)	3.8(2)	767(9)	1.36(5)	1.7(2)	131(1)	2.1(1)	2.8(2)
*CaSiO3	27.45	236(4)	3.9(2)	796(44)	1.89(7)	0.9(16)	157(12)	2.2(5)	1.3(10)
**CaSiO3	27.832	206.6	4.41	1100	1.567	0.84			

2.2.5 Spin crossover softening

Understanding the fundamentals of how spin crossover of iron in fp induces the anomalous behavior in the elastic moduli is important. Here we show the source of such anomalies following the formulation proposed by Wu et al. [112]. The mixed spin (MS) state can be defined as an ideal solid solution of the system in high spin HS and low spin LS states. Therefore, the Gibbs free energy can be defined as

$$\mathscr{G} = n\mathscr{G}_{LS} + (1-n)\mathscr{G}_{HS} + \mathscr{G}_{mix} \tag{2.92}$$

with $n = n(P,T)$ is the low spin fraction, i.e., the fraction of irons in LS state. Also, $\mathscr{G}_{LS}$ and $\mathscr{G}_{HS}$ are the Gibbs free energies of LS and HS states, and $\mathscr{G}_{mix}$ is the free energy of mixing. On the other hand, the elastic compliances S^{ij} are given by

$$S^{ij} = -\frac{1}{V}\left(\frac{\partial^2\mathscr{G}}{\partial\sigma_i\partial\sigma_j}\right)_{P,T} \tag{2.93}$$

Implementing equation (2.92) into (2.93) one gets

$$S^{ij}V = nS^{ij}_{LS}V_{LS} + (1-n)S^{ij}_{HS}V_{HS} - \left(\frac{\partial \mathscr{G}_{LS}}{\partial \sigma_j} - \frac{\partial \mathscr{G}_{HS}}{\partial \sigma_j}\right)\frac{\partial n}{\partial \sigma_i} \tag{2.94}$$

The first two terms of (2.94) give the weighted average of the compliances of HS and LS states, and the last term only appears when the system is in mixed spin (MS) state, i.e. $\frac{\partial n}{\partial \sigma_i}$ causes the anomalies in the bulk modulus K (See for example Figure 2.5). The reason is that the elastic constants C^{11} and C^{12} are the only ones that are affected by the change of n due to an applied stress, while C^{44} is unaffected. Thus, the shear modulus G do not display anomalous behavior. The compliances for fp (cubic crystal) are

$$\begin{aligned} S^{11} &= nS^{11}_{LS}V_{LS} + (1-n)S^{11}_{HS}V_{HS} - \frac{1}{9}(V_{LS} - V_{HS})\frac{\partial n}{\partial P}, \\ S^{12} &= nS^{12}_{LS}V_{LS} + (1-n)S^{12}_{HS}V_{HS} - \frac{1}{9}(V_{LS} - V_{HS})\frac{\partial n}{\partial P}, \\ S^{44} &= nS^{44}_{LS}V_{LS} + (1-n)S^{44}_{HS}V_{HS} \end{aligned} \tag{2.95}$$

S^{11} and S^{12} display the anomalies since $\frac{\partial n}{\partial \sigma_1} \neq 0$. However, for S^{44}, $\frac{\partial n}{\partial \sigma_4} = 0$ since $n(\sigma_4)$ is an even function of σ_4.

2.2.6 The isentropic temperature gradient

Infinitesimal changes in entropy $S(T, P)$ are given by

$$dS = \left(\frac{\partial S}{\partial T}\right)_P dT + \left(\frac{\partial S}{\partial P}\right)_T dP \tag{2.96}$$

Moreover, in an isentropic system, state changes at constant $dS = 0$ give

$$\left(\frac{\partial S}{\partial T}\right)_P dT = -\left(\frac{\partial S}{\partial P}\right)_T dP \tag{2.97}$$

therefore

$$\left(\frac{\partial S}{\partial T}\right)_P \left(\frac{\partial T}{\partial P}\right)_S = -\left(\frac{\partial S}{\partial P}\right)_T \tag{2.98}$$

and thus

$$\left(\frac{\partial S}{\partial T}\right)_P \left(\frac{\partial T}{\partial P}\right)_S \left(\frac{\partial P}{\partial S}\right)_T = -1 \tag{2.99}$$

From Maxwell's relations we know

$$\left(\frac{\partial S}{\partial P}\right)_T = \left(\frac{\partial V}{\partial T}\right)_P \tag{2.100}$$

Also, the thermal expansion coefficient coefficient is formally defined as

$$\alpha = \frac{1}{V}\left(\frac{\partial V}{\partial T}\right)_P \tag{2.101}$$

and the isobaric specific heat

$$C_P = T\left(\frac{S}{T}\right)_P \tag{2.102}$$

Replacing (2.100,2.101,2.102) into (2.99), we obtain the adiabatic gradient

$$\left(\frac{\partial T}{\partial P}\right)_S = \frac{\alpha V T}{C_P} \tag{2.103}$$

Equation (2.103) shows how temperature changes adiabatically with respect to pressure. This gradient is typically assumed to calculate the temperature gradient of the Earth's interior.

2.2.7 The Adams-Williamson equation and the Bullen's parameter

The Bullen's parameter and its relevance is discussed in chapter 4. Here we derive some details about this parameter. As previously shown, the bulk modulus of a mineral under adiabatic self compression is given by

$$K_S = \rho\left(\frac{\partial P}{\partial \rho}\right)_S \tag{2.104}$$

Hence

$$\frac{K_S}{\rho} = \left(\frac{\partial P}{\partial \rho}\right)_S = \phi \tag{2.105}$$

where ϕ is the seismic parameter $\phi = V_P^2 - \left(\frac{4}{3}\right) V_S^2$. Furthermore, assuming a homogeneous media under hydrostatic changes in pressures with respect to depth

$$\frac{dP}{dr} = -\rho g \tag{2.106}$$

where g and r are the acceleration due to gravity and depth, respectively. Thus

$$\frac{dP}{d\rho}\frac{d\rho}{dr} = -\rho g \tag{2.107}$$

and using equation (2.105)

$$1 = -\phi\rho^{-1}g^{-1}\frac{d\rho}{dr} \tag{2.108}$$

Equation (2.108) is known as the Adams-Williamson equation.

If the system is not adiabatic, i.e., equation (2.108) differs from the unity, we have,

$$\eta = -\phi\rho^{-1}g^{-1}\frac{d\rho}{dr} = \phi\frac{d\rho}{dP} \tag{2.109}$$

where η is the Bullen's parameter [18].

2.3 Lower mantle minerals

As discussed in chapter 1, the main lower mantle phases are bdg (Al- Fe- bearing $MgSiO_3$ pervoskite), $CaSiO_3$ perovskite (CaPv), and fp (Mg,Fe)O [47, 49, 71]. We now look into some detail, some of the structural and thermoelastic properties of these minerals.

2.3.1 Bridgmanite

This is the most abundant mineral phase making up approximately 70% of the lower mantle's volume. Hence, accurate knowledge about this phase is essential to understand and model the lower mantle. Bdg is a perovskite (Pv) orthorhombic *Pbnm* structure of the form ABO_3, metastable below 23 GPa, where the Si atoms are located inside the octahedra (B sites) and Mg atoms at the interstitial 'A' sites (Figure 2.1). The ferrous Fe^{2+} iron always goes into the B site, while the ferric Fe^{3+} and Al can go to either site. For $Mg_{1-x}Fe_x^{2+}SiO_3$ no spin crossover occurs at lower mantle conditions

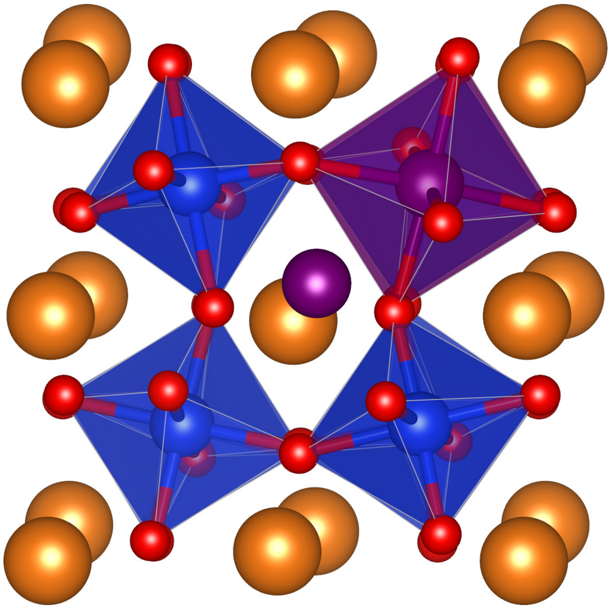

Figure 2.1: $MgSiO_3$ Pv Pbnm structure. Red/Blue/Orange/Purple spheres represent Oxygen/Silicon/Magnesium/Iron-Aluminum. Figure produced using [69].

[11, 43, 44, 58, 83, 86], while for $(Mg_{1-y}Fe^{3+}_y)(Si_{1-y}Fe^{3+}_y)O_3$, the ferric iron in the B site can undergo spin crossover at lower mantle conditions [82].

For all the calculations shown in this manuscript, we used the thermoelastic properties from Shukla et al. [82, 86]. Figure 2.2 shows how well the *ab-initio* calculations compare with experimental data, even at high pressures and temperatures [71]. Thus, we believe that the results that we present here are quite robust.

2.3.2 Post-Perovskite phase

The Post-Perovskite (PPv) phase is presumably the most abundant mineral in the D" region of the mantle, i.e., ~ 300 km above the core mantle boundary. The conditions at which the bdg Pv to PPv transition occurs are expected to be above ~ 125 GPa and 2500 K. The consequences on the thermoelastic properties and seismic observables due this phase transition are studied in detail in chapter 5. The PPv phase is a highly anisotropic layered structure, with a space group *Cmcm*, where the Mg and Fe atoms can be located in the interlayer region (See Figure 2.3). Since its discovery in 2004 [70, 99], significant progress has been made to understand the thermoelastic properties of this

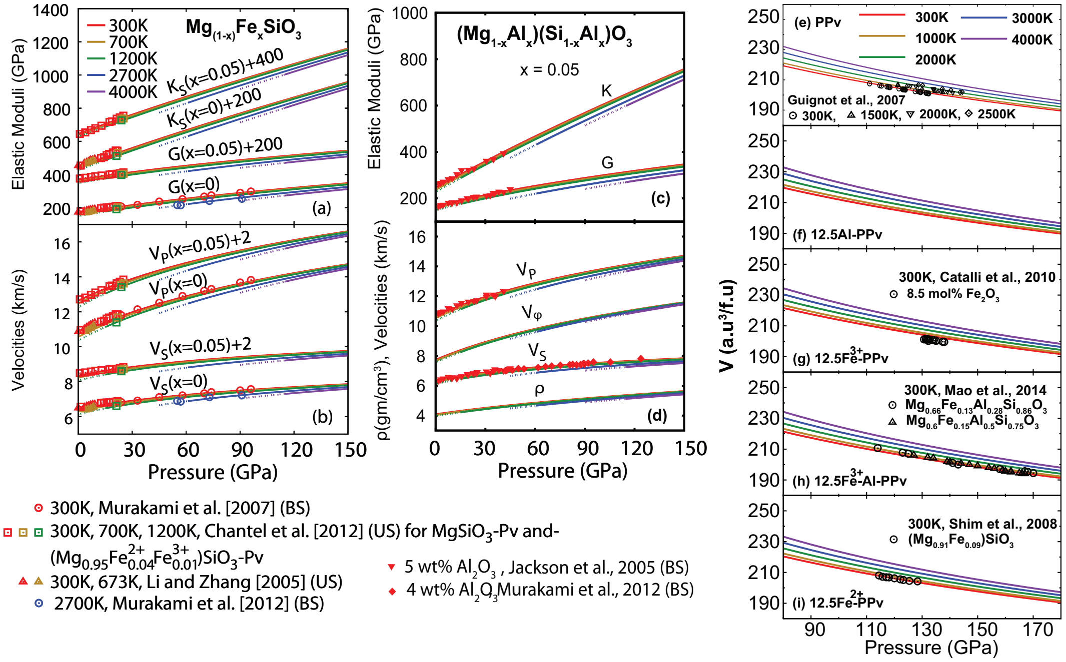

Figure 2.2: Elastic moduli, velocities, and densities for: (a,b) $MgSiO_3$ + $Mg_{1-x}Fe_x^{2+}SiO_3$ and (c,d) $Mg_{1-x}Al_xSi_{1-x}Al_xO_3$ compared with experimental data. Solid/dashed lines represent *ab initio* results within/outside the validity of QHA. US: Ultrasonic technique and BS: Brillouin Scattering. Taken from [82, 86]. Figures (e) to (i) depict the compressive behavior of pristine, Al, Fe^{3+}, Fe^{3+}-Al, and Fe^{2+}-bearing post-perovskite, respectively (To be submitted [84]). Symbols in all figures correspond to experimental values.

mineral. However, there is still a limited amount of experimental data because of the extreme conditions at which this phase exists. The PPv thermoelastic properties used in our calculations are to be submitted in Shukla et al. [84] and the compression curves with different bearing minerals can be seen in Figure 2.2.

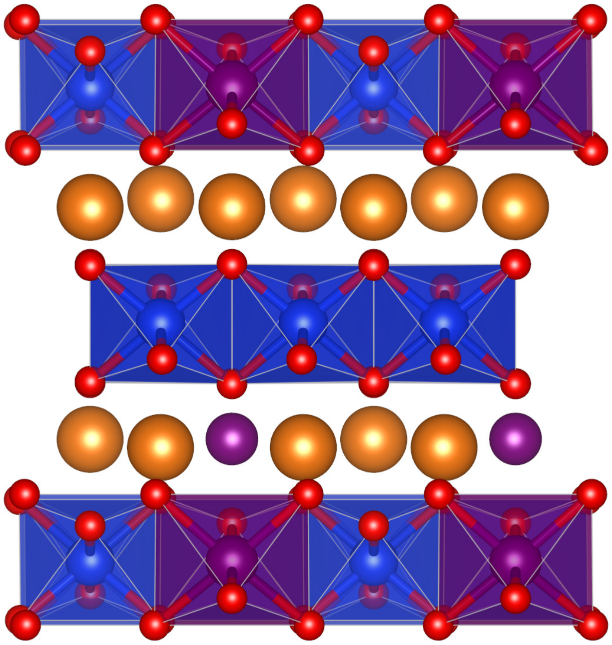

Figure 2.3: Post-perovskite lamellar structure with space group Cmcm. Red/Blue/Orange/Purple spheres represent Oxygen/Silicon/Magnesium/Iron-Aluminum. Figure produced using [69].

2.3.3 Ferropericlase

The MgO crystal has a cubic (rock-salt) structure with space group symmetry Fm3m, where the magnesium atoms are located at corners and faces of the cube (See Figure 2.4). MgO is the primary end-member of ferropericlase (fp) $Mg_{1-x}Fe_xO$ and the second most abundant mineral in the lower mantle, which makes it a relevant phase to study. Furthermore, the iron in fp undergoes through a spin crossover from high spin (HS) to low spin (LS), which affects the thermoelastic properties of this mineral (Figure 2.5) and thus, the elastic properties of the lower mantle as a whole. In this work we use fp data from [112].

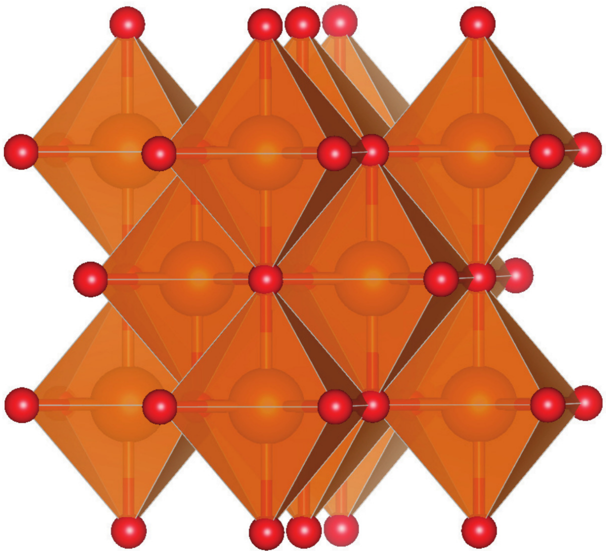

Figure 2.4: Ferropericlase structure. Red/Orange spheres represent oxygen/(magnesium or iron) atoms. Figure produced using [69].

In chapters 3 and 4 we study in detail what are the consequences of this spin crossover in the Earth's lower mantle temperature and adiabaticity.

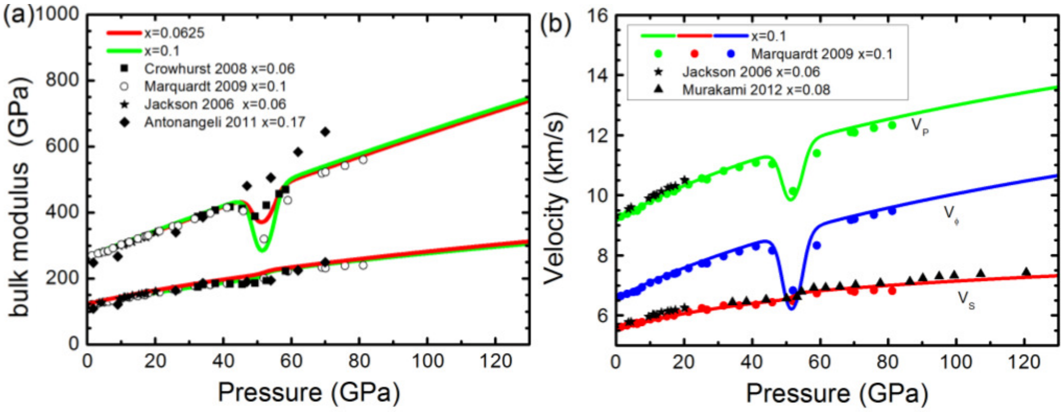

Figure 2.5: Elastic moduli and velocities for $Mg_{1-x}Fe_xO$ compared with experimental data. Taken from [112].

2.3.4 $CaSiO_3$ perovskite

The $CaSiO_3$ perovskite (CaPv) phase makes up about 5% of the volume of the lower mantle, which makes it an important phase to study. However, this phase is difficult to study experimentally since it's unquenchable to ambient pressure [107]. Moreover, it is known to be a strongly anharmonic crystal, which makes QHA inadequate to determine its thermoelastic properties. Therefore, the thermoelastic properties of this mineral are typically computed via molecular dynamics simulations. At lower mantle conditions, CaPv is a cubic structure with symmetry $Pm\overline{3}m$, with the Ca atom located in the middle of the unit cell surrounded by Si octahedra (See Figure 2.6). We reproduced the CaPv properties using the MDG method, from the calculations by Kawai and Tsuchiya [52,53].

The compressive behavior of CaPv by Kawai and Tsuchiya [52,53] is not in agreement with measurements done by Stixrude [91] and recent experimental results by Sun et al. [92]. However, Kawai and Tsuchiya [52, 53] do report, consistently, the temperature dependence for the shear modulus of this mineral.

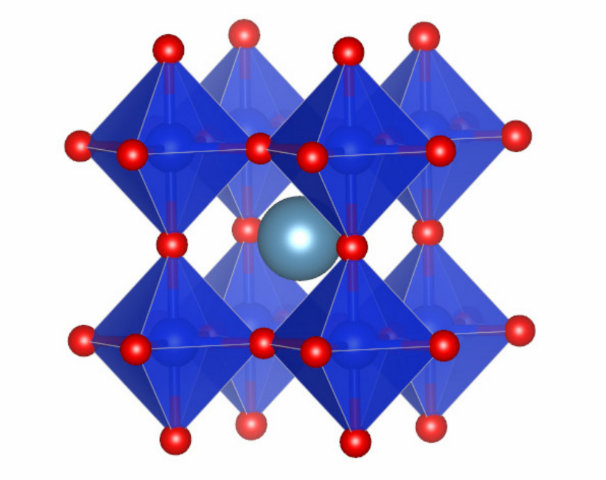

Figure 2.6: CaSiO$_3$ structure. Light/Dark blue and red sheres represent calcium/silicon and oxygen atoms. Figure produced using [69]

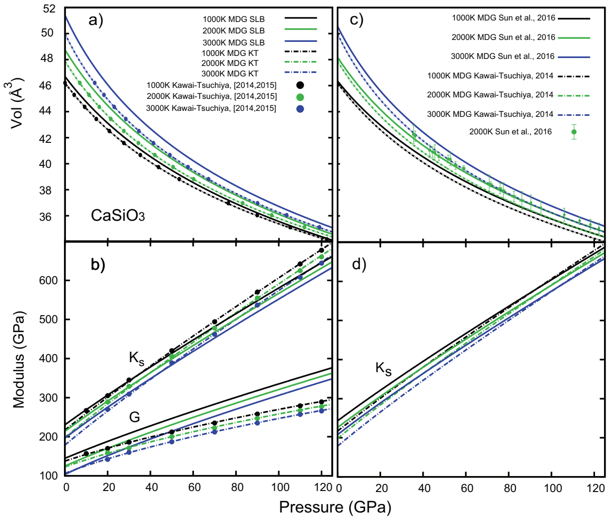

Figure 2.7: (a) CaSiO$_3$ compression curves and (b) moduli for different temperatures. Solid lines represent data obtained using the Mie-Debye-Grüneisen (MDG) model with EoS parameters from [91] (SLB, see also Table 2.1). Dashed lines are results calculated using parameters from Kawai and Tsuchiya [52, 53] (KT). Dots correspond to direct results reported by [52, 53]. (c) CaSiO$_3$ compression curves and (d) bulk modulus for different temperatures. Solid lines represent data obtained using the Mie-Debye-Grüneisen (MDG) model with EoS parameters from [92]. Dashed lines are results calculated using parameters from [52]. Dots and error bars correspond to experimental results reported by [92].

2.4 Phase boundary of binary systems: The Pv to PPv transition

The stable state of a system is that at which the minimum possible value of Gibbs free energy $\mathscr{G}$ is achieved. Thus, to compute the phase boundary of bridgmanite going from its Pv to the PPv configuration, we used the Gibbs free energy of these systems along with the standard state approach. The standard state of a component, or mineral in our case, is merely a reference state to which the component in any other state is compared. Therefore, any state can be chosen to be the standard state and its choice is usually made on a convenience basis [32].

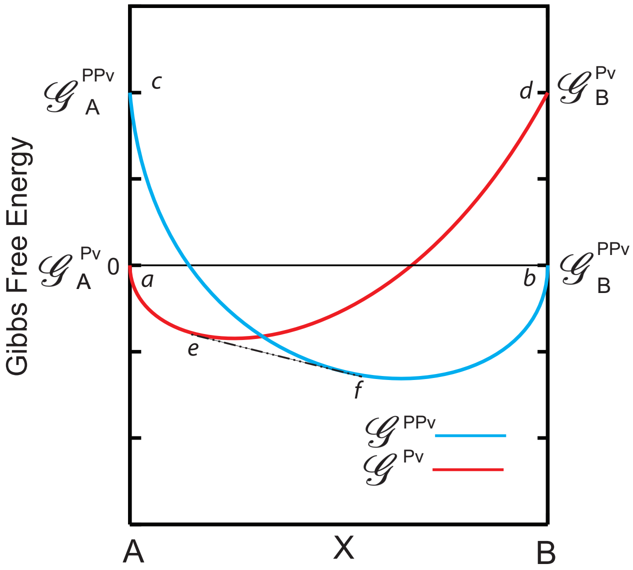

Figure 2.8: Schematic of Gibbs free energy curves for a binary system A-B for Pv and PPv solid solutions.

Figure 2.8 shows a schematic of the two Gibbs free energy curves of the Pv and PPv states in a A-B binary system, at a given fixed pressure and temperature. More explicitly, let the end members be A: $MgSiO_3$, B: $Fe^{2+}SiO_3$, $Fe_2^{3+}O_3$, Al_2O_3, or $Fe^{3+}AlO_3$, and x denotes the bearing element concentration. The Gibbs free energies of the Pv and PPv are

$$\mathscr{G}^{Pv}(T,P,x) = x(\mathscr{G}_B^{Pv} - \mathscr{G}_B^{PPv}) + k_B T(xln[x] + (1-x)ln[1-x]) \tag{2.110}$$

$$\mathscr{G}^{PPv}(T,P,x) = (1-x)(\mathscr{G}_A^{PPv} - \mathscr{G}_A^{Pv}) + k_B T(xln[x] + (1-x)ln[1-x]) \tag{2.111}$$

In Figure 2.8, the stable states of pure A and B are located at $\mathscr{G} = 0$. Also, notice that at point *a* x_A=1 and at point *b* x_B=1. Point *c* represents the Gibbs free energy of solid A in a PPv state, relative to A in a Pv configuration. Similarly, point *d* represents the Gibbs free energy of solid B in Pv relative to B in PPv. At composition *e*, the tangent to the curve for the Pv solution is also tangent to the PPv composition at point *f*. This means that both compositions are in equilibrium and that the Pv and PPv phases coexist in the *e* - *f* region. The loci of *e* and *f*, as temperature varies, will trace out the Pv and PPv boundaries. Moreover, the molar concentrations of the bearing elements indicated by the symbol (*); e.g. Fe^{2+}, Fe^{3+}, Al^{3+}, or (Fe^{3+}, Al^{3+}), in each phase are given by

$$x_*^{PPv} = \frac{1 - e^{\frac{\mathscr{G}_A^{PPv} - \mathscr{G}_A^{Pv}}{k_B T}}}{e^{\frac{\mathscr{G}_B^{PPv} - \mathscr{G}_B^{Pv}}{k_B T}} - e^{\frac{\mathscr{G}_A^{PPv} - \mathscr{G}_A^{Pv}}{k_B T}}} \tag{2.112}$$

$$x_*^{Pv} = x_*^{PPv}(e^{\frac{\mathscr{G}_B^{PPv} - \mathscr{G}_B^{Pv}}{k_B T}}) \tag{2.113}$$

which allows us to compute PPv fraction n_{PPv} using the lever rule

$$n_{PPv} = \frac{x - x_*^{Pv}}{x_*^{PPv} - x_*^{Pv}} \tag{2.114}$$

In chapter 5 we make use of the above formulation to determine the Pv-PPv phase boundaries.

Chapter 3

Influence of the iron spin crossover in ferropericlase on the lower mantle geotherm

The iron spin crossover in ferropericlase introduces anomalies in its thermodynamics and thermoelastic properties. In this chapter we investigate how these anomalies can affect the lower mantle geotherm using thermodynamics properties from *ab initio* calculations. The anomalous effect is examined in mantle aggregates consisting of mixtures of bridgmanite, ferropericlase, and $CaSiO_3$ perovskite, with different Mg/Si ratios varying from harzburgitic to perovskitic (Mg/Si$\sim$1.5 to 0.8). We find that the anomalies introduced by the spin crossover increase the isentropic gradient and thus the geotherm proportionally to the amount of ferropericlase. The geotherms can be as much as ~ 200 K hotter than the conventional adiabatic geotherm at deep lower mantle conditions. Aggregate elastic moduli and seismic velocities are also sensitive to the spin crossover and the geotherm, which impacts analyses of lower mantle velocities and composition.

3.1 Introduction

One of the grand challenges in geophysics is to resolve the thermal structure of the Earth's interior. This is clearly not an isolated problem but a fundamental one to clarify the dynamics, evolution, and chemical stratification of the planet [67, 71, 109]. Besides, a one dimensional (1D) temperature profile is an abstract construct – a spherically averaged reference temperature model consistent with spherically averaged velocity and composition profiles. To date, numerous one dimensional temperature profiles, or geotherms, have been suggested and calculated by various means and using different assumptions. For example, these include: seismological observations [15], mineral physics input [4, 7, 12] computations [25, 50, 104] or measurements [91], geodynamic simulations [13, 66, 103], or a combination of them [27, 38]. Differences between them arise not only from the technique or input data, but from the constraints to which they are subjected to, i.e., the melting temperature of iron, phase transitions, seismic discontinuities, convection processes, and lower mantle composition. In addition, lateral velocity heterogeneities point to lateral temperature and/or composition variations, a very difficult problem that still awaits, e.g., advances in geodynamic simulations. Thus, construction of one dimensional temperature profiles must be seen as an insufficient but a necessary exercise to advance this topic.

An essential aspect in constructing a geotherm, is to define a suitable potential temperature, i.e., the boundary condition for integration of the adiabatic gradient. Most geotherms are anchored to depths associated with seismic discontinuities (e.g. the ~ 660 km discontinuity), where phase transitions occur [77]. For the top of the lower mantle, we assumed a temperature of 1873 K at 23 GPa as in Brown and Shankland [15] (B&S) (See also [1]). The latter is an adiabatic temperature profile constructed from the Debye entropy formulation [14] and the acoustic velocities from the preliminary reference Earth model (PREM) [29]. This geotherm is considered by many to be the standard adiabatic geotherm for the lower mantle. It's important to point out that the conditions at which ringwoodite dissociates into bridgmanite (bdg) and ferropericlase (fp) are still somewhat controversial [23, 48, 51, 115]. Thus, the appropriate potential temperature for the lower mantle geotherm is debatable. Several other geotherms, e.g., [4], [12] and [7] were obtained by extrapolating the temperature from the inner and outer core geotherm using the phase diagram of iron. Additionally, geotherms constructed from *ab initio* calculations include different approaches; for instance, [25] and [50] calculated the temperatures needed to fit the bulk modulus of pyrolite to PREM. Others such as [98], constructed the geotherm from the set of temperatures of different isobars at which the vibrational entropy of bridgmanite was constant.

In this chapter, we integrated the isentropic gradient formula using thermodynamics properties of minerals obtained by *ab initio* calculations, starting from the standard boundary condition at 660 km depth, i.e., the experimentally determined post-spinel transition conditions [1], also used by Brown and Shankland [15]. The relevant lower mantle phases are bdg (Al- Fe- bearing $MgSiO_3$ pervoskite), $CaSiO_3$ perovskite (CaPv), and fp (Mg,Fe)O [47, 49, 71]. These minerals form a variety of aggregates commonly characterized by their Mg/Si molar ratio. However, the relative abundances of these aggregates in the lower mantle is still debatable [47, 49, 71, 104, 110, 113]. Here we derived isentropes for likely mantle aggregates such as harzburgite (Mg/Si $\sim$ 1.56) [10], chondrite (Mg/Si $\sim$ 1.07) [33], pyrolite (Mg/Si $\sim$ 1.24) [67], peridotite (Mg/Si $\sim$ 1.30) [39], and perovskite only (Mg/Si $\sim$ 0.82) [109] to asses the effect of Mg/Si ratio on the isentrope. The presence of FeO in these aggregates needs special consideration. It is well known that ferrous iron (Fe^{+2}) in fp exhibits a spin crossover at lower mantle conditions [9, 89, 100], which introduces anomalies in its thermodynamics [106, 111] and thermoelastic properties [6, 24, 61, 71, 112, 113]. Here we investigated in details how these anomalies affect the isentropes of these aggregates in the lower mantle. While some geodynamic simulations have shown the potential effect of spin crossover on the lower mantle adiabat [13, 103], clarification of this effect in the isentropes of several aggregates is a first order question in advancing the problem of mantle temperatures. Finally, we examined the effect such spin crossover induced thermal anomalies have on aggregate velocities.

3.2 Method and Calculation Details

The thermoelastic properties of bdg $Mg_{1-x}Fe^{2+}_xSiO_3$, $(Mg_{1-x}Al_x)(Si_{1-x}Al_x)O_3$, $(Mg_{1-x}Fe^{3+}_x)(Si_{1-x}Al_x)O_3$, $(Mg_{1-x}Fe^{3+}_x)(Si_{1-x}Fe^{3+}_x)O_3$ ($x = 0$ and 0.125), and fp $Mg_{1-y}Fe_yO$ ($y = 0$ and 0.1875) were obtained from [82, 86] and [112] respectively. Results for other

x and y concentrations shown in this work were linearly interpolated and only high spin (HS) Fe^{2+} -bdg was used since no spin crossover in Fe^{2+} occurs in bdg at lower mantle conditions [11, 30, 42–45, 58, 83, 86]. For CaPv, thermoelastic properties from [52, 53] were reproduced within the Mie-Debye-Grüneisen [90] formalism (see chapter 2). We considered mixtures of SiO_2 - MgO - CaO - FeO - Al_2O_3 for relevant mantle aggregates; namely, harzburgite [10], chondrite [33], pyrolite [67], peridotite [39], and perovskitic only [109].

Although the Fe-Mg partitioning coefficient $K_D = \frac{x/(1-x-z)}{y/(1-y)}$ between bdg and fp, is expected to vary throughout the lower mante because of spin crossover [49, 76], we have examined compositions with a uniform K_D with values of 0.5 and 0.25. For the aggregates shown in this manuscript, a K_D of 0.5 was used as it's more consistent with those reported by [49] and [76]. Aggregate adiabats with K_D of 0.25 are shown in the appendix chapter - Figure A.9. Also, we show in Tables 3.1 and 3.2 the weight, molar, and volume percentages of oxides and minerals in the aggregates considered, and in Tables 3.3 and 3.4 their corresponding adiabats.

The isentropes of different minerals and aggregates were found from their isentropic gradients computed as,

$$\left(\frac{\partial T}{\partial P}\right)_S = \frac{\alpha_{agg} V_{agg} T}{C_{p_{agg}}} \tag{3.1}$$

where the aggregate quantities $V_{agg} = \sum_i \zeta_i V_i$, $\alpha_{agg} = \sum_i \alpha_i \zeta_i V_i / V_{agg}$, and $C_{p_{agg}} = \sum_i \zeta_i C_{p_i}$ are the aggregate volume, thermal expansion coefficient, and isobaric specific heat, respectively. Here, ζ_i, V_i, α_i, and Cp_i represent respectively the molar fraction, molar volume, thermal expansion coefficient, and isobaric specific heat of the i^{th} mineral in the mixture. All the isentropes, here loosely referred as geotherms, were compared with the adiabatic [15] and superadiabatic [4] geotherms. Once these geotherms were obtained, we computed aggregate velocities along aggregate specific geotherms using the Voigt-Reuss-Hill (VRH) average of elastic moduli and compared with PREM values [29].

Uncertainties resulting from our *ab initio* calculations due to k-point sampling, energy cutoff, and exchange correlations, are systemic in nature. Therefore, if such uncertainties induced further uncertainties in the calculated temperature profiles, these were consistently introduced in each of the minerals of a given aggregate. Thus, the overall conclusion of this study is unlikely to change irrespective of such uncertainties.

3.3 Results and Discussion

3.3.1 Lower mantle mineral isentropes

To unravel the possible consequences of the iron spin crossover in fp (and bdg) on the lower mantle geotherm, first we calculated using equation (3.1), the isentropes of $(Mg_{0.875}Fe_{0.125})SiO_3$, $(Mg_{0.875}Al_{0.125})(Si_{0.875}Al_{0.125})O_3$, $(Mg_{0.875}Fe^{3+}_{0.125})(Si_{0.875}Al_{0.125})O_3$, $(Mg_{0.875}Fe^{3+}_{0.125})(Si_{0.875}Fe^{3+}_{0.125})O_3$, $CaSiO_3$, and $(Mg_{0.8125}Fe_{0.1875})O$, with iron in high spin (HS) state and in a mixed spin (MS) state of HS and low spin (LS) states (See Figure 3.1 and table 3.3). Here, temperature differences among all the different bdgs in HS are only about ~ 2 K at 125 GPa, while differences with bdg in MS state (~ 50 K) and $CaSiO_3$ (~ 20 K) were more significant (See Figure 3.1a). For fp however, the isentropes in MS and HS states differ by ~ 260 K at deep lower mantle pressures (Figure 3.1a). Hence, spin crossover in fp induces the most dramatic effect on the lower mantle temperature profile. The anomalies caused by the spin crossover on V,α, and C_p (See Figures 3.1b to 3.1d) on the adiabatic gradient of fp (Figure 3.1e) are responsible for such temperature increase. Note that for α and C_p, the spin crossover anomalies correspond to broad peaks at similar pressure ranges, but do not cancel during the adiabatic gradient integration owing to significant differences in their magnitudes (Figures 3.1c and 3.1d).

3.3.2 Effect of Mg/Si ratio and fp spin crossover on the geotherm

We now investigate the isentropes of aggregates likely to be present in the lower mantle. Their compositions are shown in Figure 3.2. The horizontal charts in Figure 3.2a) represent the oxides mol% of SiO_2 - MgO - CaO - FeO - Al_2O_3 in the aggregate, while the pie charts in Figure 3.2b) show the mol% of each mineral (bdg, fp, CaPv) in the aggregate (See also tables 3.1 and 3.2). Each composition is characterized by its Mg/Si molar ratio, and it is clear that as Mg/Si decreases, so does the amount of fp.

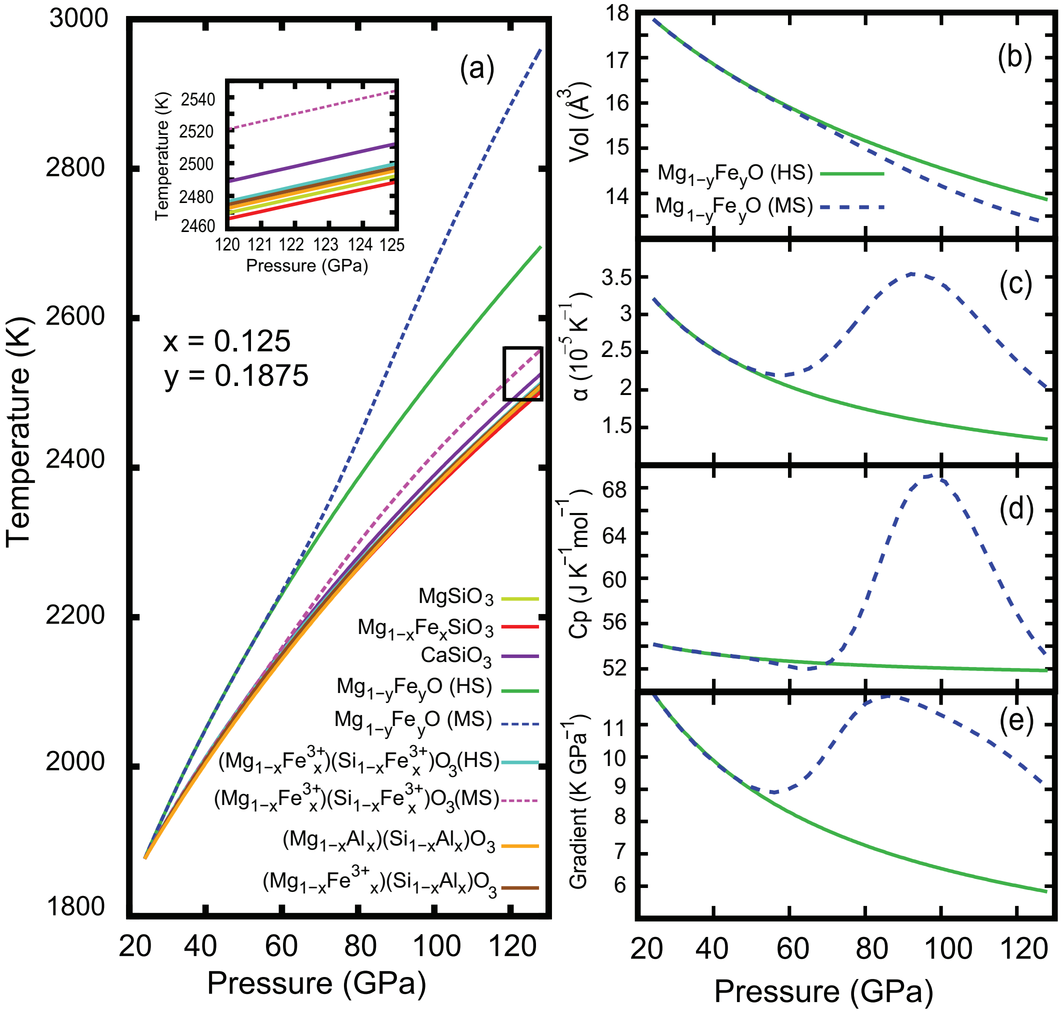

Figure 3.1: (a) Isentropes for bdg (HS and MS), CaPv, and fp in HS and MS states. Inset corresponds to highlighted region. (b) Volume, (c) thermal expansion coefficient (α), (d) isobaric specific heat (C_P), and (e) adiabatic gradient for fp in HS and MS states.

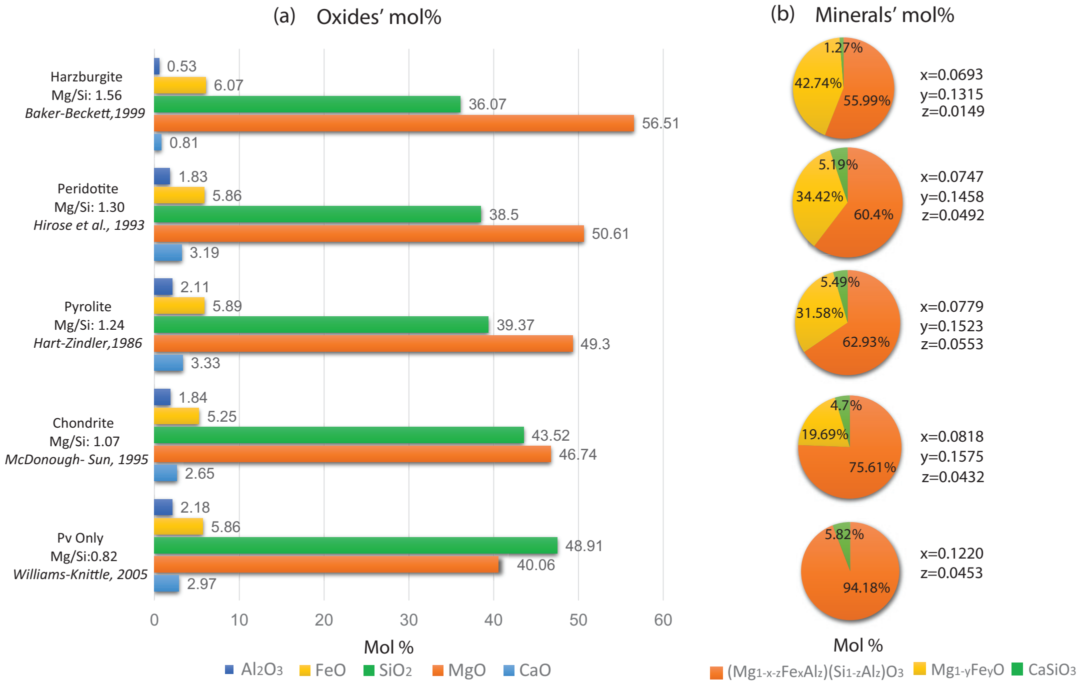

Figure 3.2: Aggregates characterized by their Mg/Si ratio. a) Mol% of oxides and b) minerals in each aggregate. All aggregates have a constant partitioning coefficient K_D of 0.5. The x, y, and z values determine the iron and aluminum concentration in bdg and iron in fp.

Table 3.1: Fundamental oxides for lower mantle compositions. *MgO moles were further modified to avoid excess of this oxide

	Perovskite [109] (Mg/Si: 0.82) Only		Chondrite [33] (Mg/Si: 1.07)		Pyrolite [67](Mg/Si: 1.24)		Peridotite [39] (Mg/Si: 1.30)		Harzburgite [10] (Mg/Si: 1.56)	
	Mol %	Wt %	Mol %	Wt %	Mol %	Wt %	Mol %	Wt %	Mol%	Wt %
CaO	2.97	3	2.65	2.82	3.33	3.55	3.19	3.44	0.81	0.91
MgO	40.06*	31.18	46.74	35.68	49.3	37.8	50.61	39.22	56.51	45.73
SiO_2	48.91	52.83	43.52	49.52	39.37	45	38.50	44.48	36.07	43.51
FeO	5.86	7.58	5.25	7.14	5.89	8.05	5.86	8.1	6.07	8.76
Al_2O_3	2.18	4	1.84	3.56	2.11	4.09	1.83	3.59	0.53	1.09

Table 3.2: Lower mantle minerals in different aggregates. The Vol % values are given at *Brown and Shankland*[1981] anchoring conditions.

	Perovskite Only (Mg/Si: 0.82) $x = 0.1220, z = 0453$			Chondritic (Mg/Si: 1.07) $x = 0.0818, y = 0.1575, z = 0432$			Pyrolite (Mg/Si: 1.24) $x = 0.0779, y = 0.1523, z = 0.0553$			Peridotite (Mg/Si: 1.30) $x = 0.0747, y = 0.1458, z = 0.0492$			Harzburgite (Mg/Si: 1.56) $x = 0.0693, y = 0.1315, z = 0.0149$		
	Mol %	Vol %	Wt %	Mol %	Vol %	Wt %	Mol %	Vol %	Wt %	Mol %	Vol %	Wt %	Mol %	Vol%	Wt %
$(Mg_{1-x-z}\ Fe^{2+}_x Al_z)(Si_{1-z}Al_z)O_3$	94.18	93.54	93.55	75.61	84.16	84.44	62.93	75.43	75.88	60.4	73.8	74.33	55.99	72.87	73.74
$(Mg_{1-y}Fe_y)O$	0	0	0	19.69	9.97	9.64	31.58	17.21	16.64	34.41	19.11	18.45	42.74	25.28	24.37
$CaSiO_3$	5.82	6.46	6.45	4.7	5.85	5.92	5.49	7.36	7.47	5.19	7.09	7.22	1.27	1.85	1.89

In what follows, we did not include Fe_2O_3 in any of the aggregates since the oxygen fugacity of the deep mantle, and thus the amount of ferric iron (Fe^{3+}), is still an open question beyond the scope of this manuscript. However, we investigated the possible effect of spin crossover in bdg on a pyrolitic composition (See Figure A.10). Here, we assumed that all iron in bdg is ferric and equally distributed into its A and B sites. Spin crossover in bdg increases the temperature by $\sim$ 13 K in this case. Furthermore, in the presence of Al_2O_3, ferric iron is expected to enter into the A site of bdg and spin crossover gets suppressed in this case [42,45,82,85]. Moreover, as it was shown in Figure 3.1a), the isentropes of $(Mg_{1-x}Fe_x^{3+})(Si_{1-x}Al_x)O_3$ and $(Mg_{1-x}Fe_x^{2+})SiO_3$ only differ by $\sim$ 6 K at 125 GPa, and therefore, the aggregate adiabats between these cases will not vary significantly.

We used the CaPv thermoelastic properties from [52, 53], which are not in the best agreement with recent experimental results conducted by [92] (Figure 2.7). This choice of CaPv was made for consistency since [52, 53] reported a shear modulus, which not only is significantly smaller than that reported by [91] (Figure 2.7), but also helped to reduce discrepancies with PREM values for all aggregates containing CaPv. Besides, the CaPV parameters reported by [92] did not introduce any major difference (less than $\sim$ 2 K at 125 GPa) when implemented to calculate the aggregate adiabat (Figure A.5).

We first examined the temperature increments caused by the spin crossover in all aggregates in which fp does (MS) and does not (HS) undergo spin crossover (Figure 3.3). Adiabatic geotherms and gradients (insets) are shown in Figures 3.3a to 3.3d. The temperature differences between HS and MS at high pressures (P $\sim$ 125 GPa) for harzburguite ($\sim$ 50 K) were greater than those for peridotite ($\sim$ 40 K), pyrolite ($\sim$ 30 K), and chondrite ($\sim$ 20 K) owing to harzburgite's higher Mg/Si. We also notice that MS gradients (insets) for all aggregates deviate from HS at pressures of $\sim$ 60 GPa, as a consequence of the spin crossover, and the gradient decreases in proportion to the Mg/Si ratio.

The isentropes of all aggregates were compared with reference geotherms by Brown and Shankland [15] and Anderson [4] in Figure 3.4 (See also Table 3.4). All calculated adiabats were anchored to 1873 K at 23 GPa (See [1, 15]). At deep lower mantle conditions, harzburgite achieves the highest temperature, which is about $\sim$ 200 K higher than that of B&S. Temperatures then decrease with Mg/Si ratio, i.e., the aggregate's

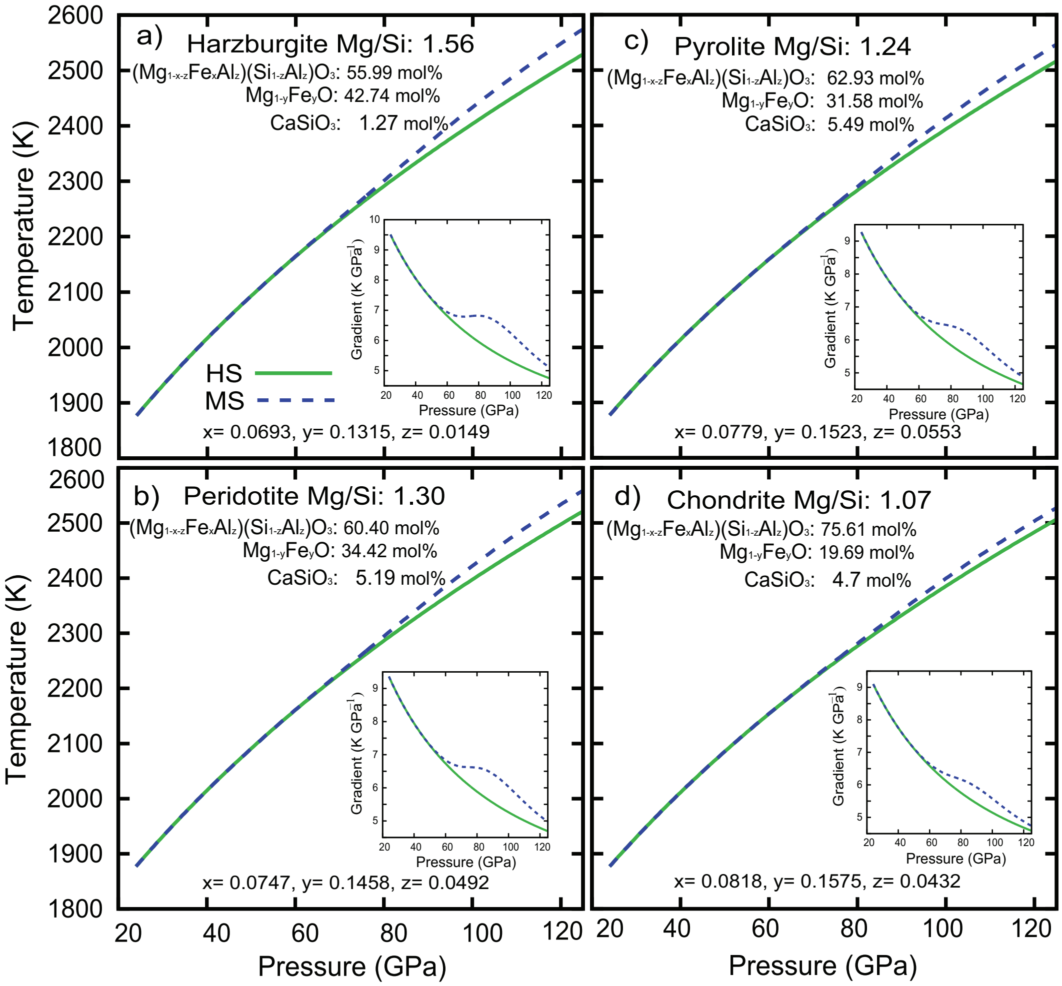

Figure 3.3: Adiabats for a) harzburgite, b) peridotite, c) pyrolite, and d) chondrite with fp in HS and MS states. The x, y, and z values determine the iron and aluminum concentration in bdg and fp. Solid/dashed lines correspond to adiabats with fp in HS/MS states. Inset figures show the adiabatic gradient for each aggregate.

fp fraction. Such temperature variations are also expected when K_D is reduced, i.e., fp containing a higher iron content. For this scenario, the crossover anomaly in the adiabat variables (α, C_p, and V) will be more pronounced and consequently leading to hotter temperatures (See Figure A.10).

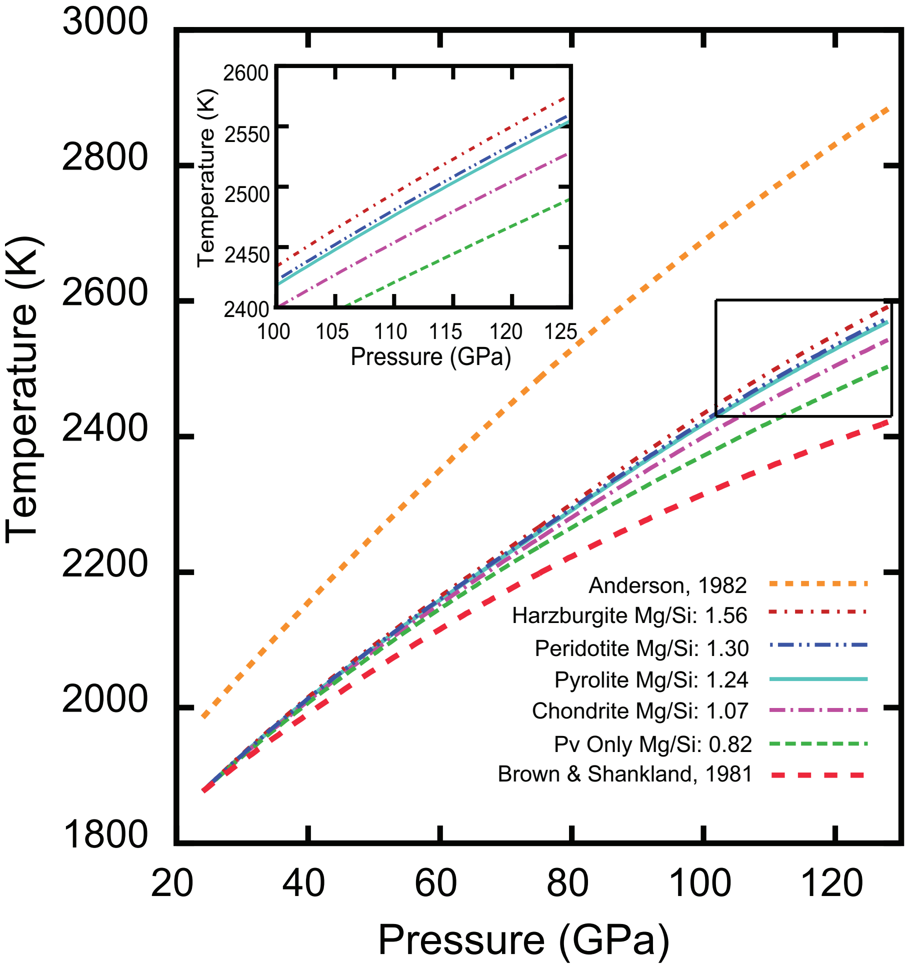

Figure 3.4: Calculated adiabats for aggregates considered, compared with geotherms by Brown and Shankland [15] and Anderson [4]. Inset corresponds to highlighted region.

Table 3.3: Adiabats for lower mantle minerals. $x = 0.125$, $y = 1875$.

Pressure (GPa)	$Mg_{1-y}Fe_yO$ HS Temperature (K)	$Mg_{1-y}Fe_yO$ MS Temperature (K)	$Mg_{1-x}Fe_xSiO_3$ Temperature (K)	$CaSiO_3$ Temperature (K)	$Mg_{1-x}Al_xSi_{1-x}Al_xO_3$ Temperature (K)	$Mg_{1-x}Fe^{3+}_xSi_{1-x}Al_xO_3$ Temperature (K)	$Mg_{1-x}Fe^{3+}_xSi_{1-x}Fe^{3+}_xO_3$ HS Temperature (K)	$Mg_{1-x}Fe^{3+}_xSi_{1-x}Fe^{3+}_xO_3$ MS Temperature (K)
23	1873.00	1873.00	1873.00	1873.00	1873.00	1873.00	1873.00	1873.00
30	1945.85	1945.85	1927.92	1929.92	1926.64	1928.98	1930.73	1930.73
40	2050.38	2050.38	2006.76	2011.78	2004.37	2013.12	2012.58	2012.58
50	2144.59	2144.59	2078.87	2086.67	2076.35	2082.61	2086.27	2086.27
60	2230.87	2238.41	2145.39	2155.80	2143.44	2150.12	2153.49	2158.94
70	2310.84	2328.82	2207.19	2220.08	2206.31	2212.77	2215.53	2230.74
80	2385.71	2438.50	2264.98	2280.21	2265.46	2271.30	2273.39	2298.63
90	2456.34	2556.66	2319.33	2336.73	2321.34	2326.30	2327.85	2361.14
100	2523.40	2672.30	2370.71	2390.09	2374.28	2378.28	2379.54	2418.42
110	2587.40	2782.20	2419.51	2440.64	2424.58	2427.64	2428.97	2471.22
120	2648.73	2884.95	2466.06	2488.70	2472.50	2474.73	2476.55	2520.52
125	2678.49	2932.98	2488.58	2511.87	2495.63	2497.51	2499.77	2544.09

Table 3.4: Adiabats for lower mantle aggregates with fp in MS state.

Pressure (GPa)	Perovskite Only Temperature (K)	Chondritic Temperature (K)	Pyrolite Temperature (K)	Peridotite Temperature (K)	Harzburgite Temperature (K)
23	1873.00	1873.00	1873.00	1873.00	1873.00
30	1932.13	1929.22	1930.41	1930.68	1931.48
40	2006.98	2010.09	2012.95	2013.61	2015.54
50	2079.23	2084.19	2088.48	2089.49	2092.40
60	2145.90	2152.93	2158.65	2160.00	2163.88
70	2207.87	2217.89	2225.58	2227.35	2232.48
80	2265.81	2280.71	2291.51	2293.89	2300.87
90	2320.31	2341.61	2356.45	2359.60	2368.91
100	2371.83	2399.52	2418.43	2422.36	2434.03
110	2420.76	2453.75	2476.13	2480.73	2494.50
120	2467.42	2504.39	2529.47	2534.62	2550.08
125	2489.98	2528.54	2554.69	2560.07	2576.23

The relative temperature differences $\Delta T/T$ between fp in MS and HS states from geodynamic simulations as in [13,103], are in overall agreement with our predictions despite the differences in the details of the aggregate's K_D and calculations. For instance, simulations by Bower et al. [13] using $Mg_{83}Fe_{17}O$, indicated a maximum relative temperature difference $\Delta T/T$ of $\sim 10\%$ at 113 GPa (~ 2500 km depth). As shown in Figure 3.1a), the temperature difference at 113 GPa between fp in MS and HS states is about ~ 200 K, which corresponds to a $\Delta T/T \sim 8\%$. Given the different nature and details of these calculations the agreement is outstanding. Furthermore, at the same pressure of 113 GPa, geodynamic simulations by Vilella et al. [103] inferred a MS - HS temperature difference of ~ 20 K ($\Delta T/T \sim 0.6\%$) and 50 K ($\Delta T/T \sim 1.6\%$) for Al-bearing and Al-free pyrolite aggregates, respectively. Our results showed a temperature increment of ~ 27 K, which corresponds to $\Delta T/T \sim 1.1\%$, for both Al-bearing (Figure 3.3c) and Al-free pyrolite. However, the MS - HS comparisons by Vilella et al. [103] were done for the same aggregate with different K_D, i.e., their Al-free pyrolite in HS had a K_D of 0.4 and in MS of 0.02, while for Al-bearing pyrolite, K_D was 0.5 and 0.4 for HS and MS, respectively. Despite the differences in details there is also a good overall agreement in this case.

3.4 Geophysical Significance

The elastic moduli (K_S,G), acoustic velocities (V_P,V_ϕ,V_S), and densities (ρ) of all the aggregates along their own isentropes are shown in Figure 3.5. In aggregates containing fp, K_S softening due fp spin crossover (See [112, 113]) is observed and varies proportionally to the Mg/Si ratio (Figure 3.5a). Moreover, G does not exhibit any anomalous behavior and its value for different compositions converges to similar values at deep lower mantle pressures. For aggregates with higher Mg/Si ratio, calculated G revealed a better agreement with PREM values, while the K_S values for chondrite and pyrolite were closer to PREM values (Figure 3.5a). The signature of K_S anomalies were also obvious in the compressional ($V_p = \sqrt{(K_S + \frac{4}{3}G)/\rho}$) and bulk ($V_\phi = \sqrt{K_S/\rho}$) velocities, while shear velocities $V_S = \sqrt{G/\rho}$ were unaffected (See Figure 3.5b). The relative velocity deviations ($\Delta V_P\%$, $\Delta V_\phi\%$, and $\Delta V_S\%$) from PREM values are shown in Figure 3.5c). $\Delta V_P\%$ and $\Delta V_\phi\%$ decreased with increasing Mg/Si ratio, and reached negative values mainly due fp spin crossover. However, $\Delta V_S\%$ for all the aggregates was positive and the deviations from PREM values for pyrolite, perditotite, and harzburgite were the lowest (Less than 1%). The relative density deviations ($\Delta\rho$) reduced with increasing pressure (Figure 3.5c). For compositions with fp, the volume collapse caused by fp spin crossover [106], seemed to reduce such deviations further.

Moreover, as discussed in section 3.3.2, the iron spin crossover in fp raises the aggregate's geotherm in proportion to its fp content (or to the iron content in fp). This temperature boost can affect analyses of the lower mantle composition. Figures 3.6a) and 3.6a') show peridotite and pyrolite's elastic moduli along their own geotherms and the B&S geotherm. Although not substantial, relative deviations from PREM varied depending on the geotherm used. For the bulk modulus $\Delta K_S\%$ in Figures 3.6b) and 3.6b'), the relative deviations from PREM were the same along both geotherms until pressures lower than 80 GPa, while for the shear modulus relative deviations $\Delta G\%$, results along the self-consistent geotherm (Figures 3.6c and 3.6c') exhibited lower deviations from PREM throughout the whole lower mantle. Such details suggest that the aggregate thermoelastic properties along the self-consistent geotherm should sharpen uncertainties in analyses of lower mantle composition.

3.5 Conclusions

We presented a set of adiabatic geotherms for individual minerals and likely lower mantle aggregates under realistic pressure and temperature conditions. We showed that the spin crossover in ferropericlase introduces an anomaly in its isentrope similar to "superadiabaticity". This effect increased the adiabatic temperature gradient in different aggregates in proportion to their ferropericlase content or Mg/Si ratio. Velocities of aggregates with compositions varying from perovskitic to harzburgitic along their self-consistent geotherms exhibited deviations from PREM velocities within $\pm \sim 2\%$. However, pyrolitic and peridotitic compositions displayed the best fit with respect to PREM values. The elastic moduli, velocities, and densities of these aggregates along their own self-consistent geotherms tend to display smaller deviations from PREM (up to $\sim 1\%$ less), than those along standard geotherms such as Brown and Shankland [15]. Results from this chapter can also be found in [101].

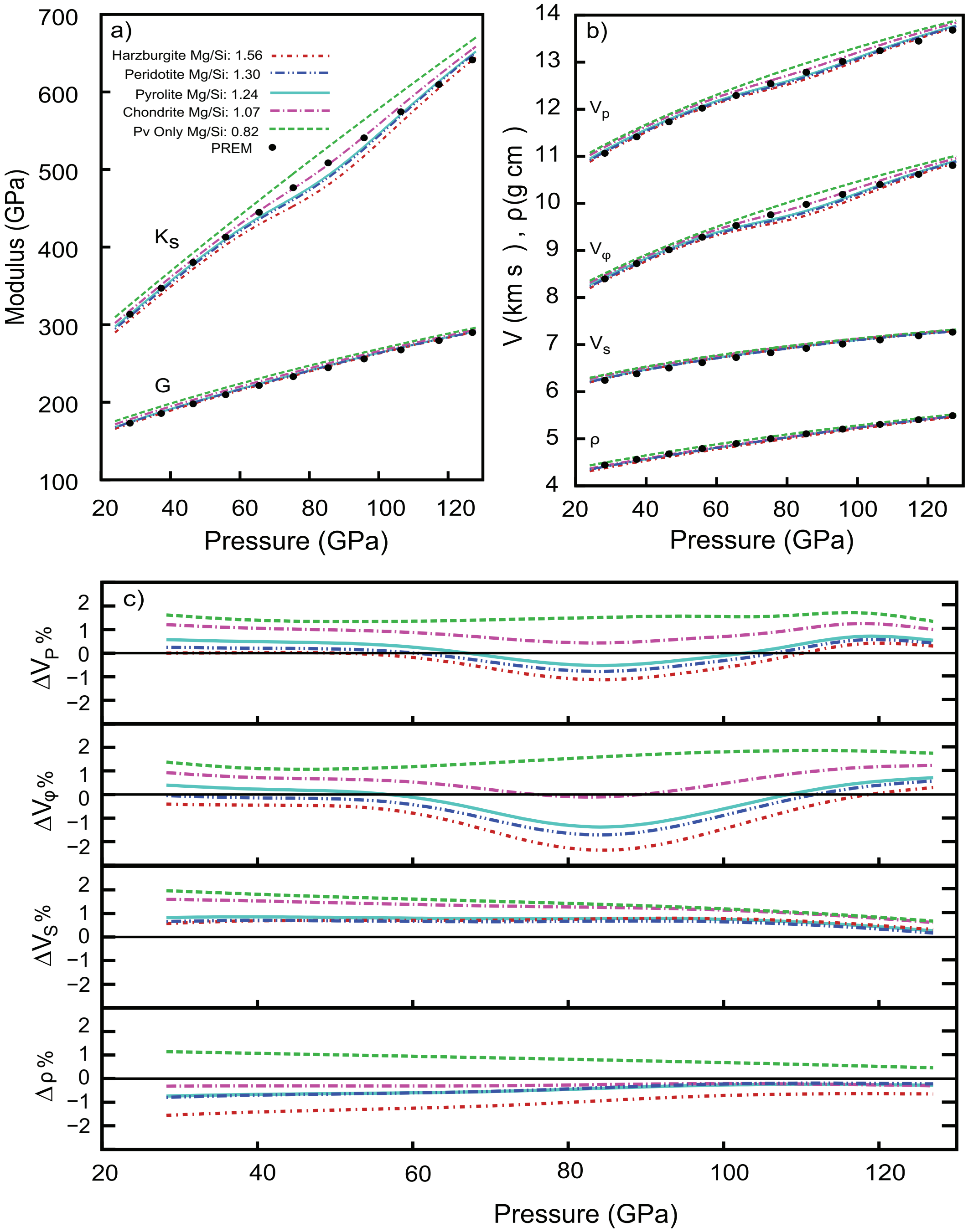

Figure 3.5: (a) Elastic moduli (K_S, G), (b) acoustic velocities (V_P, V_ϕ, V_S) and densities (ρ) for all aggregates considered. Black circles indicate PREM values [29]. (c) Relative deviations from PREM shown as percentages.

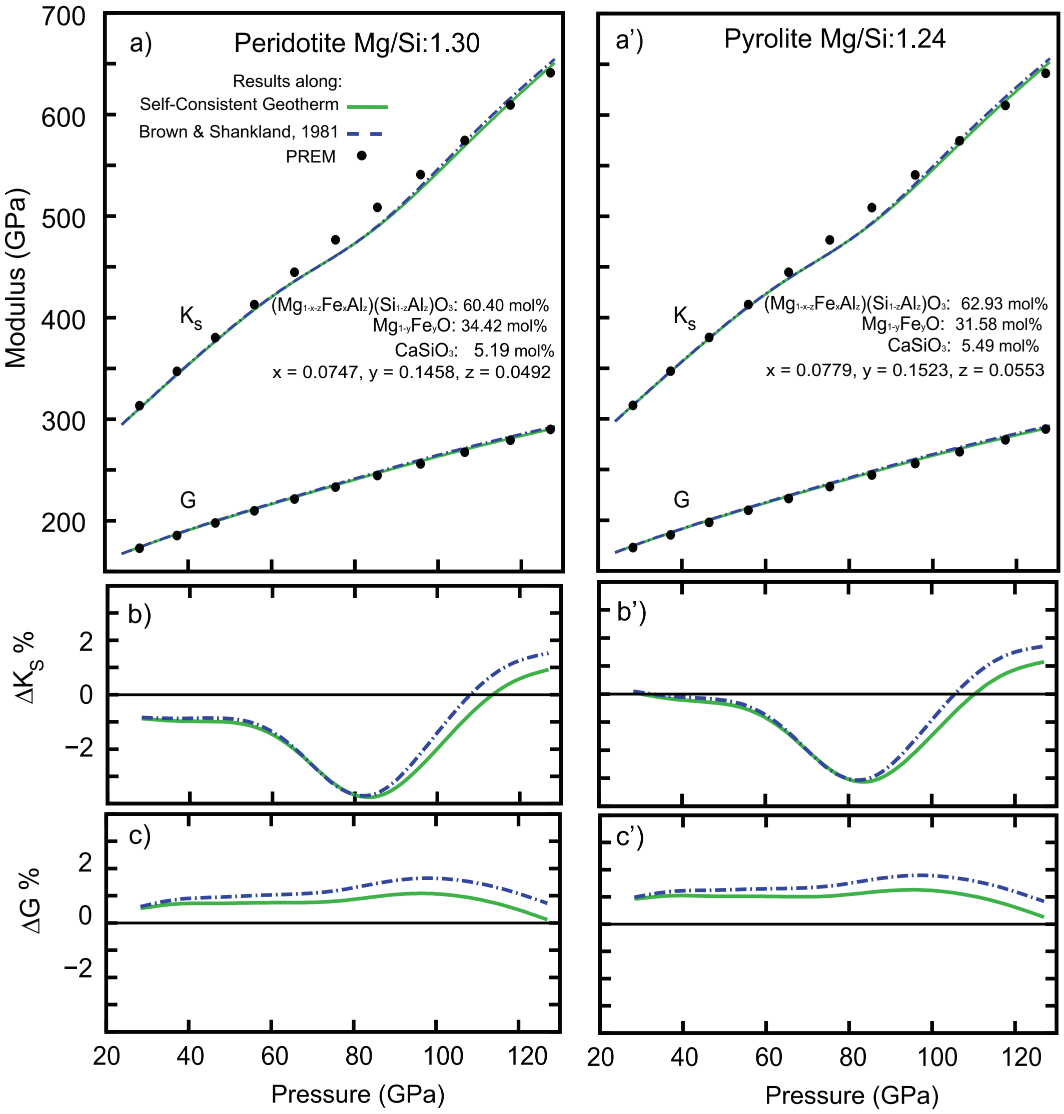

Figure 3.6: Elastic moduli (K_S, G) for (a) peridotite, and (a') pyrolite along self-consistent (solid green line) and [15] (dashed blue line) geotherms. Black circles correspond to PREM values [29]. (b)/(b') and (c)/(c') are the elastic moduli relative deviations ($\Delta K_S\%$, $\Delta G\%$) with respect to PREM values, shown as percentages for peridotite/pyrolite.

Chapter 4

Bullen's parameter as a seismic observable for spin crossovers in the lower mantle

Elastic anomalies produced by the spin crossover in ferropericlase have been documented by both first principles calculations and high pressure-temperature experiments. The predicted signature of this spin crossover in the lower mantle is, however, subtle and difficult to geophysically observe within the mantle. Indeed, global seismic anomalies associated with spin transitions have not yet been recognized in seismologic studies of the deep mantle. A sensitive seismic parameter is needed to determine the presence and amplitude of such a spin crossover signature. In this chapter, the effects of spin crossovers on the Bullen's parameter, η, are assessed for a range of compositions, thermal profiles, and lateral variations in temperature within the lower mantle. Velocity anomalies associated with the spin crossover in ferropericlase span a depth range near 1,000 km for typical mantle temperatures. Positive excursions of Bullen's parameter with a maximum amplitude of ~ 0.03 are calculated to be present over a broad depth range within the mid-to-deep lower mantle: these are largest for peridotitic and harzburgitic compositions. These excursions are highest in amplitude for model lower mantles with large lateral thermal variations, and with cold downwellings having longer lateral length-scales relative to hot upwellings. We conclude that predicted deviations in

Bullen's parameter due to the spin crossover in ferropericlase for geophysically relevant compositions may be sufficiently large to resolve in accurate seismic inversions of this parameter, and could shed light on both the lateral variations in temperature at depth within the lower mantle, and the amount of ferropericlase at depth.

4.1 Introduction

The adiabatic nature of the convecting mantle is a frequently used concept in the geophysical sciences. For instance, equation of state parameters, which are used to calculate the elastic and thermodynamic properties of minerals at mantle conditions, are commonly assumed to be adiabatic within the convecting mantle, e.g., the adiabatic bulk modulus and its derivative. However, various geodynamic simulations and seismological models [19,29,54,64–66] suggest that the mantle is regionally nonadiabatic, particularly in the shallow and deep mantle regions, and in some cases, at mid lower mantle pressures. The latter is important because deviations from adiabaticity within the mantle provide insights into temperature gradients, heat flux, thermal history, thermal boundary layers, phase transitions, chemical stratification, and compositional heterogeneities. Therefore, knowledge about the degree of adiabaticity of the mantle helps us to constrain its composition and thermal structures related to mantle convection [65].

A common observable that quantifies the adiabaticity level of the mantle is Bullen's parameter, η. Introduced and developed by Bullen [17,18], η is a measure of the ratio between the actual density increase with pressure within the Earth (as constrained by a combination of seismology, the Earth's moment of inertia, and mass) with respect to the profile derived from adiabatic self-compression. As such, it is expected to be unity where the mantle is homogeneous, adiabatic, and free of phase transitions. Thus, deviations of η from unity (generally $\sim \pm 0.1$ or less), indicate super(sub)adiabatic regions, and consequently, the presence of thermal boundary layers, compositional variations, or phase transitions. Moreover, there is also the possibility that due to internal heating within the mantle, the mantle may be systematically subadiabatic [19].

Evaluations of η in geodynamic simulations are generally done by probing the parameter space associated with plausible convection models. This includes examining the effects of possible variations of the thermal conductivity, thermal expansion coefficient, viscosity, internal heating, and heat flux from the core, each of which directly impact the inferred geotherms [19, 65, 66]. For instance, if internal heating is relatively significant, subadiabaticity is expected. Additionally, differences in elastic properties between individual phases within an aggregate can also produce variations in Bullen's parameter, and hence apparent deviations from adiabaticity. This is a bulk attenuation effect. Specifically, bulk attenuation phenomena are attributed to internal shear stresses generated from the local mismatch of the elastic moduli of neighboring grains in a given aggregate. One formulation of bulk attenuation by Heinz et al. [34] characterizes it through the ratio of the adiabatic bulk modulus K_S and an effective modulus (Reuss bound) K_E, since the mantle can be assumed to be under hydrostatic pressure. Attenuation is a complicated problem to tackle, because it involves calculating complex moduli with an associated time dependency [16, 34, 35]. Such bulk attenuation effects are beyond the scope of this study, since the calculations we conduct are not time-dependent, but certainly needs to be addressed to understand systematic deviations of Bullen's parameter from 1. Here, we study how anomalies in bulk modulus induced by spin crossovers affect the Bullen's parameter, and hence inferred adiabaticity of the lower mantle.

Elastic anomalies produced by the spin crossover in ferropericlase (fp) and bridgmanite (bdg), have been documented by both first principles calculations and high pressure-temperature experiments [6, 9, 24, 42, 45, 61, 71, 82, 85, 89, 100, 106, 111–113]. The predicted signatures of this spin crossover in the lower mantle are subtle. Despite the fact that thermally induced velocity heterogeneities associated with this spin crossover appear to correlate statistically with seismic tomographic patterns observed in deeply rooted plumes [113], spherically averaged anomalies have not yet been recognized in seismologic studies of the deep mantle. This may be due to difficulties associated with resolving gradual changes in the slopes of seismic velocities as a function of depth, and the trade-offs involved in seismic inversions of depth-dependent velocity and density structures. In particular, velocity anomalies associated with the spin crossover in fp are anticipated to span a depth range greater than 1000 km at mantle temperatures. Thus, a sensitive seismic parameter is needed to determine the presence or absence of this spin crossover signature, which would in turn shed light on the amount of ferropericlase in the lower mantle. Bullen's parameter η is an ideal candidate as it relates seismic wave speeds with density variations, and sensitively records deviations from adiabaticity. Moreover, deviations from Bullen's parameter can be readily identified because it has a clear reference value (unity) in an adiabatic mantle that is heated from below. We calculated one dimensional perturbations of η due to changes in composition, temperature, and spin crossover. We achieved this by computing η of different relevant mantle aggregates along their own adiabats. We also approximate lateral variations in temperature by modeling differing areas and temperature differences between upwellings and downwellings. The mantle phases of the aggregates considered are bridgmanite (bdg: Al- Fe- bearing $MgSiO_3$ perovskite), $CaSiO_3$ perovskite (CaPv), and ferropericlase (fp: (Mg,Fe)O). The aggregates have Mg/Si ratios that range from 0.82 to 1.56 and are harzburgite (Mg/Si $\sim$ 1.56) [10], chondrite (Mg/Si $\sim$ 1.07) [33], pyrolite (Mg/Si $\sim$ 1.24) [67], peridotite (Mg/Si $\sim$ 1.30) [39], and perovskite only (Mg/Si $\sim$ 0.82) [109]. The predicted deviations in η due to the spin crossover are comparable to previously reported variations [19, 64–66], and may be sufficiently large to turn up in accurate seismic inversions of this parameter.

4.2 Method and Calculation Details

We used bdg $Mg_{1-x}Fe^{2+}_xSiO_3$, $(Mg_{1-x}Al_x)(Si_{1-x}Al_x)O_3$, $(Mg_{1-x}Fe^{3+}_x)(Si_{1-x}Al_x)O_3$, $(Mg_{1-x}Fe^{3+}_x)(Si_{1-x}Fe^{3+}_x)O_3$ ($x = 0$ and 0.125) and fp $Mg_{1-y}Fe_yO$ ($y = 0$ and 0.1875) thermoelastic properties from [82, 86] and [112]. Results for other x and y values were obtained by linear interpolation. All compositions account for the spin crossover in fp unless otherwise noted, i.e., bdg's iron (ferrous and/or ferric) is in the high spin (HS) state and fp is in a mixed spin (MS) state of HS and low spin (LS) states. For CaPv, we used thermoelastic properties from [52, 53], which were reproduced within the Mie-Debye-Grüneisen [90] formalism. The mantle aggregates in this study, namely, harzburgite [10], chondrite [33], pyrolite [67], peridotite [39], and perovskititic only [109], are mixtures within the SiO_2 - MgO - CaO - FeO - Al_2O_3 system (ignoring alkalis and TiO_2 is not anticipated to resolvably affect the results). In addition, the Fe-Mg partition coefficient $K_D = \frac{x/(1-x-z)}{y/(1-y)}$ between bdg and fp, which is known to be affected by the spin crossover [49, 76], was assumed to be uniform throughout the mantle with a value of 0.5. Further details about these compositions can be found in chapter 3.

The adiabats of the different minerals and aggregates were integrated from their adiabatic gradient,

$$\left(\frac{\partial T}{\partial P}\right)_S = \frac{\alpha V T}{C_p} \tag{4.1}$$

We denote the molar fraction, molar volume, molar mass, thermal expansion coefficient, and isobaric specific heat of the ith mineral in the mixture as ζ_i, V_i, M_i, α_i, and Cp_i respectively. The aggregate properties such as volume, thermal expansion coefficient, and isobaric specific heat are then $V = \sum_i \zeta_i V_i$, $\alpha = \sum_i \alpha_i \zeta_i V_i / V$, and $C_p = \sum_i \zeta_i C_{p_i}$. The adiabatic aggregate bulk moduli K_S were obtained from the Voigt-Reuss-Hill (VRH) average. Moreover, the aggregate density $\rho = \sum_i \zeta_i M_i / V$ and seismic parameter $\phi = K_S/\rho$ were calculated along the aggregate adiabat, in order to compute adiabatic changes of density with respect to pressure as,

$$\eta = \phi \frac{d\rho}{dP} \tag{4.2}$$

where η is the Bullen's parameter. If $\eta = 1$ the mantle is homogeneous and adiabatic, whereas values of $\eta > 1$ can indicate a phase change as ρ varies more rapidly with depth than predicted by the adiabat. Furthermore, values of $\eta < 1$ may signify the presence of a thermal boundary layer or substantial internal heat production. Details about equation (4.2) can be found in chapter 2.

4.3 Results and Discussion

4.3.1 Observations of η in the lower mantle

Figure 4.1 shows different η calculations from previous geodynamic [19, 65, 66], seismic [28,29,54], and seismic plus mineral physics models with a priori starting conditions [64]. Overall, η oscillates between values of ~ 1.04 to 0.96 for most of these models, except for the AK135F model [54], which displays the largest fluctuations. AK135F exhibited an average value of $\eta \sim 0.92$ from 1000 km to 2700 km in depth, and variations in η above and below those depths were at least of the order of ~ 0.1, which is substantially larger than the other inversions and calculations. For other seismic models such as PEM [28] and PREM [29] such large fluctuations are not observed, but they could be suppressed by the continuity requirements of the polynomial formulations of these models. However, the Bullen's parameters of these seismic models do suggest the presence of a thermal boundary layer at the bottom of the lower mantle, as shown by the negative slope of all models in the bottommost hundred to few hundred km of the mantle. Notably, for the mineral physics plus inverse model calculation by Mattern et al. [64], η values less than one from 800 km to 1300 km were attributed to iron depletion from their initially pyrolitic compositional model.

Two and three dimensional geodynamic calculations of η were first done by Matyska and Yuen [65,66], where the effect of varying parameter space properties, such as thermal conductivity, thermal expansion coefficient, and viscosity, lead to different perturbations in η, but with an average value of ~ 1.01. This average value is in general agreement with other geodynamic calculations by Bunge et al. [19], which also showed that the presence of internal heat sources lead to subadiabatic regions. Other thermal contributions, like core heating, cause superadiabatic temperature gradients at the bottom of the mantle and thus the presence of a thermal boundary layer, as manifested by the negative slopes of η near the base of the mantle.

4.3.2 Spin-crossover effect on the adiabaticity of the lower mantle

We studied the effect of spin crossovers on lower mantle adiabaticity by examining η excursions for different lower mantle aggregates along their self consistent adiabats. All of the adiabats of the different aggregates are listed in Table 3.4 (See also [101]). Figure 4.2 and Table 4.1 shows the variations of η only due to the spin crossover in fp: only a portion of trivalent iron in bdg is anticipated to undergo a spin transition within the mantle (e.g., [22] and [42, 45]). For compositions with fp, fluctuations in η were ~ 0.02 max, which are well within the variations in seismological observations and geodynamical calulations shown in Figure 4.1. Furthermore, larger deviations from adiabaticity occur as the aggregate's Mg/Si ratio, i.e., fp content, is increased. The sensitivity to Mg/Si content of the Bullen's parameter maximum near 1900 km depth, induced by the spin crossover, is relatively large: peridotitic and harzburgitic compositions have an η anomaly which is nearly twice that of the chondritic composition. The η excursions for the perovskitic composition, Pv only, depict the profile of a composition without fp in

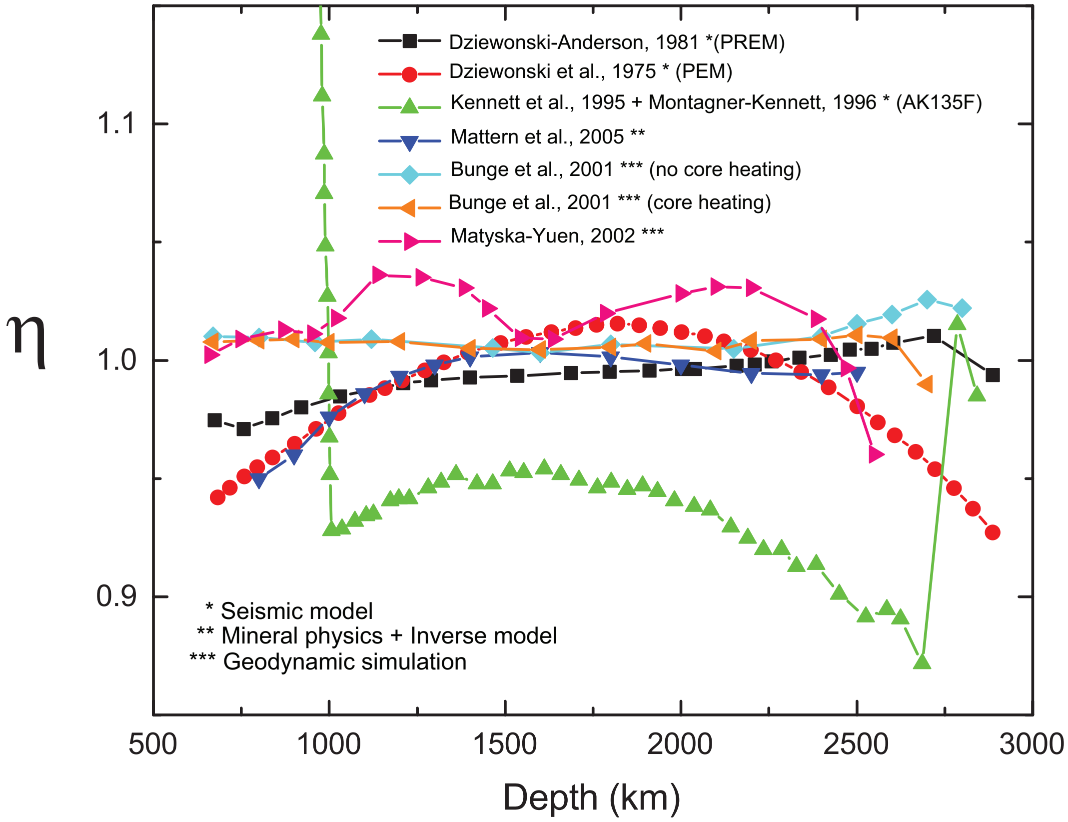

Figure 4.1: Bullen's parameter η calculations for seismic, geodynamic, and mineral physics models.

the lower mantle.

Table 4.1: Bullen's parameter η for aggregates with fp in MS state.

Pressure (GPa)	Perovskite Only η	Chondritic η	Pyrolite η	Peridotite η	Harzburgite η
23	0.9983	0.9989	1.0008	0.9990	0.9996
30	0.9983	0.9981	0.9996	0.9978	0.9981
40	0.9984	0.9974	0.9985	0.9967	0.9967
50	0.9985	0.9976	0.9985	0.9968	0.9968
60	0.9986	0.9987	0.9998	0.9986	0.9987
70	0.9987	1.0020	1.0041	1.0038	1.0046
80	0.9987	1.0073	1.0116	1.0125	1.0148
90	0.9990	1.0091	1.0145	1.0157	1.0187
100	0.9990	1.0054	1.0092	1.0097	1.0117
110	0.9991	1.0016	1.0036	1.0032	1.0038
120	0.9992	1.0002	1.0016	1.0007	1.0009
125	0.9992	1.0003	1.0016	1.0006	1.0007

4.3.3 Lateral temperature variations

We have characterized what Bullen parameter anomalies, due to spin crossovers, might generate for one-dimensional seismic models of an isochemical adiabatic mantle. However, the lack of maxima in most Bullen parameter observations (Figure 4.1) that are at the appropriate depth and have the right breadth to correspond to the spin crossover of fp, led us to probe the effect of lateral temperature variations on deviations of η. Since lateral temperature variations and their areal distribution at a given depth of hot/upwelling and cold/downwelling material are not well-constrained in the deep mantle (e.g., [41]), we conducted a sensitivity analysis for the effect of thermal variations on η in a pyrolitic mantle. Here, material at each depth is distributed along adiabats with potential temperatures above (hot) and below (cold) a reference adiabat pinned at 1873 K at 23 GPa as in [15] (B&S) (See also [1]). The lateral temperature variations between hot and cold regions that we probed were ± 250 K, ± 500 K, and ± 750 K in a sequence of 25%:75%, 50%:50% and 75%:25% ratio of the mantle at a given depth being hot:cold (See Figure 4.3).

For all the temperature-average distributions (Figures 4.3a, 4.3b, and 4.3c), we observed that the spin crossover anomalies, i.e. deviations from adiabaticity, became more prominent at lower temperatures: this is a natural consequence of the broadening of the spin transition that occurs at high temperatures. Conversely, greater amounts

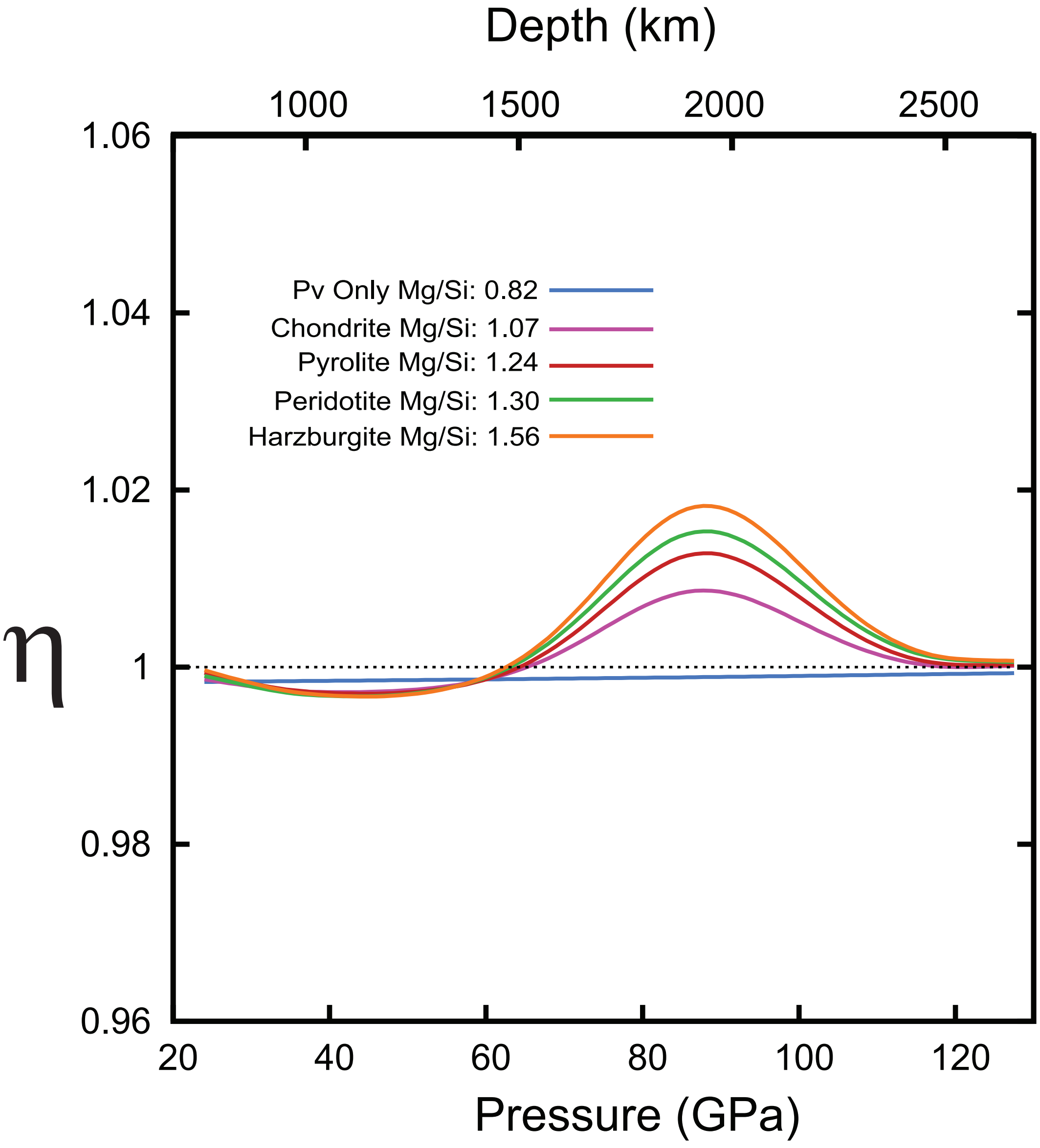

Figure 4.2: Perturbations of η due spin crossover in fp in lower mantle aggregates.

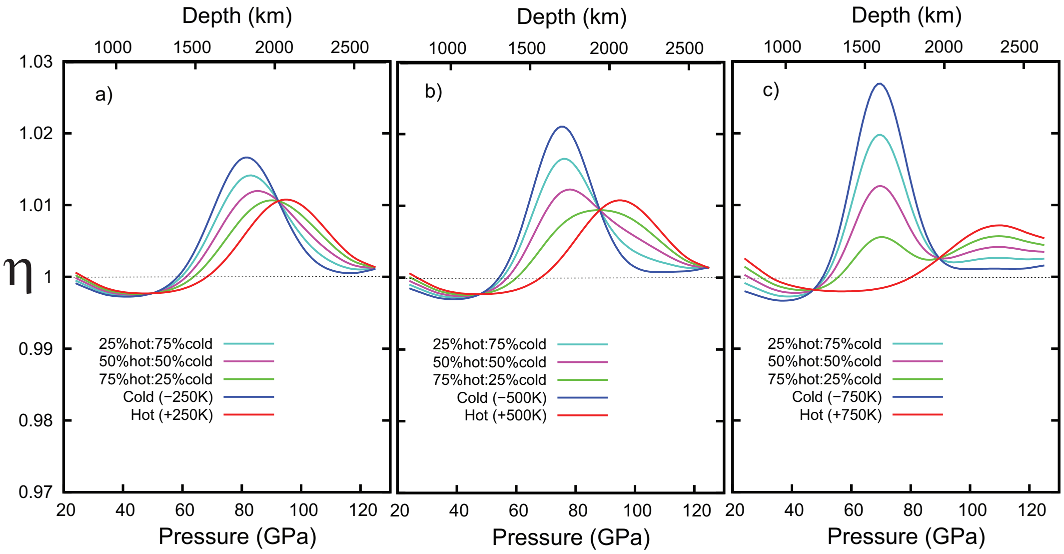

Figure 4.3: Lateral temperature variations of a) ± 250 K, b) ± 500 K, and c) ± 750 K for sequences of 25%:75%, 50%:50% and 75%:25% of the mantle being hot:cold. In accord with the two-state model for temperature that we have assumed, two isosbestic points are generated near 1250 km and 2000 km depth, respectively.

of hot material tend to make spin crossovers more difficult to resolve. Furthermore, we also observed that for large temperature variations, ± 750 K, two peaks in η can also be generated at different depths in an isochemical thermally heterogeneous mantle (Figure 4.3c). This phenomenon is attributed to the volume increase with temperature, which increases the pressures that are required for the spin crossover to occur. Since the amplitude of the perturbations in η increases also with higher fp content, it is expected that regions with larger cold harzburgitic chemistry present within the lower mantle, such as subducting slabs, should have substantially greater local fluctuations in the Bullen's parameter if a local vertical sampling of η over such regions is performed.

Beyond lateral temperature variations, we examined the case of coupled compositional and thermal lateral heterogeneities. The rationale here is that cold, downwelling subducted material is likely to have a larger concentration of harzburgite than ambient mantle. We utilized a similar temperature averaging scheme, but with cold η values being harzburgitic. Figure 4.4 shows different η profiles with the mantle being 75% hot(pyrolite) and 25% cold(harzburgite). For this scenario, perturbations in η due to the spin crossover vary their magnitude and reach a maxima at different depths, depending on the temperature difference between the cold downwellings of harzburgitic chemistry and ambient pyrolitic mantle. If the temperature difference is sufficiently large, e.g. ± 750 K, multiple peaks can be observed. Thus, the relative amplitudes and locations of multiple peaks could, if observed/observable, provide strong constraints on lateral variations in the geotherm and/or composition of the deep mantle. In particular, the depth at which the spin transition-induced peak occurs in Bullen's parameter is highly sensitive to temperature (Figure 4.3), while the amplitude of its variation is sensitive to composition (Figure 4.2).

4.4 Geophysical Significance

We have utilized η as an observable for spin crossovers in the lower mantle for the first time, in an attempt to reconcile mineral physics with seismic observations and to understand how such spin crossovers may affect observations of deviations from adiabaticity within the mantle. Our results suggest that the spin crossover signatures in η should be sufficiently large to turn up in accurate (ca. 1%) seismic inversions for this parameter. Whether such accuracies are achievable is unclear: several decades ago, Masters [63] concluded that η variations from seismic observations could be resolved with a precision no better than 2%. Recent results from an inverse Bayesian method, deployed via a neural network technique by de Wit and Trampert [26], showed that ρ, Vp, and Vs may each be resolvable to somewhat better than 1% in the $\sim$ 2000 km depth range, based on their observed probability density functions. A linear combination of these uncertainties will certainly lead to values of order 1-2.5% for the net uncertainty in 1-D inversions for Bullen's parameter. Nevertheless, given markedly improved and more accurate seismic inversions coupled with substantially larger data sets, it is possible that better constraints on η might be developed.

We also highlight the importance of the chosen temperature profile, as it has a direct impact on η. Elastic moduli, seismic velocities, and aggregate densities strongly depend on temperature. Hence, super(sub)adiabatic geotherms will lead to different interpretations of η. As showed in chapter 3 (See also [101]), the spin crossover in fp and bdg induces an increment in the adiabat's temperature of a given aggregate and such

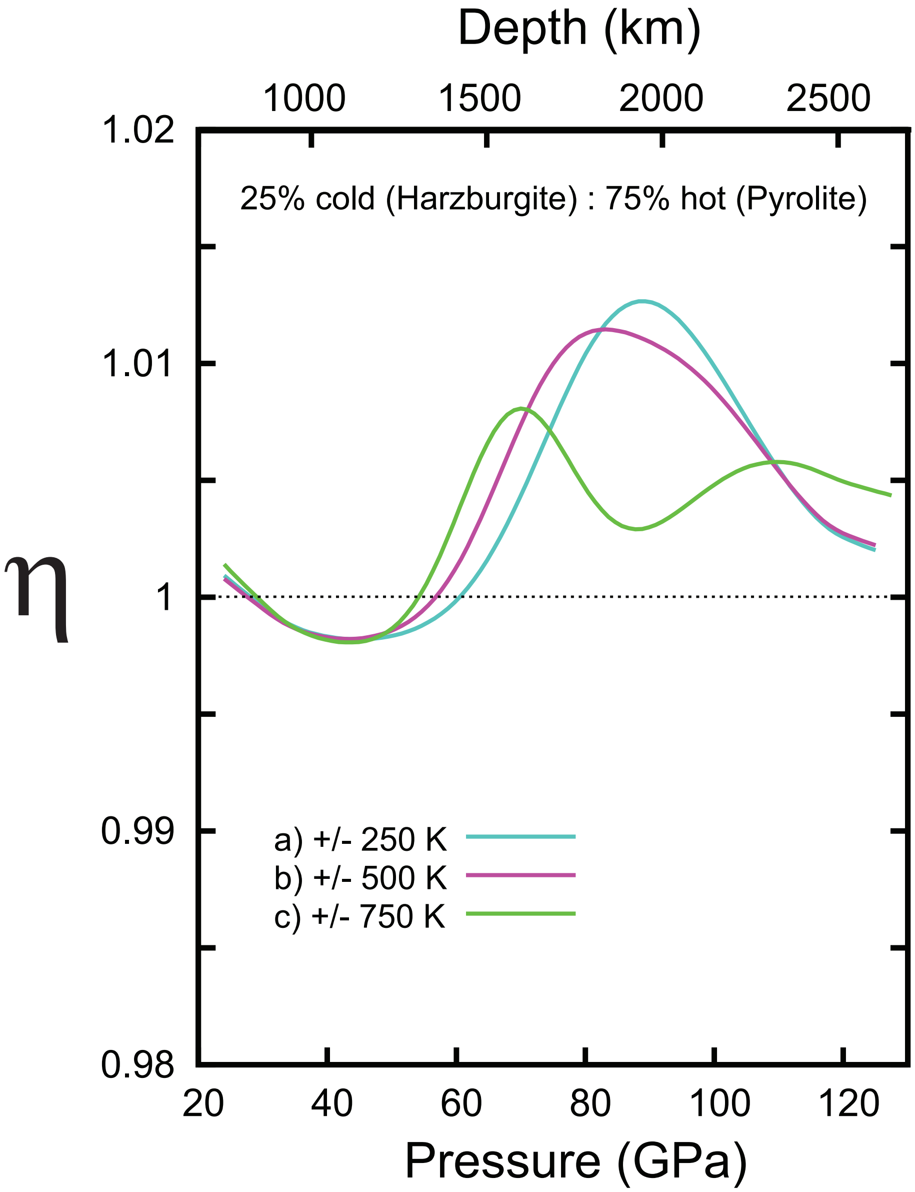

Figure 4.4: Lateral temperature and composition variations of a) ± 250 K, b) ± 500 K, and c) ± 750 K for a mantle being 25% cold(harzburgite): 75 % hot(pyrolite).

a temperature increment will impact η's sensitivity. Because of the potentially complex coupling of lateral temperature differences with compositional variations, further work on the effect of spin crossovers on η would likely benefit from an assessment within a three dimensional convective scheme, such as the formulation proposed in [66].

4.5 Conclusions

Apparent deviations from adiabaticity due to spin crossover, as recorded by the Bullen's parameter, increased in proportion to the aggregate's ferropericlase content. The magnitude of these perturbations is generally consistent with the magnitude of variations in η present in previous seismological and geodynamic inversions of η in the lower mantle. Our results provide a sense of how much of a perturbation in η, given the spin crossover and lateral temperature variations, might be expected in one dimensional seismic models, with the net result being of order 1-2%. Accurate characterization of η either globally or locally could provide constraints on both the lateral temperature distribution and the fp content at depth, although such determinations hinge critically on achieving sufficient seismic resolution to resolve spin transitions. Also, the perturbations found in η for different mantle temperature averages highlight the importance of doing vertical seismic velocity profiles with sufficient precision to allow η to be characterized on a regional basis. Our results provide a guide for possible a priori models of η in regionalized inversions of velocity as a function of depth: inversions without spin crossover induced perturbations in η implicitly assume that spin transitions are absent at depth, and hence that no ferropericlase is present in the deep mantle. Results from this chapter can also be found in [102].

Chapter 5

The post-perovskite phase tranistion: Phase equilibria and effects of Fe and Al substitutions

The major mineral phase of the Earth's lower mantle, (Al, Fe)-bearing bridgmanite, transitions to a seemingly layered structure known as post-perovskite, at Earth's deep lower mantle pressure and temperature conditions. Despite extensive investigations by experiments and *ab initio* calculations, there are still some important aspects of this transformation that need clarification. Here, we systematically address this question in (Al, Fe^{3+})-, (Fe^{2+})- and (Fe^{3+})-bearing bridgmanite using *ab initio* calculations. We particularly address the phase boundary dependence on the chemistry and acoustic velocity changes across this transformation. Since the topography of and seismic velocity jumps at the D" discontinuity depend on the local composition and temperature, our results allowed us to further constrain the nature of the D" region. While our results are consistent with previous seismic studies of the deep mantle, such seismic features varied distinctly depending on the bearing element, in contrast to temperature gradients due to adiabatic self-compression. This suggests that the high temperatures of the D" region might be due to other heat transport mechanism such as heat exchange with the outer core.

5.1 Introduction

The extraordinary complexity of the region $\sim$ 300 km above the core mantle boundary (CMB), otherwise known as the D" region, comes from its enigmatic compositional nature and thermal structure. This makes it a compelling subject matter of intensive research in the geophysical sciences. One of its most relevant features is its thermal boundary layer, partially responsible of driving the mantle convection, and also of great importance to understand the thermal evolution of the core and heat flux necessary to power the dynamo. Fluctuations of the thermal boundary layer directly affect the heat flux rate from the core [73]. Such fluctuations can be caused by phase transitions, which are usually determined from discontinuities, or triplications, in the seismic observables of one-dimensional seismic models. For the D" region, the discontinuities in the compressional and shear velocities were found to be $\sim$ 2.5% to 3% in over 40 different studies summarized in Wysession et al. [114]. The magnitude of such relative differences was also consistent with synthetic waveforms computed from geodynamic simulations [87]. For the latter, the geodynamic model that best correlated with seismic observations was that of a thermal slab interacting with a phase transition. However, no mineral physics evidence revealed a phase transition at the time, likely due to limitations in the instrumentation and required laboratory conditions. It was only until 2004 when it was found that the major mineral phase of the lower mantle, bridgmanite $MgSiO_3$ perovskite (Pv), transitions to a seemingly lamellar phase, named post-perovskite (PPv), at approximately 125 GPa and 2500 K [70, 74, 99]. Followed this, extensive experimental [5, 21, 40, 60, 72, 80, 81, 88, 93–95] and computational [2, 20, 46, 68, 75, 97, 108] studies were performed. Despite all these efforts, there are still important aspects of this transformation that need clarification, particularly on the effect of bearing elements such as Fe and Al. The presence or absence of these bearing elements directly affects how the transition occurs, i.e., the Clapeyron slope and the coexistence between phases. For instance, various studies have argued that Al_2O_3 tend to stabilize the Pv phase to higher pressures [2, 20, 93], while others, like Tsuchiya et al. [97], observed a moderate decrease of the transition pressure. Similar disparities were also found for ferrous iron Fe^{2+}: It has been proposed that Fe^{2+} should stabilize the PPv phase at lower pressures [20, 60, 75, 80], as opposed to findings in other studies [40, 94]. Furthermore, Catalli et al. [21] showed that the effect of ferric iron Fe^{3+} was to narrow the phase coexistence region, while (Fe^{3+}, Al^{3+}) had a similar Pv-PPv coexistence to that displayed by Fe^{2+}-bearing systems. However, both of these cases, Fe^{3+}- and (Fe^{3+}, Al^{3+})-, increased the transition pressure. We used *ab-initio* thermodynamic data to compute the phase boundaries and validate them by comparing with all the aforementioned cases. Also, we examined the phase boundaries of various lower mantle aggregates, in which the ferrous iron concentration in PPv is constrained by the amount of ferropericlase (fp) present in the deep mantle, i.e., the partitioning coefficient $K_D^{PPv/Fp}$. Experiments suggest that the PPv phase is likely to be iron depleted, with $K_D^{PPv/Fp}$ values of ~ 0.12 [5, 79, 88] and ~ 0.3 [56, 79]. This might be due to fp's higher affinity for iron [5]. Nevertheless, some studies suggest otherwise, e.g., $K_D^{PPv/Fp} \sim 0.6$ [8]. Here we study the effect of the Pv-PPv transition on various lower mantle aggregates with Mg/Si ratios ranging from 0.82 to 1.56 (Chondrite to harzburgite) and a fixed $K_D^{Pv/Fp}$ and $K_D^{PPv/Fp}$ of 0.5.

Evidence of seismic velocities decreasing at the bottom of the D" region have also been detected [96, 114]. This was interpreted by Hernlund et al. [36–38] as a "double-crossing" phenomena, where Pv transitions to PPv and back-transforms to the Pv phase. Indeed, this phenomena strongly depends on the geotherm: Cold temperatures tend to stabilize the PPv phase, steep temperature gradients enhance the chances of double-crossing, and very steep temperature gradients may even prevent the occurrence of the Pv-PPv transition [38]. This is another important aspect for addressing the temperature of the D" region. We approach this by analyzing the changes in the acoustic velocities along different geotherms, and by computing the temperature profiles of different types of bearing systems, in order to study the effect on the adiabatic temperature gradients across the phase transition.

5.2 Method and Calculation Details

The Pv and PPv thermoelastic properties of $Mg_{1-x}Fe_x^{2+}SiO_3$, $(Mg_{1-x}Al_x)(Si_{1-x}Al_x)O_3$, $(Mg_{1-x}Fe_x^{3+})(Si_{1-x}Al_x)O_3$, $(Mg_{1-x}Fe_x^{3+})(Si_{1-x}Fe_x^{3+})O_3$ ($x = 0$ and 0.125) are from [82, 84, 86]. For fp $Mg_{1-y}Fe_yO$ ($y = 0$ and 0.1875), thermoelastic properties were taken from [112]. Other x and y concentrations were computed by linear interpolation. We only considered spin crossover in fp, i.e., fp's iron is in a mixed spin (MS) state of high spin (HS) and low spin (LS) states. Pv and PPv bearing Fe^{2+} and (Fe^{3+},Al) are in HS state, while Fe^{3+} in LS state. Spin crossover in Fe^{3+} bearing Pv and PPv was not considered as it should not affect the phase boundary calculation, since this occurs at pressures lower than the Pv to PPv transition [43, 82, 83, 85]. The $CaSiO_3$ (CaPv) properties were reproduced from [52,53] using the Mie-Debye-Grüneisen formalism [90]. The lower mantle aggregates considered: Harzburgite [10], chondrite [33], pyrolite [67], peridotite [39], and perovskititic only [109], are mixtures of SiO_2 - MgO - CaO - FeO - Al_2O_3, with a uniform Fe-Mg partitioning coefficient $K_D^{Pv/Fp}$ and $K_D^{PPv/Fp} = \frac{x/(1-x-z)}{y/(1-y)}$ of 0.5. The temperature profiles of the minerals and rocks were computed from the from their adiabatic gradient

$$\left(\frac{\partial T}{\partial P}\right)_S = \frac{\alpha V T}{C_p} \tag{5.1}$$

We denote the molar fraction, molar volume, molar mass, thermal expansion coefficient, and isobaric specific heat of the i^{th} mineral in the mixture as μ_i, V_i, M_i, α_i, and Cp_i respectively. The aggregate properties such as volume, thermal expansion coefficient, and isobaric specific heat are then $V = \sum_i \mu_i V_i$, $\alpha = \sum_i \alpha_i \mu_i V_i / V$, and $C_p = \sum_i \mu_i C_{p_i}$. Aggregate moduli and velocities were computed using the Voigt-Reuss-Hill (VRH) averaging scheme.

The phase boundaries were calculated using the standard state model for binary systems (See chapter 2), where the Gibbs free energies $\mathscr{G}^{Pv/PPv}$ of a binary system with phases Pv and PPv and end-members 'A' and 'B' can be computed as

$$\mathscr{G}^{Pv}(T, P, x) = x(\mathscr{G}_B^{Pv} - \mathscr{G}_B^{PPv}) + k_B T(xln[x] + (1-x)ln[1-x]) \tag{5.2}$$

$$\mathscr{G}^{PPv}(T, P, x) = (1-x)(\mathscr{G}_A^{PPv} - \mathscr{G}_A^{Pv}) + k_B T(xln[x] + (1-x)ln[1-x]) \tag{5.3}$$

with k_B as the Boltzmann constant and x as bearing element concentration. End-member 'A' corresponds to $MgSiO_3$, while end-member 'B' is either: $Fe^{2+}SiO_3$, $Fe_2^{3+}O_3$, Al_2O_3, or $Fe^{3+}AlO_3$. The bearing element concentration of each phase, x_*^{Pv} and x_*^{PPv}, was computed as

$$x_*^{PPv} = \frac{1 - e^{\frac{\mathscr{G}_A^{PPv} - \mathscr{G}_A^{Pv}}{k_B T}}}{e^{\frac{\mathscr{G}_B^{PPv} - \mathscr{G}_B^{Pv}}{k_B T}} - e^{\frac{\mathscr{G}_A^{PPv} - \mathscr{G}_A^{Pv}}{k_B T}}} \qquad x_*^{Pv} = x^{PPv}\left(e^{\frac{\mathscr{G}_B^{PPv} - \mathscr{G}_B^{Pv}}{k_B T}}\right) \tag{5.4}$$

with (*) denoting: Fe^{2+}, Fe^{3+}, Al^{3+}, or (Fe^{3+}, Al^{3+}), depending on the end-member 'B'. Moreover, the PPv fraction (n_{PPv}) for a particular bearing element concentration x, was calculated using the lever rule

$$n_{PPv} = \frac{x - x_*^{Pv}}{x_*^{PPv} - x_*^{Pv}} \tag{5.5}$$

5.3 Results and Discussion

5.3.1 Effects of Fe and Al bearing elements on the Pv-PPv phase boundary

We studied the effects that bearing elements have on the Pv-PPv phase boundary. Figures 5.1a) to 5.1d) show the phase boundaries for all the bearing systems: $Mg_{1-x}Fe_x^{2+}SiO_3$, $(Mg_{1-x}Fe_x^{3+})(Si_{1-x}Fe_x^{3+})O_3$, $(Mg_{1-x}Al_x)(Si_{1-x}Al_x)O_3$, and $(Mg_{1-x}Fe_x^{3+})(Si_{1-x}Al_x)O_3$, with $x = 0.10$. Solid lines are the boundaries calculated from taking the arithmetic average of the leftmost and rightmost boundaries using LDA and GGA functionals (See Table 5.1). Hence, the gray shaded areas represent the uncertainties in our calculations, while the blue shaded areas are the regions where the Pv and PPv phases are likely to coexist. The hazel and pink temperature profiles correspond to that of Brown and Shankland [15] and Boehler [12], respectively. All cases seemed to be in good agreement with experiments: Despite that the Pv-PPv coexistence region for Fe^{2+}- predicted by Catalli et al. [21] is shifted to higher pressures compared to our calculation; the overall width of this region, including the uncertainties, is almost the same. Moreover, the phase boundaries of Fe^{3+}- and (Fe^{3+}, Al^{3+})- (Figures 5.1b) and 5.1d)) are in good agreement with Catalli et al. [21], while discrepancies between calculations and experiments in Figure 5.1c) are probably due to the high Al^{3+}- concentration (x=0.25) in Tateno et al. [93] experiments. Furthermore, a common feature among all these cases is that the coexistence between phases increased at lower temperatures, except for the Fe^{3+}- bearing case (Figure 5.1b).

The phase boundary and coexistence between the Pv and PPv phases is also expected to vary depending on the bearing element concentration [2, 5, 21, 93]. This is shown in Figure 5.2, for concentrations of x = 0.08, 0.10, and 0.12. In all cases, the coexistence region increased with concentration. However, with the exception of Fe^{2+}-, the transition pressure P_T always increased. In other words, Fe^{3+}-, Al^{3+}-, and (Fe^{3+}, Al^{3+})- tend to stabilize the Pv phase, while Fe^{2+} has the opposite effect. This can also be observed in Figure 5.4, which shows the phase boundaries for all the bearing cases, parametrized in terms of concentration vs. pressure, at different relevant lower mantle temperatures. Each temperature is represented by a different color, while its intensity indicates the locations of the Pv, Pv+PPv, and PPv phases. With increasing concentration, a noteworthy feature is the negative slopes of Fe^{2+}- bearing systems (Figures 5.4a1) to 5.4b4)), compared to the positive ones for the other cases. This observable upholds what was previously discussed: As the concentration of Fe^{3+}-, Al^{3+}-, and (Fe^{3+}, Al^{3+})- increases, the Pv phase tends to be stabilized, while higher concentrations of Fe^{2+}- stabilize the PPv phase. These trends are consistent with previous studies [2, 20, 21, 60, 75, 83, 93]. We also explored how the post-perovskite fraction n_{PPv} varies and what is the effect of the different functionals, LDA and GGA, on the phase boundary (See Figure 5.3). Compared to LDA, GGA displayed a thinner coexistence between phases shifted to higher pressures. However, in all cases, n_{PPv} shows a gradual change across the transition, and is particularly broader for boundaries computed with LDA thermodynamic data.

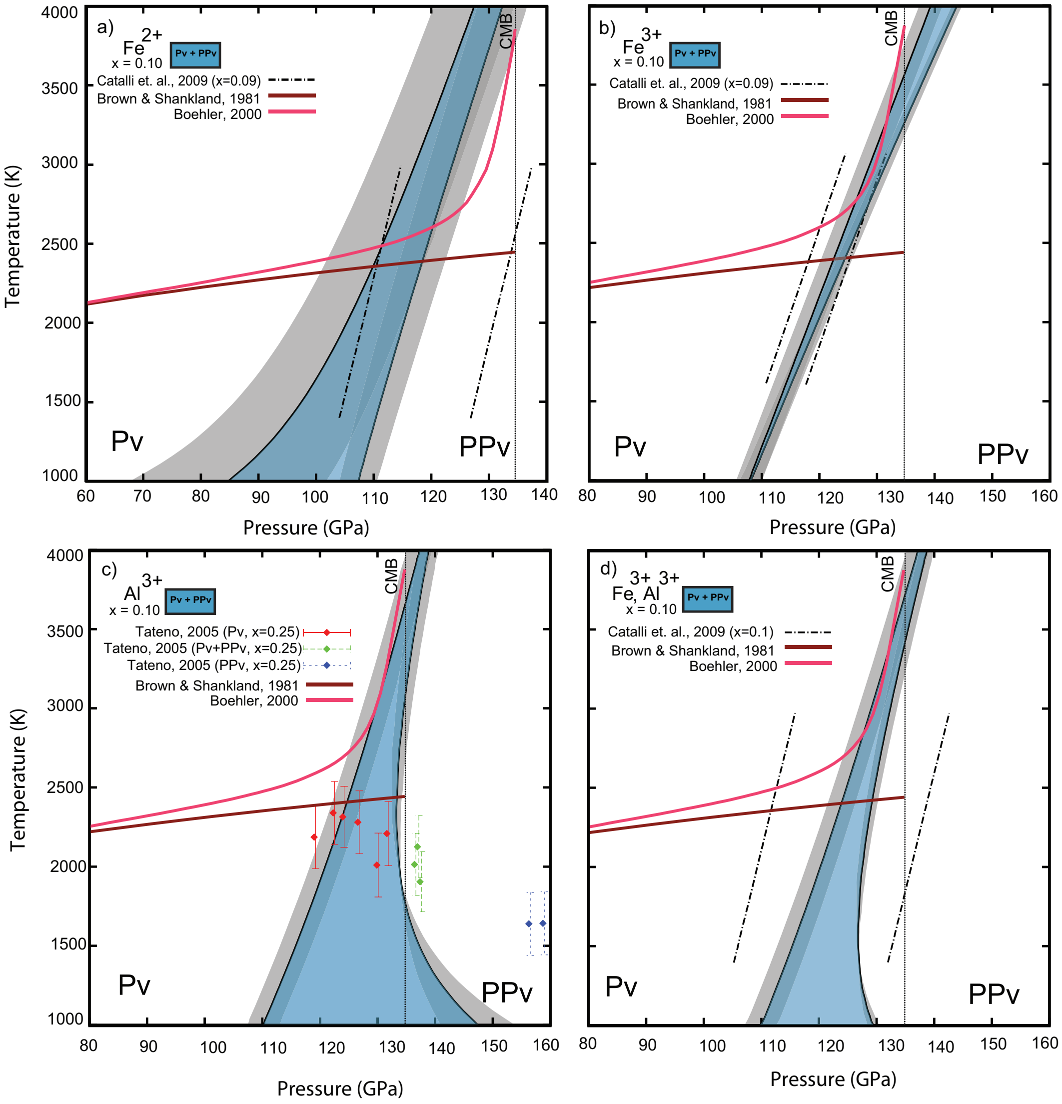

Figure 5.1: Figures a) to d) are the phase boundaries of $Mg_{1-x}Fe^{2+}_xSiO_3$, $(Mg_{1-x}Fe^{3+}_x)(Si_{1-x}Fe^{3+}_x)O_3$, $(Mg_{1-x}Al_x)(Si_{1-x}Al_x)O_3$, and $(Mg_{1-x}Fe^{3+}_x)(Si_{1-x}Al_x)O_3$, respectively, for a concentration x = 0.10. Solid black lines are the boundaries. Gray shaded areas are the uncertainties in the calculations. Blue shaded areas are the regions where the Pv and PPv phases are likely to coexist. Dashed lines and symbols are the experimental data from Catalli et al. [21] and Tateno et al. [93] respectively. Hazel/pink lines depict the geotherms by Brown and Shankland [15] and Boehler [12], respectively. The vertical dashed-dotted line indicates the location of the core mantle boundary (CMB).

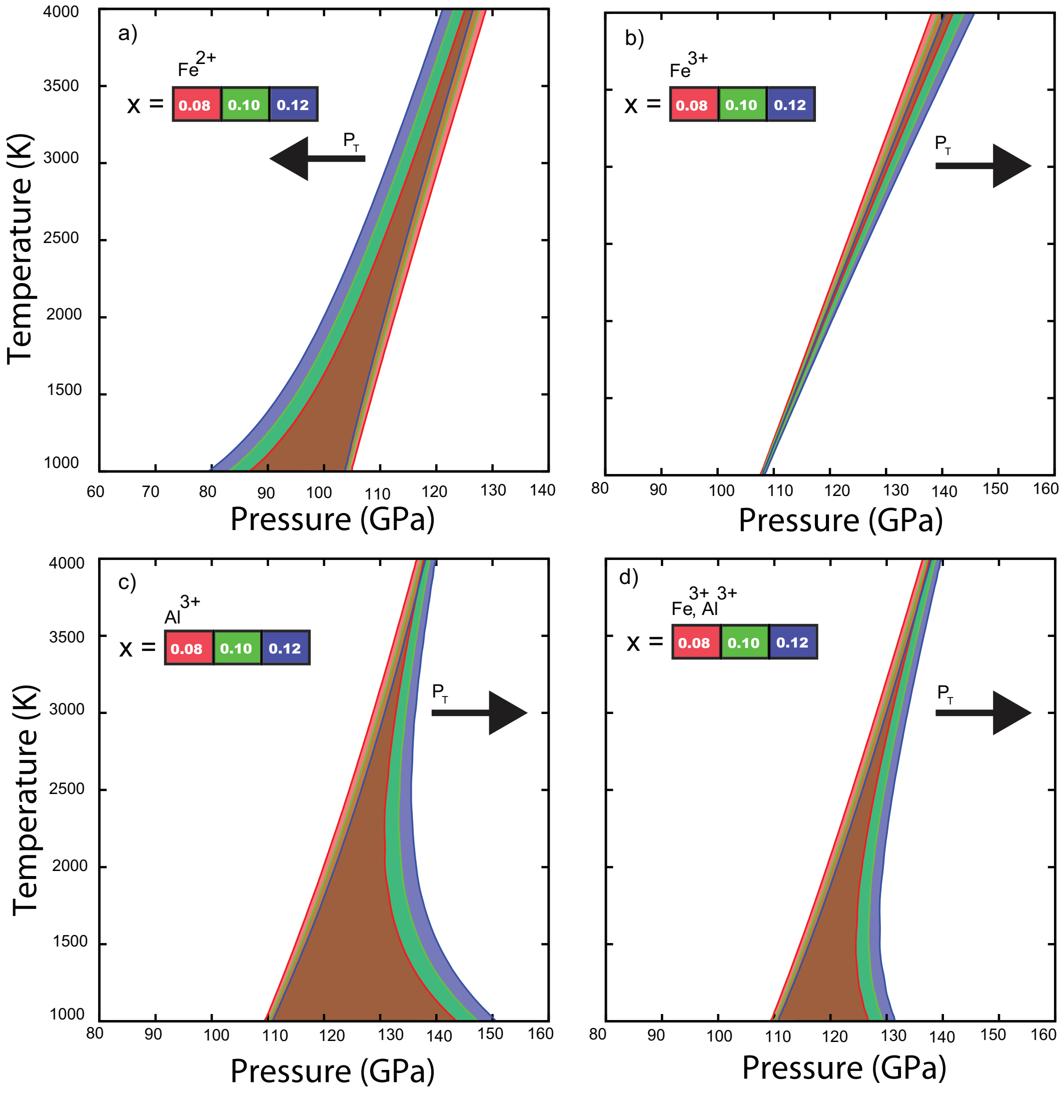

Figure 5.2: Phase boundaries for $Mg_{1-x}Fe^{2+}_xSiO_3$, $(Mg_{1-x}Fe^{3+}_x)(Si_{1-x}Fe^{3+}_x)O_3$, $(Mg_{1-x}Al_x)(Si_{1-x}Al_x)O_3$, and $(Mg_{1-x}Fe^{3+}_x)(Si_{1-x}Al_x)O_3$; with concentrations x of 0.08 (red), 0.10 (green), and 0.12 (blue). P_T stands for the transition pressure and the arrows indicates how it is changing with concentration.

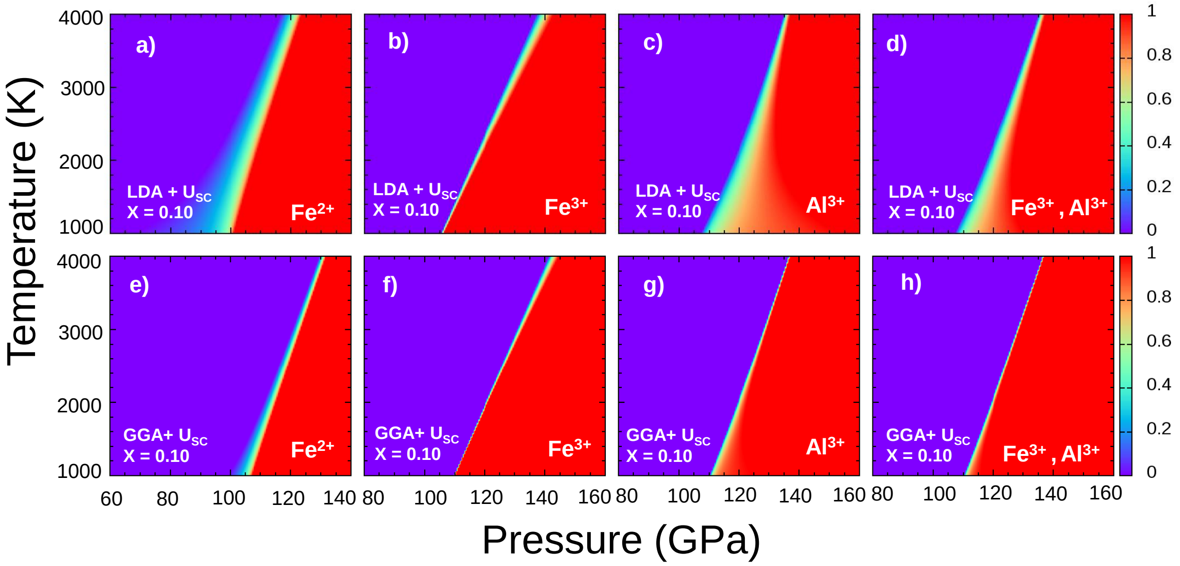

Figure 5.3: Surface plots showing the post-perovskite fraction for all the LDA (a to d) and GGA (e to h) bearing cases, with concentration x=0.10.

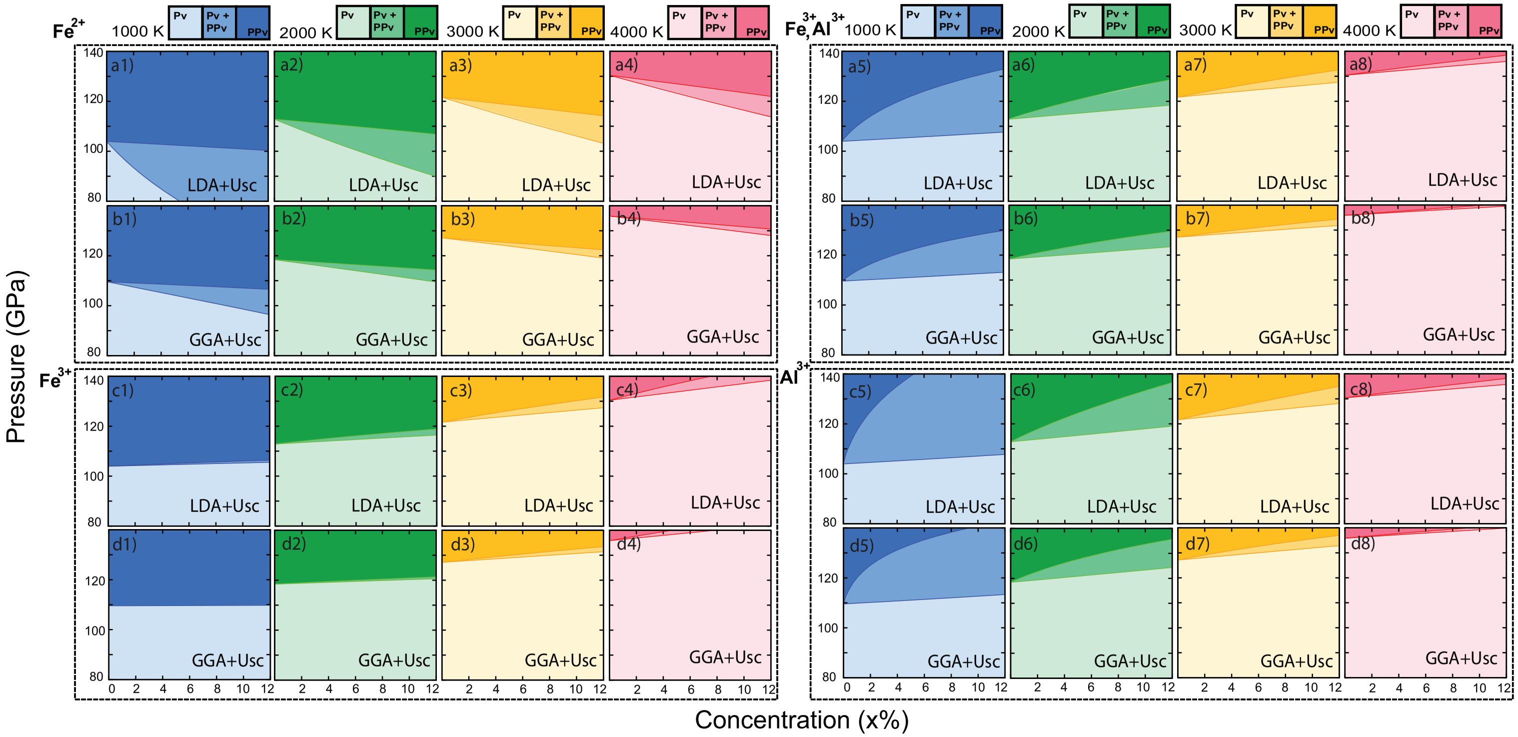

Figure 5.4: Pressure vs concentration (x%) boundaries at relevant lower mantle temperatures for $Mg_{1-x}Fe_x^{2+}SiO_3$, $(Mg_{1-x}Fe_x^{3+})(Si_{1-x}Fe_x^{3+})O_3$, $(Mg_{1-x}Al_x)(Si_{1-x}Al_x)O_3$, and $(Mg_{1-x}Fe_x^{3+})(Si_{1-x}Al_x)O_3$ with LDA and GGA functionals. The bearing element for each system is shown in the top left corner of each dashed rectangle. Colors indicate the temperature (1000 K to 4000 K) and its intensity the locations of the Pv, Pv+PPv, and PPv phases.

Table 5.1: Left (L) and right (R) LDA and GGA phase boundaries for $Mg_{1-x}Fe_x^{2+}SiO_3$, $(Mg_{1-x}Fe_x^{3+})(Si_{1-x}Fe_x^{3+})O_3$, $(Mg_{1-x}Al_x)(Si_{1-x}Al_x)O_3$, and $(Mg_{1-x}Fe_x^{3+})(Si_{1-x}Al_x)O_3$ with x = 0.10.

Temperature (K)	$Mg_{1-x}Fe_x^{2+}SiO_3$ [LDA(L), LDA(R), GGA(L), GGA(R)]	$(Mg_{1-x}Fe_x^{3+})(Si_{1-x}Fe_x^{3+})O_3$ [LDA(L), LDA(R), GGA(L), GGA(R)]	$(Mg_{1-x}Al_x)(Si_{1-x}Al_x)O_3$ [LDA(L), LDA(R), GGA(L), GGA(R)]	$(Mg_{1-x}Fe_x^{3+})(Si_{1-x}Al_x)O_3$ [LDA(L), LDA(R), GGA(L), GGA(R)]
1000	[67.000, 101.00, 99.00, 107.50]	[105.50, 106.50, 110.00, 110.00]	[107.50, 154.00, 113.00, 141.00]	[107.00, 130.50, 113.00, 128.00]
1200	[75.500, 102.50, 102.00, 109.00]	[107.50, 108.50, 112.00, 112.00]	[109.50, 146.50, 115.00, 138.00]	[109.50, 128.00, 115.00, 127.00]
1400	[81.500, 104.00, 105.00, 110.50]	[110.00, 111.00, 114.00, 114.50]	[112.00, 141.00, 117.50, 136.00]	[111.50, 127.00, 117.00, 127.00]
1600	[86.500, 105.00, 107.00, 112.00]	[112.00, 113.50, 116.50, 116.50]	[114.00, 137.50, 119.50, 135.00]	[114.00, 126.50, 119.00, 127.00]
1800	[90.000, 106.50, 109.00, 113.50]	[114.00, 116.00, 118.50, 119.00]	[116.50, 135.00, 121.50, 134.00]	[116.00, 126.50, 121.00, 127.50]
2000	[93.500, 108.00, 111.50, 115.00]	[116.00, 118.00, 120.50, 121.00]	[118.50, 133.50, 123.50, 134.00]	[117.50, 127.00, 123.00, 128.50]
2200	[96.500, 109.50, 113.00, 117.00]	[118.00, 120.50, 122.50, 123.50]	[120.00, 133.00, 125.50, 134.00]	[119.50, 127.50, 124.50, 129.00]
2400	[99.000, 111.00, 115.00, 118.50]	[120.50, 123.00, 124.50, 125.50]	[122.00, 132.50, 127.00, 134.00]	[121.50, 128.00, 126.50, 130.00]
2600	[101.50, 112.50, 117.00, 120.00]	[122.50, 125.50, 127.00, 128.00]	[124.00, 132.50, 129.00, 134.50]	[123.50, 129.00, 128.00, 131.00]
2800	[104.00, 114.00, 119.00, 122.00]	[124.50, 128.00, 129.00, 130.50]	[125.50, 132.50, 130.50, 135.00]	[125.00, 130.00, 129.50, 132.50]
3000	[106.50, 115.50, 120.50, 123.50]	[126.50, 130.50, 131.00, 132.50]	[127.50, 133.00, 132.00, 136.00]	[127.00, 131.00, 131.50, 133.50]
3000	[106.50, 115.50, 120.50, 123.50]	[126.50, 130.50, 131.00, 132.50]	[127.50, 133.00, 132.00, 136.00]	[127.00, 131.00, 131.50, 133.50]
3200	[108.50, 117.50, 122.50, 125.00]	[129.00, 133.00, 133.00, 135.00]	[129.00, 134.00, 133.50, 136.50]	[128.50, 132.50, 133.00, 135.00]
3400	[110.50, 119.00, 124.50, 127.00]	[131.00, 135.50, 135.00, 137.50]	[130.50, 134.50, 135.00, 137.50]	[130.50, 133.50, 134.50, 136.00]
3600	[112.50, 120.50, 126.00, 128.50]	[133.00, 138.00, 137.00, 140.00]	[132.00, 135.50, 136.50, 138.50]	[132.00, 135.00, 136.00, 137.50]
3800	[114.50, 122.00, 128.00, 130.00]	[135.00, 140.50, 139.50, 142.50]	[133.50, 136.00, 138.00, 139.50]	[133.50, 136.00, 137.50, 138.50]
4000	[116.50, 123.50, 129.50, 132.00]	[137.50, 143.00, 141.50, 145.00]	[135.00, 137.00, 139.50, 140.50]	[135.00, 137.50, 139.00, 140.00]

5.3.2 Changes across the phase transition

The magnitude of the changes of the seismic observables, namely: Compressional V_P, bulk V_ϕ, shear V_S velocities, and density ρ; across the phase transition, depends on the boundary thickness and temperature profile. Figure 5.5 shows the percentages of those variations as a function of pressure, along a typical geotherm [15], for different bearing elements. The different seismic changes are shown in each column and were computed as $\Delta M(\%) = 100 * (M_{agg} - M_{PV})/M_{PV}$, where M is either V_P,V_ϕ, V_S, or ρ; and M_{agg} is the Pv and PPv aggregate. The last column shows n_{PPv} values along Brown and Shankland geotherm [15]. Each color depicts the changes for a different bearing element. Shaded areas are the differences between the changes across LDA and GGA boundaries. All these cases correspond to a concentration of x = 0.10. Overall, changes in seismic observables are within the magnitude of previous seismic studies [87,114]. All changes were positive with the exception of $\Delta V_\phi(\%)$, which shows values of $\Delta V_\phi(\%) \sim$ -0.8% in most of the cases (Figures 5.5b), 5.5g), and 5.5q) with the exception of Al^{3+}- (Figure 5.5g), with $\Delta V_\phi(\%) \sim$ -2.5%. These negative contrasts are due to a decrement of the adiabatic bulk modulus (K_S) across the transition, in accordance with previous studies [114].

Changes in shear velocity were larger, with the highest contrast value of $\Delta V_S(\%) \sim$ 3.7% for the Fe^{3+}- case (Figure 5.5h). All other $\Delta V_S(\%)$ contrasts were within $\sim$ 2% to $\sim$ 2.4%. This is of course due to an increment of the shear modulus (G), which is consistent with seismic observations of the deep mantle [87]. The changes in the

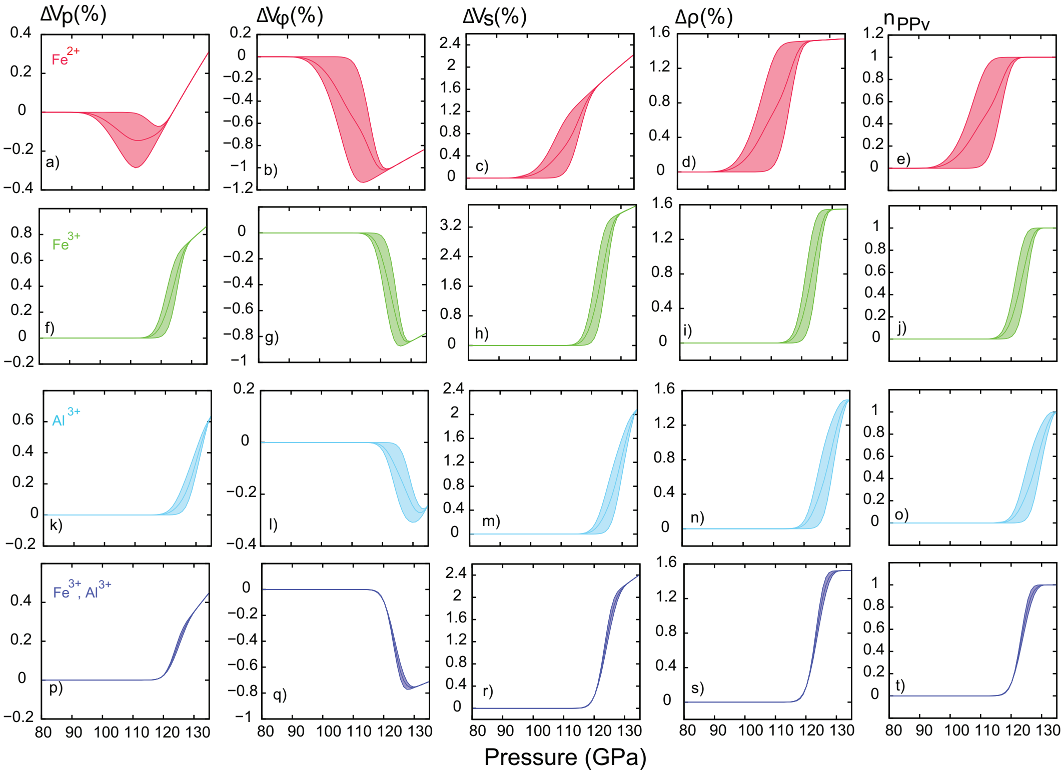

Figure 5.5: Calculated contrasts $\Delta V_P(\%)$, $\Delta V_\phi(\%)$, $\Delta V_S(\%)$, $\Delta\rho(\%)$ and PPv fraction (n_{PPv}) in $Mg_{1-x}Fe_x^{2+}SiO_3$, $(Mg_{1-x}Fe_x^{3+})(Si_{1-x}Fe_x^{3+})O_3$, $(Mg_{1-x}Al_x)(Si_{1-x}Al_x)O_3$, and $(Mg_{1-x}Fe_x^{3+})(Si_{1-x}Al_x)O_3$, respectively, with x=0.10. The contrasts are calculated along the Brown and Shankland temperature profile [15] as: $\Delta M = 100 * (M_{agg} - M_{PV})/M_{PV}$, with M as: V_P, V_ϕ, V_S, and ρ.

compressional velocities $\Delta V_P(\%)$ were positive in all cases, with values varying between $\sim 0.3\%$ to $\sim 0.9\%$. However, $\Delta V_P(\%)$ for Fe^{2+} (Figure 5.5a) decreased from 95 GPa to 110 GPa. This distinct feature is due to a ‘competition’ between K_S and G, where G dominates the overall behavior for the aforementioned pressure range. Additionally, with a value of $\Delta\rho(\%) \sim 1.6\%$, density contrasts are nearly identical for all cases. This observation is quite consistent with density discontinuities reported for the D” region [87, 114]. Positive and negative ‘jumps’, otherwise known as paired discontinuities, have also been reported [96, 114]. This phenomena depends strongly on the temperature gradient and corresponds to a Pv-PPv-Pv transition, known as double-crossing [37, 38]. We computed the contrasts along a superadiabatic temperature gradient [12] (See appendix - Figure A.11). In this case, the PPv phase is not always stable, and thus, double-crossing occurs.

5.3.3 Effects on the adiabatic temperature gradient

The origin and intensity of the thermal boundary layer that sits atop of the core mantle boundary (CMB) are still debatable. With reported temperatures above 4000 K, some of the most common reasons attributed to such extreme conditions are: Heat exchange with the outer core, radiation, or heat released from the Pv-PPv exothermic phase transition. To test the latter, we calculated the adiabatic temperature profiles of all the various types of bearing Pv and PPv phases, across the transition, and examined the effect on the temperature gradient (See Figure 5.6). All the adiabats followed a similar temperature profile, with CMB temperatures only about 80 K hotter than Brown and Shankland geotherm [15], but 2500 K cooler than Boehler geotherm [12]. Moreover, none of the adiabats exhibited significant changes across the Pv-PPv transition, as can be seen from the inset in Figure 5.6. This might suggest that, regardless of the bearing element, the high temperatures believed to be found in the D” thermal boundary layer are likely due to other transport mechanisms, e.g., heat exchange with the outer core. We did not consider spin-crossover for the Fe^{3+}- case. The effect of spin-crossover on the lower mantle adiabat was already meticulously addressed in chapter 3 (See also [101]).

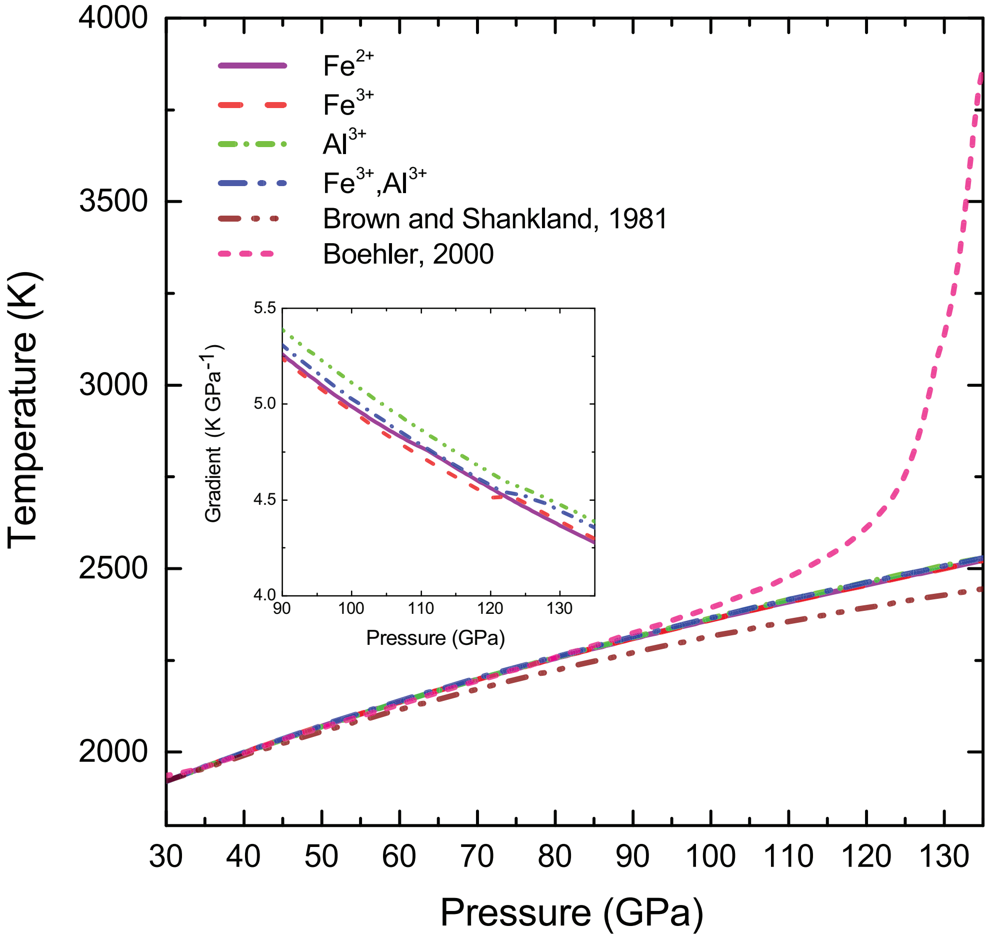

Figure 5.6: Adiabats of $Mg_{1-x}Fe_x^{2+}SiO_3$, $(Mg_{1-x}Fe_x^{3+})(Si_{1-x}Fe_x^{3+})O_3$, $(Mg_{1-x}Al_x)(Si_{1-x}Al_x)O_3$, and $(Mg_{1-x}Fe_x^{3+})(Si_{1-x}Al_x)O_3$, respectively, with x=0.10. The hazel/pink profiles corresponds to that of Brown and Shankland [15]/ Boehler [12]. The inset shows the temperature gradients across the transition.

5.3.4 Effects on Mantle Aggregates

The boundaries of (Fe^{2+}, Al^{3+})-$MgSiO_3$ Pv-PPv phase transition, in different lower mantle aggregates, are shown in Figure 5.7a). Uncertainties for each aggregate boundary are shown in the appendix (See Figure A.9). The molar concentration of each mineral is shown in the pie charts. The corresponding x, y, and z values are shown in the colored boxes. As the Mg/Si ratio increases so does the amount of fp in the aggregate, and consequently, the Fe^{2+} concentration x in Pv and PPv diminishes. The latter also causes a decrement of the Pv-PPv coexistence width. This observation seems to be consistent as long as the Al^{3+} concentration y doesn't vary dramatically: There is a notable change in the coexistence width between peridotite and harzburgite. While the lower Fe^{2+} concentration of harzburgite compared to peridotite partially explains this phenomenon, the main reason seems to be the difference in Al^{3+}. This suggests that Al^{3+} induces a sharper change in the coexistence between phases, compared to Fe^{2+}. This behavior seems to be consistent with experiments [21], and might also explain why pyrolite's boundary is wider than chondrite's: Pyrolite has less Fe^{2+}, but more Al^{3+} than chondrite. This is also consistent with Andrault et al. [5], where it was found that fp should reduce the Pv to PPv coexistence width in Al-bearing systems. Furthermore, none of the geotherms used [12, 15] is hot or steep enough to induce double-crossing, i.e., the PPv phase is likely to be stable for all aggregates studied at CMB pressures.

Figure 5.7b) shows the different aggregate velocities and densities, along Brown and Shankland geotherm [15], compared to the preliminary reference Earth model PREM [29]. Deviations from PREM throughout mid lower mantle pressures are due to iron spin-crossover in fp. The latter has been previously discussed in chapter 3 (See also [101]) for the aggregates of interest in this study. Changes due Pv-PPv transition on the velocities and densities can be observed from $\sim$ 107 GPa onwards. This is coherent with the geotherm-boundary intersection shown in Figure 5.7 a). The changes due to this transition can be clearly observed in V_ϕ, V_S, and ρ, while in V_P are more subtle. Regardless of the phase boundary and aggregate composition, densities and V_S showed an overall agreement with PREM. However, the phase transition induced deviations from PREM in V_S at high pressures.

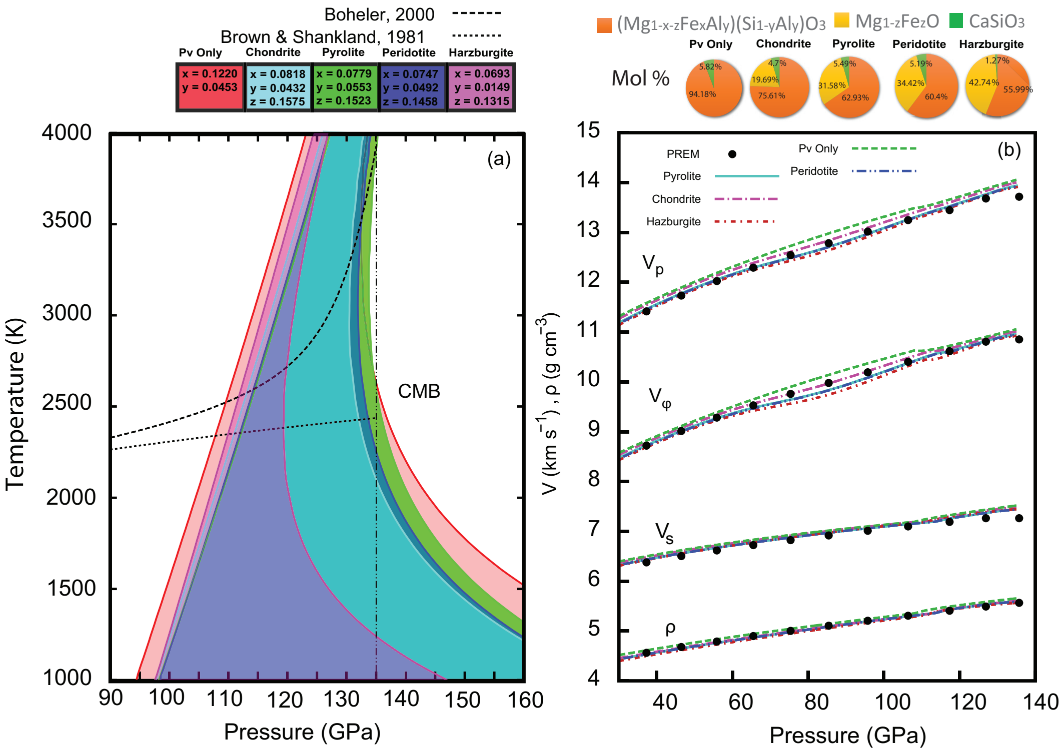

Figure 5.7: a) Pv-PPv phase boundary for different lower mantle aggregates. The Fe^{2+} and Al concentrations in Pv and PPv are given by x and y, while z is the Fe^{2+} concentration in fp. The dotted lines correspond to Boehler [12] and Brown & Shankland [15] geotherms. The vertical dashed-dotted line delineates the core mantle boundary (CMB). Pie-charts show the mol percentage of each mineral in the aggregate. (b) Velocities and densities for lower mantle aggregates, along the Brown & Shankland geotherm [15], compared with dots representing the preliminary Earth reference model (PREM) [29].

5.4 Geophysical Significance

We presented a comprehensive study of the effect of Fe and Al bearing elements on the Pv-PPv phase transition, and its consequences on seismic observables and temperature gradients, in an attempt to further constrain the uncertainties in the temperature and composition of the D" region. Despite the fact that it is still an open question whereas the Pv-PPv phase transition alone can explain all the seismic features of the deep mantle [2], it is believed that the exothermic nature of this phase transition should destabilize the thermal boundary layer, and thus, favor the heat flow between core and mantle, leading to an increment of the temperature gradient and the amount of small-scale plumes in the D" region [73]. Our results suggest that under the assumption of adiabatic self-compression, and regardless of the bearing element hosted in Pv or PPv, there are no indications of a steep temperature gradient across the phase transition. Nevertheless, this could also suggest that the existence of a thermal boundary layer is likely due to heat exchange with the outer core.

We also determined that higher concentrations of Fe^{2+} tend to decrease the transition pressure. Hence, low pressure discontinuities in seismic observables might indicate a greater presence of Fe^{2+} in the mantle. The magnitudes of these discontinuities were found to be comparable to those from seismic studies [87,114]. Another distinct feature we observed were the large velocity changes, $\Delta V_P \sim 0.9\%$ and $\Delta V_S \sim 3.7\%$, displayed by Fe^{3+} bearing systems, which if observed, could evince a higher concentration of Fe^{3+} in the deep mantle.

Furthermore, another relevant aspect we considered is the phase coexistence width and what it can indicate as an observable. Width variations might induce important geophysical consequences: The dominant effect of Al^{3+} over Fe^{2+}, observed in the width variation of the phase coexistence region in different mantle aggregates, suggests that broad seismic discontinuities indicate higher Al^{3+} concentrations. Furthermore, we also noticed a reduction of the coexistence region as the aggregate's Mg/Si ratio increased, which in other words imply that greater amounts of fp could be correlated with sharper seismic discontinuities in Al depleted systems.

5.5 Conclusions

The effects of Fe and Al on the Pv-PPv phase boundary and its consequences on the thermal structure and seismic observables were studied. Overall, the phase boundaries and seismic discontinuities were in agreement with mineral physics experiments and seismic studies. We found that shallow discontinuities might suggest a higher presence of Fe^{2+}, while sharp and large velocity contrasts are likely to correspond to greater Fe^{3+} concentrations. For mantle aggregates, broad phase coexistence regions and seismic discontinuities varied in proportion to the amount of Fe^{2+} and Al^{3+} in Pv and PPv. Small alterations in Al^{3+} affected significantly the phase boundary. Furthermore, results indicated that sharp discontinuities can be linked to high Mg/Si aggregate ratio, and consequently, to larger Fp concentrations. Finally, adiabatic temperature gradients across the transition did not display significant changes across the transition, suggesting that the high temperatures of D" thermal boundary layer might be due to other heat transport mechanism such as heat exchange with the outer core.

Chapter 6

Conclusions

Different aspects of the thermal structure and composition of the lower mantle were discussed in this work. The lower mantle thermal structure was shown to be affected by spin-crossovers in Fe-bearing minerals. Such phenomena lead to increments on the temperature gradients of various lower mantle aggregates. We also found that using a self-consistent temperature gradient, when comparing with one-dimensional seismic models, should sharpen uncertainties in studies of the lower mantle composition. Moreover, the novel use of a common seismic observable, known as the Bullen's parameter η, helped us to determine the signatures that spin-crossovers might display in studies of a lower mantle that is compositionally heterogeneous and varying its temperature laterally. The deviations from adiabaticity measured by η might serve as bridge between mineral physics and seismic observations, and also as a guide for the construction of *a priori* models of η in regionalized inversions of velocities with respect to depth; i.e., seismic inversions that ignore spin crossover perturbations in η essentially assume that ferropericlase is absent in the lower mantle. Finally, we showed a comprehensive study of the effects of Al and Fe substitutions on the Pv to PPv phase transition. Our results are in overall agreement with the discontinuities observed in seismic studies. Shallow/deeper discontinuities suggest a higher presence of Fe^{2+}/(Fe^{3+} and/or Al^{3+}). The temperature gradient calculated across the phase transition did not vary significantly, suggesting that the high temperatures of the D" thermal boundary layer are likely due to other heat transport mechanisms such as heat exchange with the outer core. Future work that would be beneficial to further develop the results shown here would be to consider a pressure or depth dependent Fe-partitioning coefficient and also to study the effects of spin crossovers on the Bullen's parameter within a three dimensional convective scheme. All the results presented in this work are a step forward in understanding the nature of the deep mantle.

References

[1] Akaogi, M., and Akimoto, S. High-pressure phase equilibria in a garnet lherzolite, with special reference to Mg^{2+}-Fe^{2+} partitioning among constituent minerals. *Physics of the Earth and Planetary Interiors 19*, 1 (1979), 31–51.

[2] Akber-Knutson, S., Steinle-Neumann, G., and Asimow, P. D. Effect of Al on the sharpness of the $MgSiO_3$ perovskite to post-perovskite phase transition. *Geophysical Research Letters 32*, 14 (2005).

[3] American, S. How do scientists determine the composition of the interior of Earth and other planets?, 2005.

[4] Anderson, O. The Earth's core and the phase diagram of iron. *Philosophical Transactions of the Royal Society of London A: Mathematical, Physical and Engineering Sciences 306*, 1492 (1982), 21–35.

[5] Andrault, D., Muñoz, M., Bolfan-Casanova, N., Guignot, N., Perrillat, J.-P., Aquilanti, G., and Pascarelli, S. Experimental evidence for perovskite and post-perovskite coexistence throughout the whole D" region. *Earth and Planetary Science Letters 293*, 1 (2010), 90–96.

[6] Antonangeli, D., Siebert, J., Aracne, C. M., Farber, D. L., Bosak, A., Hoesch, M., Krisch, M., Ryerson, F. J., Fiquet, G., and Badro, J. Spin crossover in ferropericlase at high pressure: A seismologically transparent transition? *Science 331*, 6013 (2011), 64–67.

[7] Anzellini, S., Dewaele, A., Mezouar, M., Loubeyre, P., and Morard, G. Melting of iron at Earth's inner core boundary based on fast x-ray diffraction. *Science 340*, 6131 (2013), 464–466.

[8] Auzende, A.-L., Badro, J., Ryerson, F. J., Weber, P. K., Fallon, S. J., Addad, A., Siebert, J., and Fiquet, G. Element partitioning between magnesium silicate perovskite and ferropericlase: New insights into bulk lower-mantle geochemistry. *Earth and Planetary Science Letters 269*, 1 (2008), 164–174.

[9] Badro, J., Fiquet, G., Guyot, F., Rueff, J.-P., Struzhkin, V. V., Vankó, G., and Monaco, G. Iron partitioning in Earth's mantle: toward a deep lower mantle discontinuity. *Science 300*, 5620 (2003), 789–791.

[10] Baker, M. B., and Beckett, J. R. The origin of abyssal peridotites: A reinterpretation of constraints based on primary bulk compositions. *Earth and Planetary Science Letters 171*, 1 (1999), 49–61.

[11] Bengtson, A., Li, J., and Morgan, D. Mössbauer modeling to interpret the spin state of iron in (Mg, Fe)SiO_3 perovskite. *Geophysical Research Letters 36*, 15 (2009).

[12] Boehler. High-pressure experiments and the phase diagram of lower mantle and core materials. *Reviews of Geophysics 38*, 2 (2000), 221–245.

[13] Bower, D. J., Gurnis, M., Jackson, J. M., and Sturhahn, W. Enhanced convection and fast plumes in the lower mantle induced by the spin transition in ferropericlase. *Geophysical Research Letters 36*, 10 (2009).

[14] Brillouin, L. *Wave propagation in periodic structures: Electric filters and crystal lattices.* Courier Corporation, 2003.

[15] Brown, J., and Shankland, T. Thermodynamic parameters in the Earth as determined from seismic profiles. *Geophysical Journal International 66*, 3 (1981), 579–596.

[16] Budiansky, B., Sumner, E. E., and O'Connell, R. J. Bulk thermoelastic attenuation of composite materials. *Journal of Geophysical Research: Solid Earth 88*, B12 (1983), 10343–10348.

[17] Bullen, K. Compressibility-pressure hypothesis and the Earth's interior. *Geophysical Supplements to the Monthly Notices of the Royal Astronomical Society 5*, 9 (1949), 335–368.

[18] Bullen, K. An index of degree of chemical inhomogeneity in the Earth. *Geophysical Journal International 7*, 5 (1963), 584–592.

[19] Bunge, H.-P., Ricard, Y., and Matas, J. Non-adiabaticity in mantle convection. *Geophysical research letters 28*, 5 (2001), 879–882.

[20] Caracas, R., and Cohen, R. Effect of chemistry on the stability and elasticity of the perovskite and post-perovskite phases in the $MgSiO_3$-$FeSiO_3$-Al_2O_3 system and implications for the lowermost mantle. *Geophysical Research Letters 32*, 16 (2005).

[21] Catalli, K., Shim, S.-H., and Prakapenka, V. Thickness and clapeyron slope of the post-perovskite boundary. *Nature 462*, 7274 (2009), 782–785.

[22] Catalli, K., Shim, S.-H., Prakapenka, V. B., Zhao, J., Sturhahn, W., Chow, P., Xiao, Y., Liu, H., Cynn, H., and Evans, W. J. Spin state of ferric iron in $MgSiO_3$ perovskite and its effect on elastic properties. *Earth and Planetary Science Letters 289*, 1 (2010), 68–75.

[23] Chudinovskikh, L., and Boehler, R. High-pressure polymorphs of olivine and the 660-km seismic discontinuity. *Nature 411*, 6837 (2001), 574–577.

[24] Crowhurst, J., Brown, J., Goncharov, A., and Jacobsen, S. Elasticity of (Mg, Fe)O through the spin transition of iron in the lower mantle. *Science 319*, 5862 (2008), 451–453.

[25] da Silva, C. R., Wentzcovitch, R., Patel, A., Price, G., and Karato, S. The composition and geotherm of the lower mantle: Constraints from the

elasticity of silicate perovskite. *Physics of the Earth and Planetary Interiors 118*, 1 (2000), 103–109.

[26] De Wit, R., and Trampert, J. Robust constraints on average radial lower mantle anisotropy and consequences for composition and texture. *Earth and Planetary Science Letters 429* (2015), 101–109.

[27] Deschamps, F., and Trampert, J. Towards a lower mantle reference temperature and composition. *Earth and Planetary Science Letters 222*, 1 (2004), 161–175.

[28] Dziewonski, A., Hales, A., and Lapwood, E. Parametrically simple Earth models consistent with geophysical data. *Physics of the Earth and Planetary Interiors 10*, 1 (1975), 12–48.

[29] Dziewonski, A. M., and Anderson, D. L. Preliminary reference Earth model. *Physics of the earth and planetary interiors 25*, 4 (1981), 297–356.

[30] Fukui, H., Yoneda, A., Nakatsuka, A., Tsujino, N., Kamada, S., Ohtani, E., Shatskiy, A., Hirao, N., Tsutsui, S., Uchiyama, H., et al. Effect of cation substitution on bridgmanite elasticity: A key to interpret seismic anomalies in the lower mantle. *Scientific Reports 6* (2016).

[31] Garnero, E. J., and McNamara, A. K. Structure and dynamics of Earth's lower mantle. *science 320*, 5876 (2008), 626–628.

[32] Gaskell, D. R. *Introduction to the Thermodynamics of Materials*. CRC Press, 2008.

[33] Hart, S. R., and Zindler, A. In search of a bulk-Earth composition. *Chemical Geology 57*, 3-4 (1986), 247–267.

[34] Heinz, D., Jeanloz, R., and O'Connell, R. J. Bulk attenuation in a polycrystalline Earth. *Journal of Geophysical Research: Solid Earth 87*, B9 (1982), 7772–7778.

[35] Heinz, D. L., and Jeanloz, R. Inhomogeneity parameter of a homogeneous Earth. *Nature 301*, 5896 (1983), 138–139.

[36] Hernlund, J., and Labrosse, S. Geophysically consistent values of the perovskite to post-perovskite transition Clapeyron slope. *Geophysical Research Letters 34*, 5 (2007).

[37] Hernlund, J. W. On the interaction of the geotherm with a post-perovskite phase transition in the deep mantle. *Physics of the Earth and Planetary Interiors 180*, 3 (2010), 222–234.

[38] Hernlund, J. W., Thomas, C., and Tackley, P. J. A doubling of the post-perovskite phase boundary and structure of the Earth's lowermost mantle. *Nature 434*, 7035 (2005), 882–886.

[39] Hirose, K., and Kushiro, I. Partial melting of dry peridotites at high pressures: Determination of compositions of melts segregated from peridotite using aggregates of diamond. *Earth and Planetary Science Letters 114*, 4 (1993), 477–489.

[40] Hirose, K., Takafuji, N., Fujino, K., Shieh, S. R., and Duffy, T. S. Iron partitioning between perovskite and post-perovskite: A transmission electron microscope study. *American Mineralogist 93*, 10 (2008), 1678–1681.

[41] Houser, C., and Williams, Q. The relative wavelengths of fast and slow velocity anomalies in the lower mantle: Contrary to the expectations of dynamics? *Physics of the Earth and Planetary Interiors 176*, 3 (2009), 187–197.

[42] Hsu, H., Blaha, P., Cococcioni, M., and Wentzcovitch, R. M. Spin-state crossover and hyperfine interactions of ferric iron in $MgSiO_3$ perovskite. *Physical Review Letters 106*, 11 (2011), 118501.

[43] Hsu, H., Umemoto, K., Blaha, P., and Wentzcovitch, R. M. Spin states and hyperfine interactions of iron in $MgSiO_3$ perovskite under pressure. *Earth and Planetary Science Letters 294*, 1 (2010), 19–26.

[44] Hsu, H., and Wentzcovitch, R. M. First-principles study of intermediate-spin ferrous iron in the Earth's lower mantle. *Physical Review B 90*, 19 (2014), 195205.

[45] Hsu, H., Yonggang, G. Y., and Wentzcovitch, R. M. Spin crossover of iron in aluminous $MgSiO_3$ perovskite and post-perovskite. *Earth and Planetary Science Letters 359* (2012), 34–39.

[46] Iitaka, T., Hirose, K., Kawamura, K., and Murakami, M. The elasticity of the $MgSiO_3$ post-perovskite phase in the earth's lowermost mantle. *Nature 430*, 6998 (2004), 442–445.

[47] Irifune, T. Absence of an aluminous phase in the upper part of the Earth's lower mantle. *Nature 370*, 6485 (1994), 131–133.

[48] Irifune, T., Nishiyama, N., Kuroda, K., Inoue, T., Isshiki, M., Utsumi, W., Funakoshi, K.-i., Urakawa, S., Uchida, T., Katsura, T., et al. The postspinel phase boundary in Mg_2SiO_4 determined by in situ X-ray diffraction. *Science 279*, 5357 (1998), 1698–1700.

[49] Irifune, T., Shinmei, T., McCammon, C. A., Miyajima, N., Rubie, D. C., and Frost, D. J. Iron partitioning and density changes of pyrolite in Earth's lower mantle. *Science 327*, 5962 (2010), 193–195.

[50] Karki, B. B., Wentzcovitch, R. M., de Gironcoli, S., and Baroni, S. First principles thermoelasticity of $MgSiO_3$-perovskite: Consequences for the inferred properties of the lower mantle. *Geophysical research letters 28*, 14 (2001), 2699–2702.

[51] Katsura, T., Yamada, H., Nishikawa, O., Song, M., Kubo, A., Shinmei, T., Yokoshi, S., Aizawa, Y., Yoshino, T., Walter, M. J., et al. Olivine-wadsleyite transition in the system (Mg, Fe)$_2$SiO$_4$. *Journal of Geophysical Research: Solid Earth 109*, B2 (2004).

[52] Kawai, K., and Tsuchiya, T. P-V-T equation of state of cubic $CaSiO_3$ perovskite from first-principles computation. *Journal of Geophysical Research: Solid Earth 119*, 4 (2014), 2801–2809.

[53] Kawai, K., and Tsuchiya, T. Small shear modulus of cubic $CaSiO_3$ perovskite. *Geophysical Research Letters 42*, 8 (2015), 2718–2726.

[54] Kennett, B., Engdahl, E., and Buland, R. Constraints on seismic velocities in the Earth from traveltimes. *Geophysical Journal International 122*, 1 (1995), 108–124.

[55] Kittel, C. *Introduction to solid state physics.* Wiley, 2005.

[56] Kobayashi, Y., Kondo, T., Ohtani, E., Hirao, N., Miyajima, N., Yagi, T., Nagase, T., and Kikegawa, T. Fe-Mg partitioning between (Mg, Fe)SiO_3 post-perovskite, perovskite, and magnesiowüstite in the earth's lower mantle. *Geophysical Research Letters 32*, 19 (2005).

[57] Kohn, W., and Sham, L. J. Self-consistent equations including exchange and correlation effects. *Physical review 140*, 4A (1965), A1133.

[58] Lin, J.-F., Mao, Z., Yang, J., Liu, J., Xiao, Y., Chow, P., and Okuchi, T. High-spin Fe^{2+} and Fe^{3+} in single-crystal aluminous bridgmanite in the lower mantle. *Geophysical Research Letters 43*, 13 (2016), 6952–6959.

[59] Lin, J.-F., Speziale, S., Mao, Z., and Marquardt, H. Effects of the electronic spin transitions of iron in lower mantle minerals: Implications for deep mantle geophysics and geochemistry. *Reviews of Geophysics 51*, 2 (2013), 244–275.

[60] Mao, W. L., Shen, G., Prakapenka, V. B., Meng, Y., Campbell, A. J., Heinz, D. L., Shu, J., Hemley, R. J., and Mao, H.-k. Ferromagnesian postperovskite silicates in the D" layer of the Earth. *Proceedings of the National Academy of Sciences of the United States of America 101*, 45 (2004), 15867–15869.

[61] Marquardt, H., Speziale, S., Reichmann, H. J., Frost, D. J., Schilling, F. R., and Garnero, E. J. Elastic shear anisotropy of ferropericlase in Earth's lower mantle. *Science 324*, 5924 (2009), 224–226.

[62] Martin, R. M. *Electronic structure: Basic theory and practical methods.* Cambridge university press, 2004.

[63] Masters, G. Observational constraints on the chemical and thermal structure of the Earth's deep interior. *Geophysical Journal International 57*, 2 (1979), 507–534.

[64] Mattern, E., Matas, J., Ricard, Y., and Bass, J. Lower mantle composition and temperature from mineral physics and thermodynamic modelling. *Geophysical Journal International 160*, 3 (2005), 973–990.

[65] Matyska, C., and Yuen, D. A. Profiles of the Bullen's parameter from mantle convection modelling. *Earth and Planetary Science Letters 178*, 1 (2000), 39–46.

[66] Matyska, C., and Yuen, D. A. Bullen's parameter η: A link between seismology and geodynamical modelling. *Earth and Planetary Science Letters 198*, 3 (2002), 471–483.

[67] McDonough, W. F., and Sun, S.-S. The composition of the Earth. *Chemical geology 120*, 3-4 (1995), 223–253.

[68] Metsue, A., and Tsuchiya, T. Thermodynamic properties of (Mg, Fe^{2+}) SiO_3 perovskite at the lower-mantle pressures and temperatures: an internally consistent LSDA+ U study. *Geophysical Journal International 190*, 1 (2012), 310–322.

[69] Momma, K., and Izumi, F. VESTA 3 for three-dimensional visualization of crystal, volumetric and morphology data. *Journal of Applied Crystallography 44*, 6 (2011), 1272–1276.

[70] Murakami, M., Hirose, K., Kawamura, K., Sata, N., and Ohishi, Y. Post-perovskite phase transition in $MgSiO_3$. *Science 304*, 5672 (2004), 855–858.

[71] Murakami, M., Ohishi, Y., Hirao, N., and Hirose, K. A perovskitic lower mantle inferred from high-pressure, high-temperature sound velocity data. *Nature 485*, 7396 (2012), 90–94.

[72] Murakami, M., Sinogeikin, S. V., Bass, J. D., Sata, N., Ohishi, Y., and Hirose, K. Sound velocity of $MgSiO_3$ post-perovskite phase: A constraint on the D" discontinuity. *Earth and Planetary Science Letters 259*, 1 (2007), 18–23.

[73] Nakagawa, T., and Tackley, P. J. Effects of a perovskite-post perovskite phase change near core-mantle boundary in compressible mantle convection. *Geophysical Research Letters 31*, 16 (2004).

[74] Oganov, A. R., and Ono, S. Theoretical and experimental evidence for a post-perovskite phase of $MgSiO_3$ in Earth's D" layer. *Nature 430*, 6998 (2004), 445–448.

[75] Ono, S., and Oganov, A. R. In situ observations of phase transition between perovskite and $CaIrO_3$-type phase in $MgSiO_3$ and pyrolitic mantle composition. *Earth and Planetary Science Letters 236*, 3 (2005), 914–932.

[76] Piet, H., Badro, J., Nabiei, F., Dennenwaldt, T., Shim, S.-H., Cantoni, M., Hébert, C., and Gillet, P. Spin and valence dependence of iron partitioning in Earth's deep mantle. *Proceedings of the National Academy of Sciences* (2016), 201605290.

[77] Poirier, J.-P. *Introduction to the Physics of the Earth's Interior.* Cambridge University Press, 2000.

[78] Sadd, M. H. *Elasticity: theory, applications, and numerics.* Academic Press, 2009.

[79] Sakai, T., Ohtani, E., Terasaki, H., Miyahara, M., Nishijima, M., Hirao, N., Ohishi, Y., and Sata, N. Fe–Mg partitioning between post-perovskite and ferropericlase in the lowermost mantle. *Physics and Chemistry of minerals 37*, 7 (2010), 487–496.

[80] Shieh, S. R., Duffy, T. S., Kubo, A., Shen, G., Prakapenka, V. B., Sata, N., Hirose, K., and Ohishi, Y. Equation of state of the postperovskite phase synthesized from a natural (Mg, Fe)SiO_3 orthopyroxene. *Proceedings of the National Academy of Sciences of the United States of America 103*, 9 (2006), 3039–3043.

[81] Shim, S.-H., Duffy, T., Jeanloz, R., and Shen, G. Stability and crystal structure of $MgSiO_3$ perovskite to the core-mantle boundary. *Geophysical Research Letters 31*, 10 (2004).

[82] Shukla, G., Cococcioni, M., and Wentzcovitch, R. M. Thermoelasticity of Fe^{3+}- and Al-bearing bridgmanite: Effects of iron spin crossover. *Geophysical Research Letters 43*, 11 (2016), 5661–5670.

[83] Shukla, G., Topsakal, M., and Wentzcovitch, R. M. Spin crossovers in iron-bearing $MgSiO_3$ and $MgGeO_3$: Their influence on the post-perovskite transition. *Physics of the Earth and Planetary Interiors 249* (2015), 11–17.

[84] Shukla, G., Valencia-Cardona, J. J., and Wentzcovitch, R. M. Thermoelasticity of iron- and aluminum-bearing $MgSiO_3$ post-perovskite. *Journal of Geophysical Research: Solid Earth N/A* (2018), N/A.

[85] Shukla, G., and Wentzcovitch, R. M. Spin crossover in (Mg, Fe^{3+})(Si, Fe^{3+})O_3 bridgmanite: Effects of disorder, iron concentration, and temperature. *Physics of the Earth and Planetary Interiors 260* (2016), 53–61.

[86] Shukla, G., Wu, Z., Hsu, H., Floris, A., Cococcioni, M., and Wentzcovitch, R. M. Thermoelasticity of Fe^{2+}-bearing bridgmanite. *Geophysical Research Letters 42*, 6 (2015), 1741–1749.

[87] Sidorin, I., Gurnis, M., Helmberger, D. V., and Ding, X. Interpreting D” seismic structure using synthetic waveforms computed from dynamic models. *Earth and planetary science letters 163*, 1 (1998), 31–41.

[88] Sinmyo, R., Hirose, K., Nishio-Hamane, D., Seto, Y., Fujino, K., Sata, N., and Ohishi, Y. Partitioning of iron between perovskite/postperovskite and ferropericlase in the lower mantle. *Journal of Geophysical Research: Solid Earth 113*, B11 (2008).

[89] Speziale, S., Milner, A., Lee, V., Clark, S., Pasternak, M., and Jeanloz, R. Iron spin transition in Earth’s mantle. *Proceedings of the National Academy of Sciences of the United States of America 102*, 50 (2005), 17918–17922.

[90] Stixrude, L., and Lithgow-Bertelloni, C. Thermodynamics of mantle mineralsI. Physical properties. *Geophysical Journal International 162*, 2 (2005), 610–632.

[91] Stixrude, L., and Lithgow-Bertelloni, C. Thermodynamics of mantle minerals-II. Phase equilibria. *Geophysical Journal International 184*, 3 (2011), 1180–1213.

[92] Sun, N., Mao, Z., Yan, S., Wu, X., Prakapenka, V. B., and Lin, J.-F. Confirming a pyrolitic lower mantle using self-consistent pressure scales and new constraints on $CaSiO_3$ perovskite. *Journal of Geophysical Research: Solid Earth 121*, 7 (2016), 4876–4894.

[93] Tateno, S., Hirose, K., Sata, N., and Ohishi, Y. Phase relations in $Mg_3Al_2Si_3O_{12}$ to 180 GPa: Effect of Al on post-perovskite phase transition. *Geophysical Research Letters 32*, 15 (2005).

[94] Tateno, S., Hirose, K., Sata, N., and Ohishi, Y. Solubility of Feo in (Mg, Fe)SiO_3 perovskite and the post-perovskite phase transition. *Physics of the Earth and Planetary Interiors 160*, 3 (2007), 319–325.

[95] Tateno, S., Hirose, K., Sata, N., and Ohishi, Y. Determination of post-perovskite phase transition boundary up to 4400 K and implications for thermal structure in D" layer. *Earth and Planetary Science Letters 277*, 1 (2009), 130–136.

[96] Thomas, C., Kendall, J.-M., and Lowman, J. Lower-mantle seismic discontinuities and the thermal morphology of subducted slabs. *Earth and Planetary Science Letters 225*, 1 (2004), 105–113.

[97] Tsuchiya, J., and Tsuchiya, T. Postperovskite phase equilibria in the $MgSiO_3$–Al_2O_3 system. *Proceedings of the National Academy of Sciences 105*, 49 (2008), 19160–19164.

[98] Tsuchiya, T., Kawai, K., Wang, X., Ichikawa, H., and Dekura, H. Temperature of the lower mantle and core based on ab initio mineral physics data. *Deep Earth: Physics and Chemistry of the Lower Mantle and Core* (2016), 13–30.

[99] Tsuchiya, T., Tsuchiya, J., Umemoto, K., and Wentzcovitch, R. M. Phase transition in $MgSiO_3$ perovskite in the Earth's lower mantle. *Earth and Planetary Science Letters 224*, 3 (2004), 241–248.

[100] Tsuchiya, T., Wentzcovitch, R. M., da Silva, C. R., and de Gironcoli, S. Spin transition in magnesiowüstite in earths lower mantle. *Physical Review Letters 96*, 19 (2006), 198501.

[101] Valencia-Cardona, J. J., Shukla, G., Wu, Z., Houser, C., Yuen, D. A., and Wentzcovitch, R. M. Influence of the iron spin crossover in ferropericlase on the lower mantle geotherm. *Geophysical Research Letters 44*, 10 (2017), 4863–4871.

[102] Valencia-Cardona, J. J., Williams, Q., Shukla, G., and Wentzcovitch, R. M. Bullen's parameter as a seismic observable for spin crossovers in the lower mantle. *Geophysical Research Letters 44*, 18 (2017), 9314–9320.

[103] Vilella, K., Shim, S.-H., Farnetani, C. G., and Badro, J. Spin state transition and partitioning of iron: Effects on mantle dynamics. *Earth and Planetary Science Letters 417* (2015), 57–66.

[104] Wang, X., Tsuchiya, T., and Hase, A. Computational support for a pyrolitic lower mantle containing ferric iron. *Nature Geoscience 8*, 7 (2015), 556–559.

[105] Watt, J. P., Davies, G. F., and O'Connell, R. J. The elastic properties of composite materials. *Reviews of Geophysics 14*, 4 (1976), 541–563.

[106] Wentzcovitch, R., Justo, J., Wu, Z., da SILVA, C. R., Yuen, D., and Kohlstedt, D. Anomalous compressibility of ferropericlase throughout the iron spin crossover. *Proceedings of the National Academy of Sciences 106*, 21 (2009), 8447–8452.

[107] Wentzcovitch, R., and Stixrude, L. *Theoretical and computational methods in mineral physics: Geophysical applications*, vol. 71. Mineral Soc America, 2010.

[108] Wentzcovitch, R. M., Tsuchiya, T., and Tsuchiya, J. $MgSiO_3$ postperovskite at D" conditions. *Proceedings of the National Academy of Sciences of the United States of America 103*, 3 (2006), 543–546.

[109] Williams, Q., and Knittle, E. The uncertain major element bulk composition of Earth's mantle. *Earth's Deep Mantle: Structure, Composition, and Evolution* (2005), 187–199.

[110] Wu, Z. Velocity structure and composition of the lower mantle with spin crossover in ferropericlase. *Journal of Geophysical Research: Solid Earth 121*, 4 (2016), 2304–2314.

[111] Wu, Z., Justo, J., da Silva, C., de Gironcoli, S., Wentzcovitch, R., et al. Anomalous thermodynamic properties in ferropericlase throughout its spin crossover. *Physical Review B 80*, 1 (2009), 014409.

[112] Wu, Z., Justo, J. F., and Wentzcovitch, R. M. Elastic anomalies in a spin-crossover system: Ferropericlase at lower mantle conditions. *Physical review letters 110*, 22 (2013), 228501.

[113] Wu, Z., and Wentzcovitch, R. M. Spin crossover in ferropericlase and velocity heterogeneities in the lower mantle. *Proceedings of the National Academy of Sciences 111*, 29 (2014), 10468–10472.

[114] Wysession, M. E., Lay, T., Revenaugh, J., Williams, Q., Garnero, E. J., Jeanloz, R., and Kellogg, L. H. The D" discontinuity and its implications. *The core-mantle boundary region* (1998), 273–297.

[115] Ye, Y., Gu, C., Shim, S.-H., Meng, Y., and Prakapenka, V. The postspinel boundary in pyrolitic compositions determined in the laser-heated diamond anvil cell. *Geophysical Research Letters 41*, 11 (2014), 3833–3841.

Appendix A

Appendix

A.1 Appendix Adiabats

Text 1. We compared the pyrolite's adiabat properties when its fp ($\sim$ 31 mol% in pyrolite) did (MS) and did not (HS) undergo spin transition. Figure A.1 shows pyrolite's α, C_p and V calculated along its own geotherm. Compression curves differences are subtle (Figure A.1a), while the anomalies introduced in α and C_p (Figures A.1b and A.1c respectively) caused broad peaks throughout the spin crossover at equivalent pressure ranges.

Text 2. Elastic moduli, velocities, and densities of the minerals in each aggregate, calculated along the aggregate geotherm, can be found in Figures A.2, A.3, and A.4. It can be observed that K_S for bdg and CaPv behave similarly, but CaPv shear modulus G is significantly smaller than that of bdg. In all aggregates, K_S for both perovskites is larger than PREM values. G for bdg displays values greater than PREM, while CaPv G agrees well until mid lower mantle pressures, and then deviates to values smaller than those of PREM. Finally, moduli for fp are always smaller than PREM values and showed clear anomalies associated with spin crossover. The velocities followed a trend consistent with that of the moduli, while for the densities we observed that CaPv is denser than bdg. Also, fp increases its density at mid lower mantle pressures due the volume collapse caused by the spin crossover.

Text 3. Isentropes for CaPv were calculated using [91] MDG parameters, which are different from those obtained by [52] and by [92](See Figure A.5a). They differ by $\sim$

100 K from each other in the deep lower mantle (125 GPa). Figure A.5b shows pyrolite adiabats using different CaPv. The thermodynamic model adopted for CaPv had little influence on the geotherm. We used CaPv properties reported by [52, 53] for all the aggregates. Figure A.6 shows the elastic constants of CaPv for different isotherms

Text 4.

To address the change in partitioning K_D, the adiabats for compositions containing fp were calculated with a K_D value of 0.25 (See Figure A.7). Temperature differences between the latter and those with a K_D of 0.5 were $\sim$ 9 K, 13 K, 14 K, and 16 K for chondrite, harzburgite, peridotite, and pyrolite at 125 GPa, respectively . The hotter values were a consequence of the higher iron content in fp due the reduced partitioning from 0.5 to 0.25. Furthermore, pyrolite adiabats were calculated with different types of bdg, namely: Fe^{2+},(Fe^{2+},Al)-,and (Fe^{3+},Al)- bearing bdg (See Figure A.8). The latter corresponds to a limiting case, which assumes that all the iron in bdg is ferric and that also that it enters in the B-site (Si site) where the spin crossover takes place. The spin crossover in ferric iron will also impact the adiabat in this case. At 125 GPa, spin crossover in bdg increases the temperature by $\sim$ 13 K.

A.2 Appendix PPv-Pv transition

Text 1

Figure A.10 depicts the boundaries for the $MgSiO_3$ system compared with previous calculations [99] and experiments [70]. Furthermore, Figure A.11 shows the changes in the acoustic velocities and densities across the phase transition along the Boheler [12] geotherm. Shaded areas represent the difference between LDA and GGA boundaries. With the exception of Fe^{2+} case, paired discontinuities are observed. This double crossing phenomena is caused by the superadiabatic temperature gradient of Boheler [12].

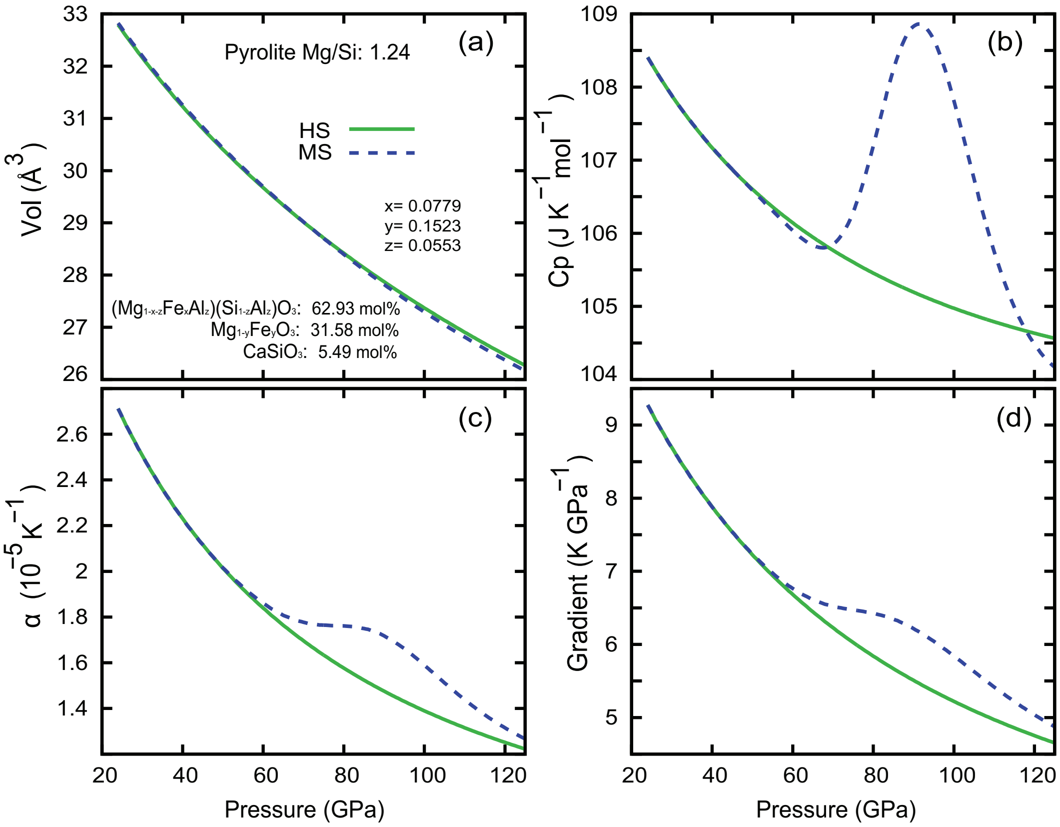

Figure A.1: Properties of pyrolite with ferropericlase in high spin state (HS) and mixed spin (MS) state along its own adiabat. (a) Volume, (b) thermal expansion coefficient, (c) isobaric specific heat and (d) adiabatic gradient.

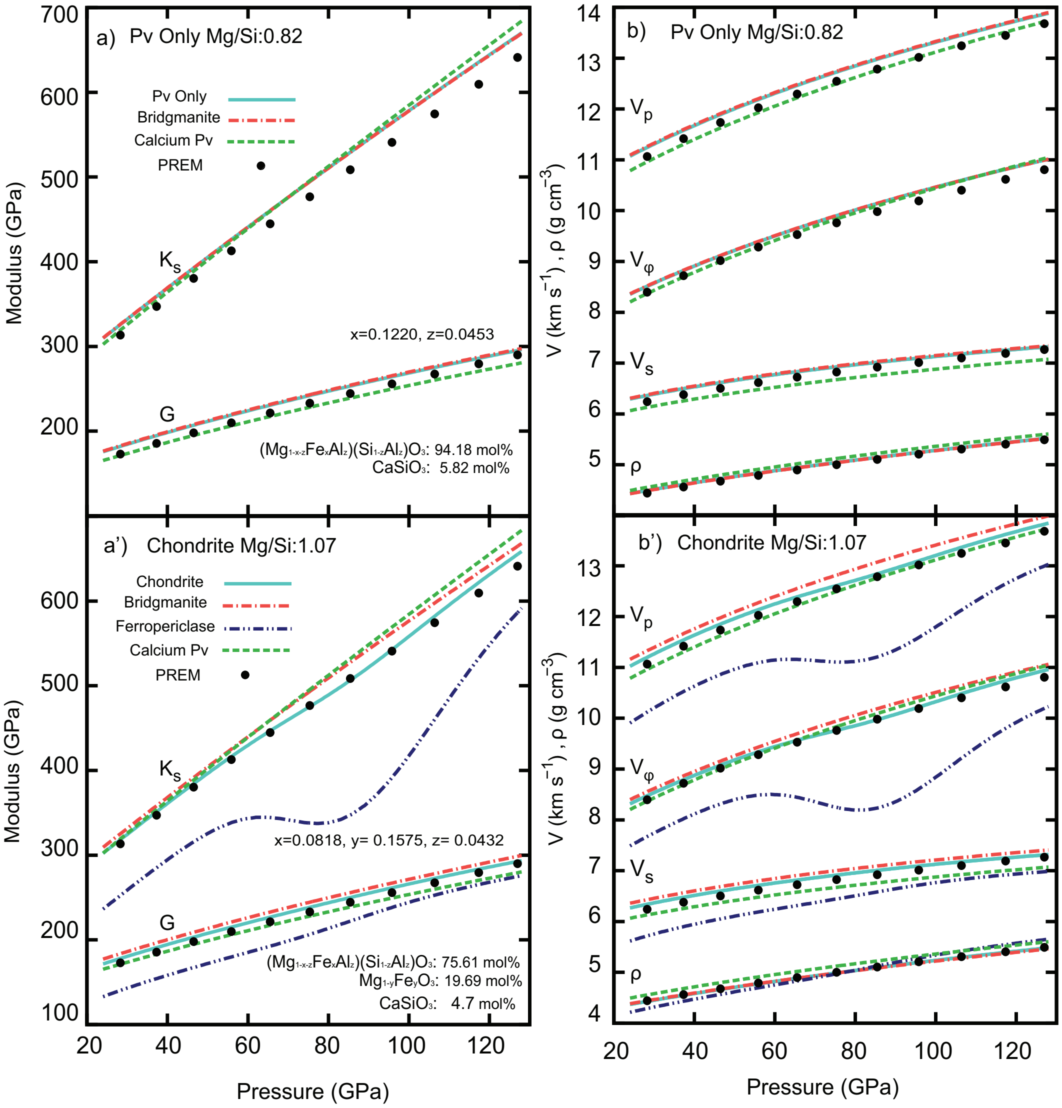

Figure A.2: (a) and (a') are the elastic moduli (K_S, G) for Pv Only and chondritic aggregates respectively, while (b) and (b') are the acoustic velocities (V_P, V_ϕ, and V_S) and densities (ρ). The solid/dashed lines represent the aggregate/mineral properties.

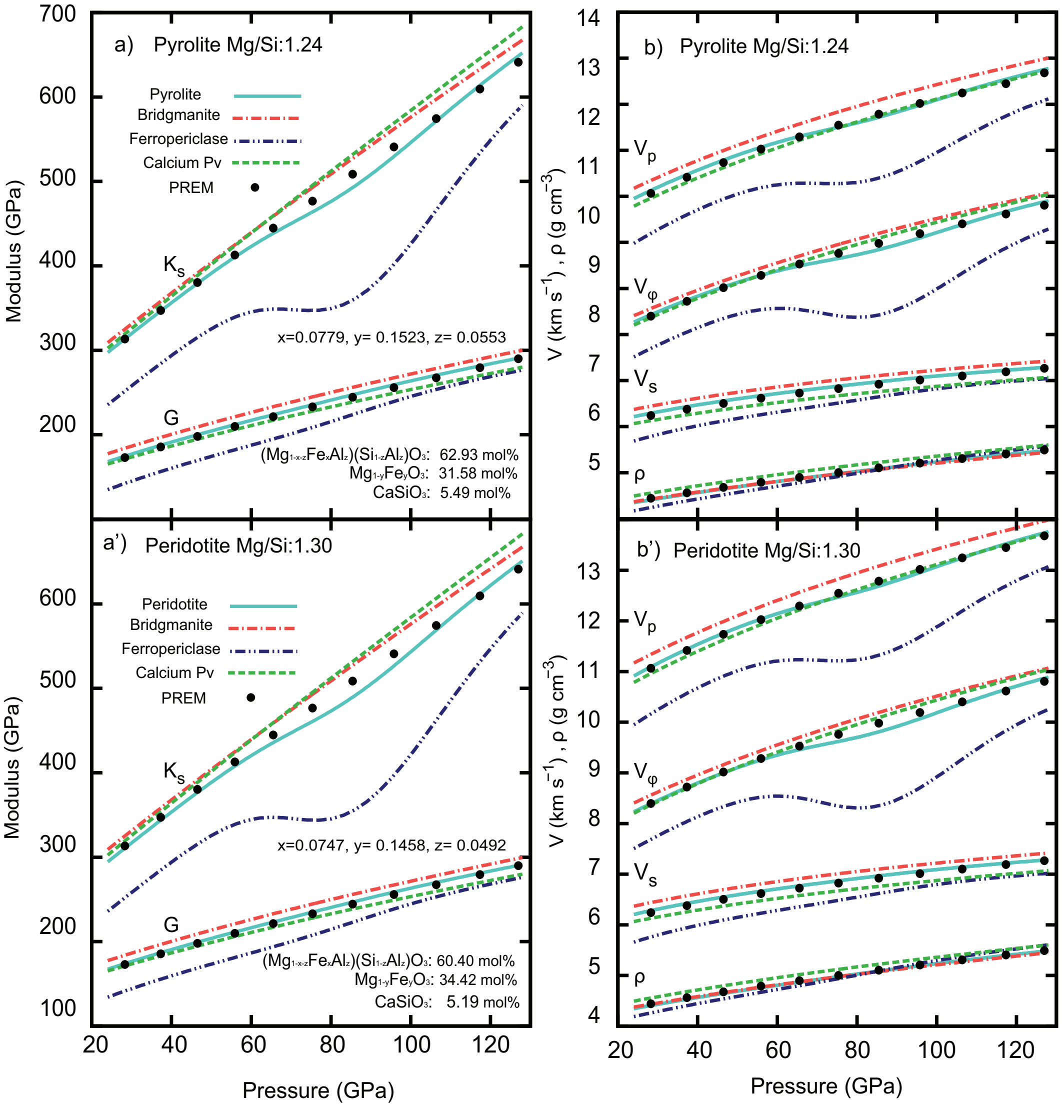

Figure A.3: (a) and (a') are the elastic moduli (K_S, G) for pyrolite and peridotite compositions respectively, while (b) and (b') are the acoustic velocities (V_P, V_ϕ, and V_S) and densities (ρ). The solid/dashed lines represent the aggregate/mineral properties.

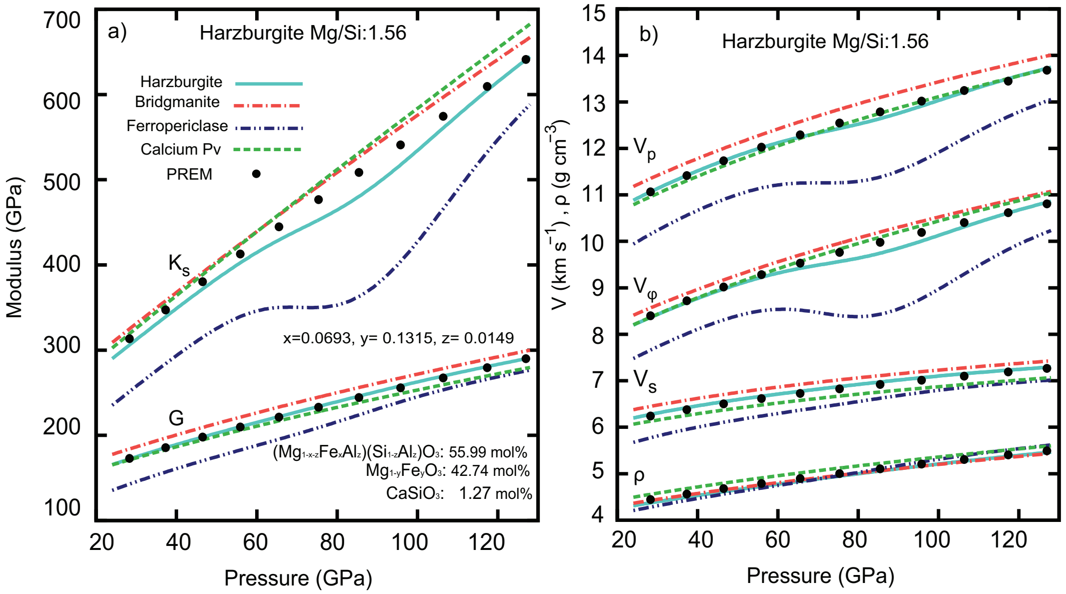

Figure A.4: (a) Elastic moduli (K_S, G), (b) acoustic velocities (V_P, V_ϕ, and V_S), and densities (ρ) for harzburgite. The solid/dashed lines represent the aggregate/mineral properties.

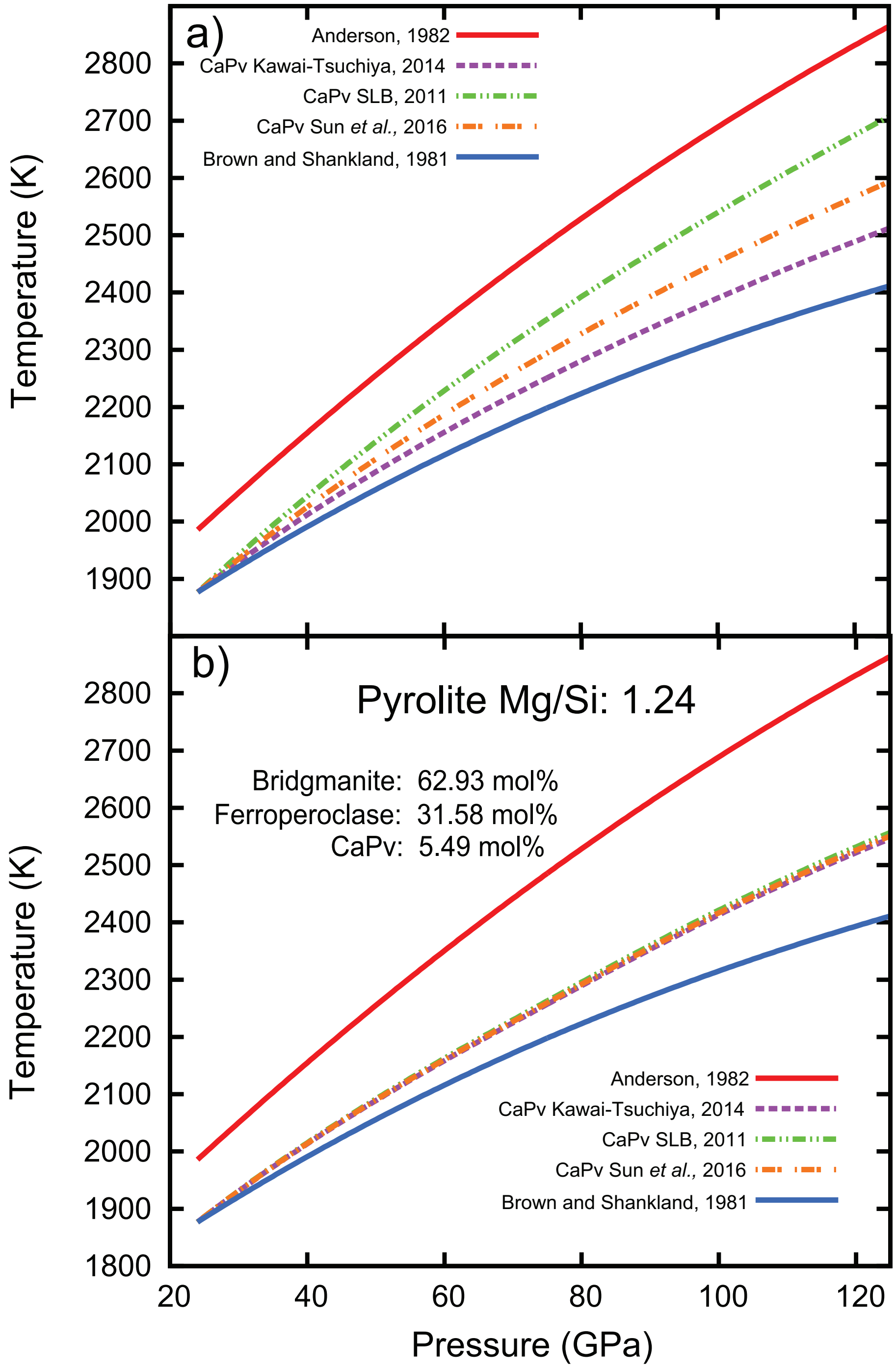

Figure A.5: (a) Calculated $CaSiO_3$ adiabats using MDG parameters from [91] (SLB), [92], and [52]. (b) Pyrolite adiabats using $CaSiO_3$ from [91] (SLB), [92], and [52].

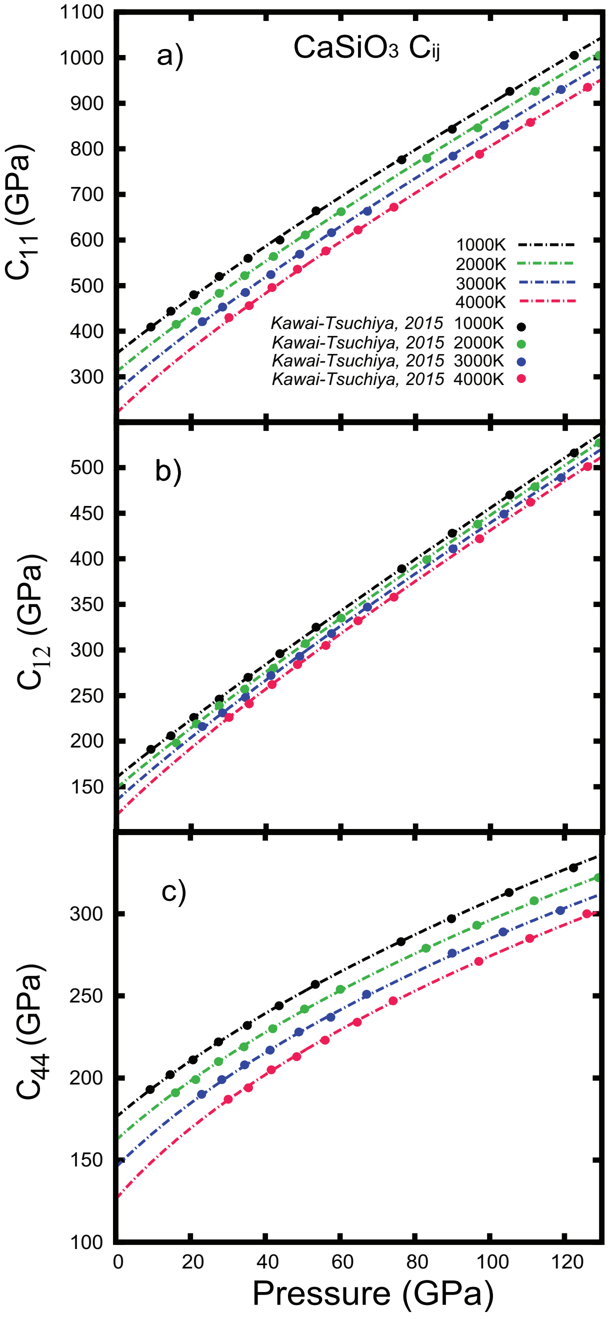

Figure A.6: Results by [53] fitted to a Mie-Debye-Grüneisen model developed in [90] (See equation 2 in [53]).

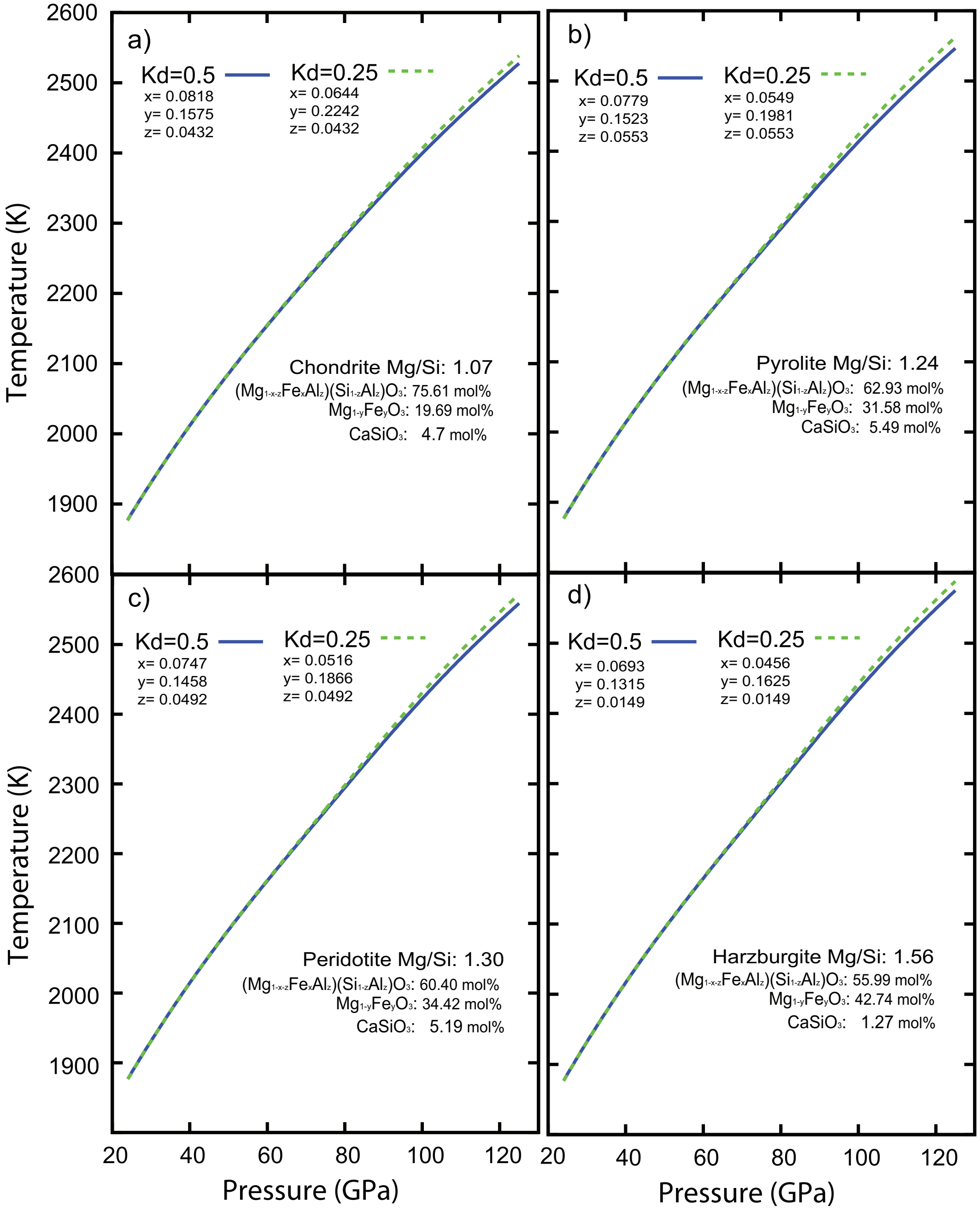

Figure A.7: Adiabats for (a) chondrite, (b) pyrolite, (c) peridotite, and (d) harzburgite with different partitioining K_D. Solid(blue)/dashed(green) lines correspond to partitioning coefficients of 0.5 and 0.25 respectively.

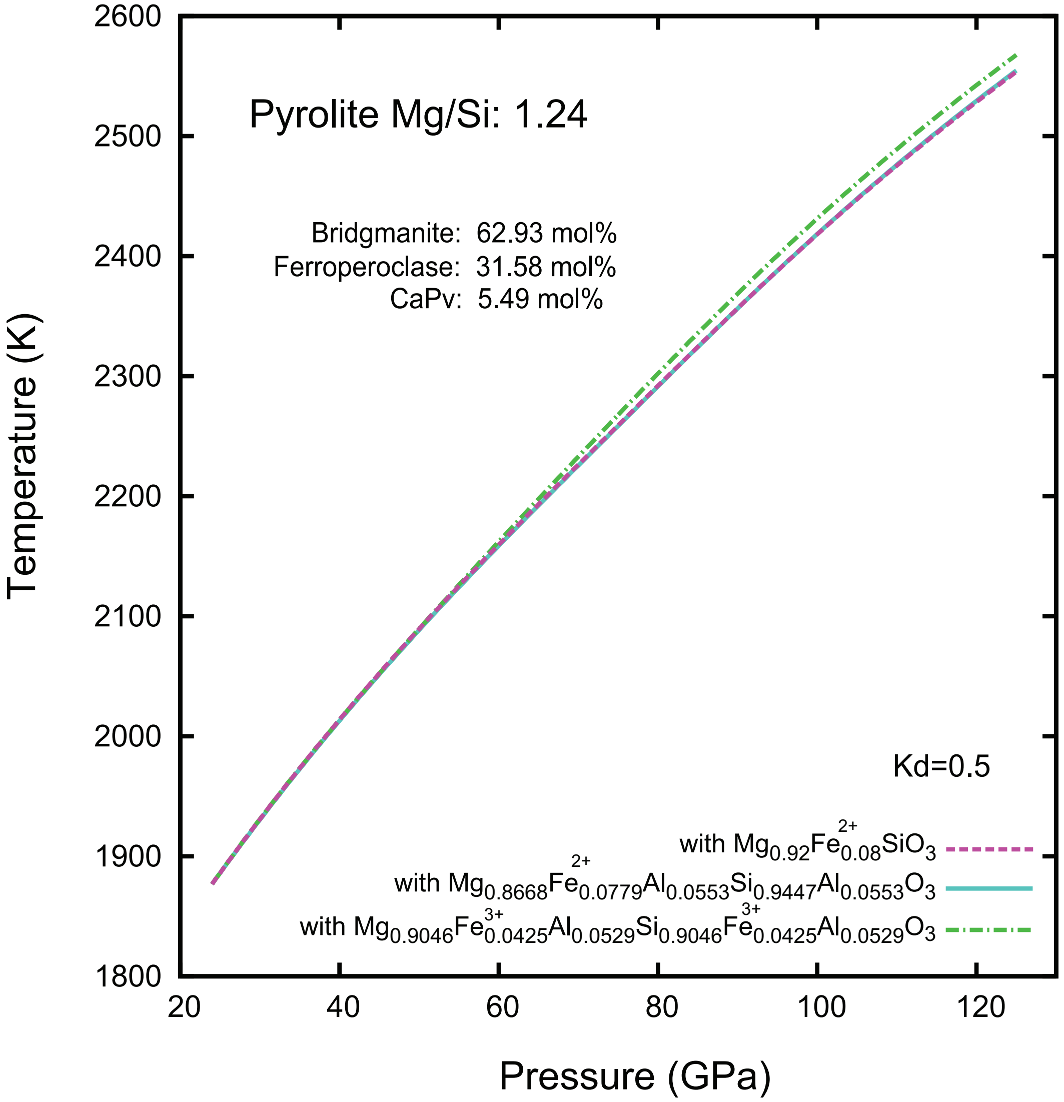

Figure A.8: Pyrolite adiabats with Fe^{2+},(Fe^{2+},Al)-,and (Fe^{3+},Al)- bearing bridgmanite.

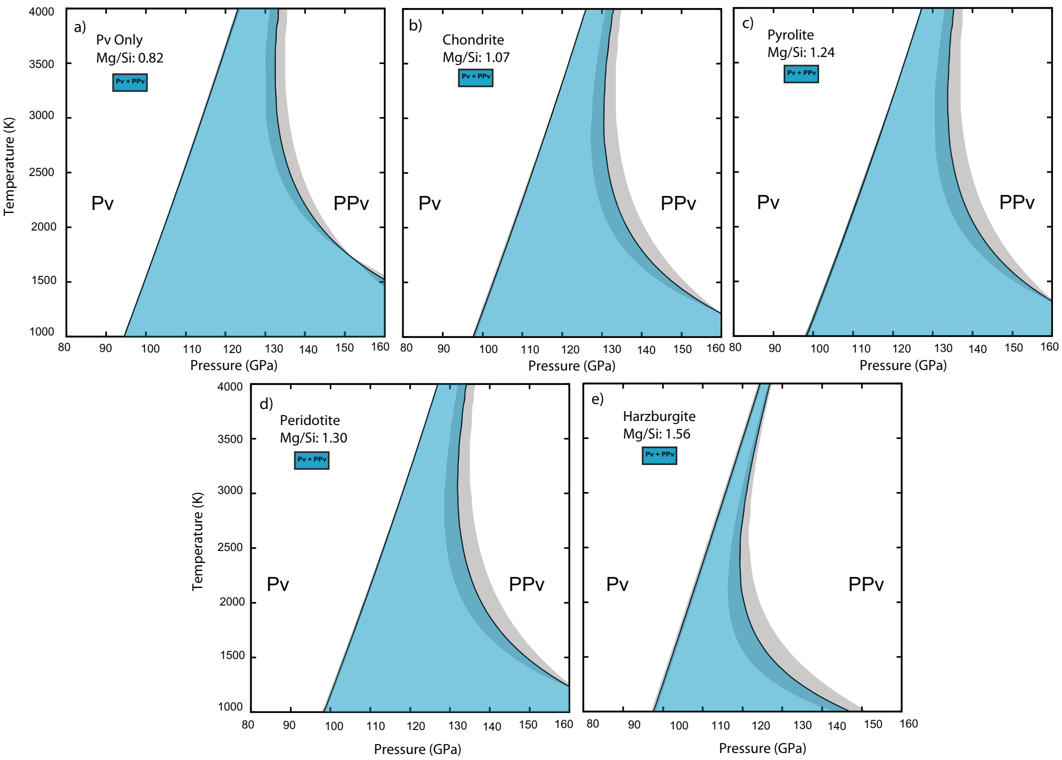

Figure A.9: Phase boundaries for lower mantle aggregates. Gray shaded areas around the boundary indicate the uncertainites. Blue shaded areas depict the coexistence region between Pv and PPv phases.

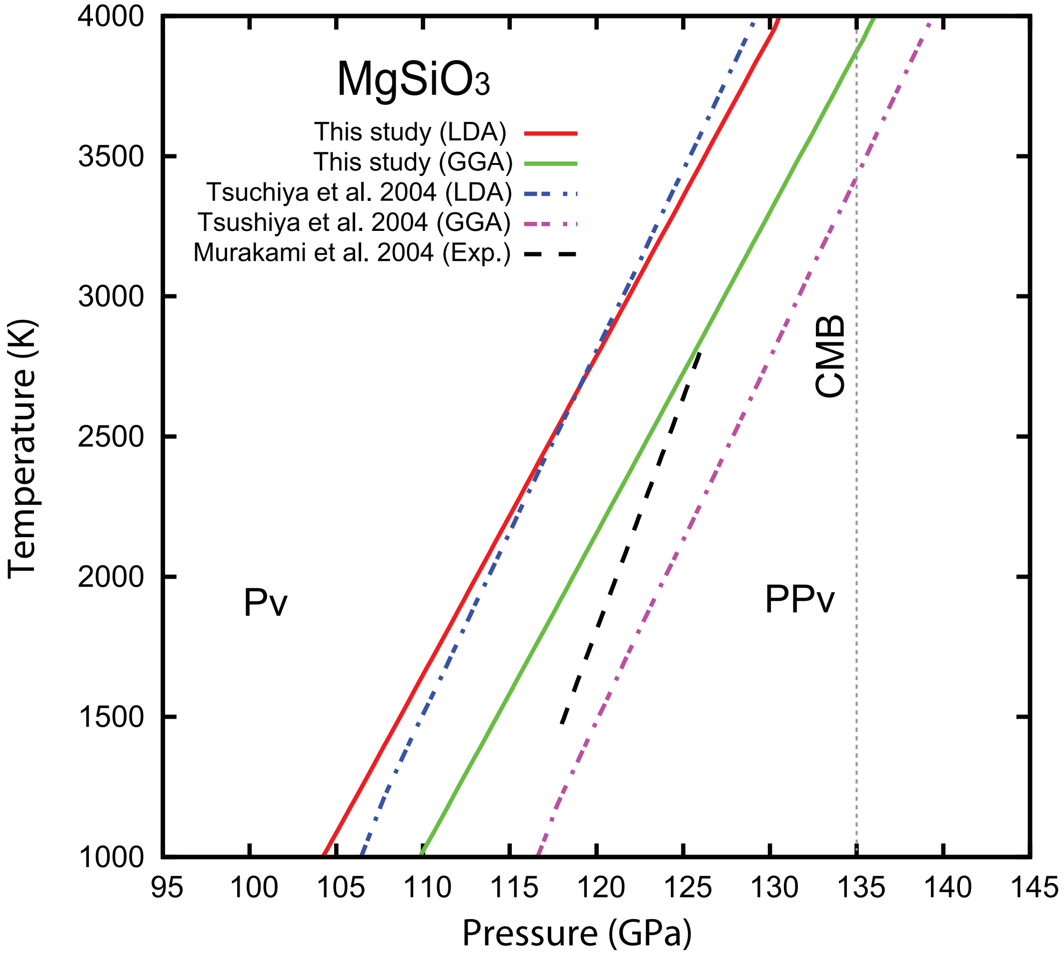

Figure A.10: LDA and GGA phase boundaries compared with calculations by [99] and experiments by [70].

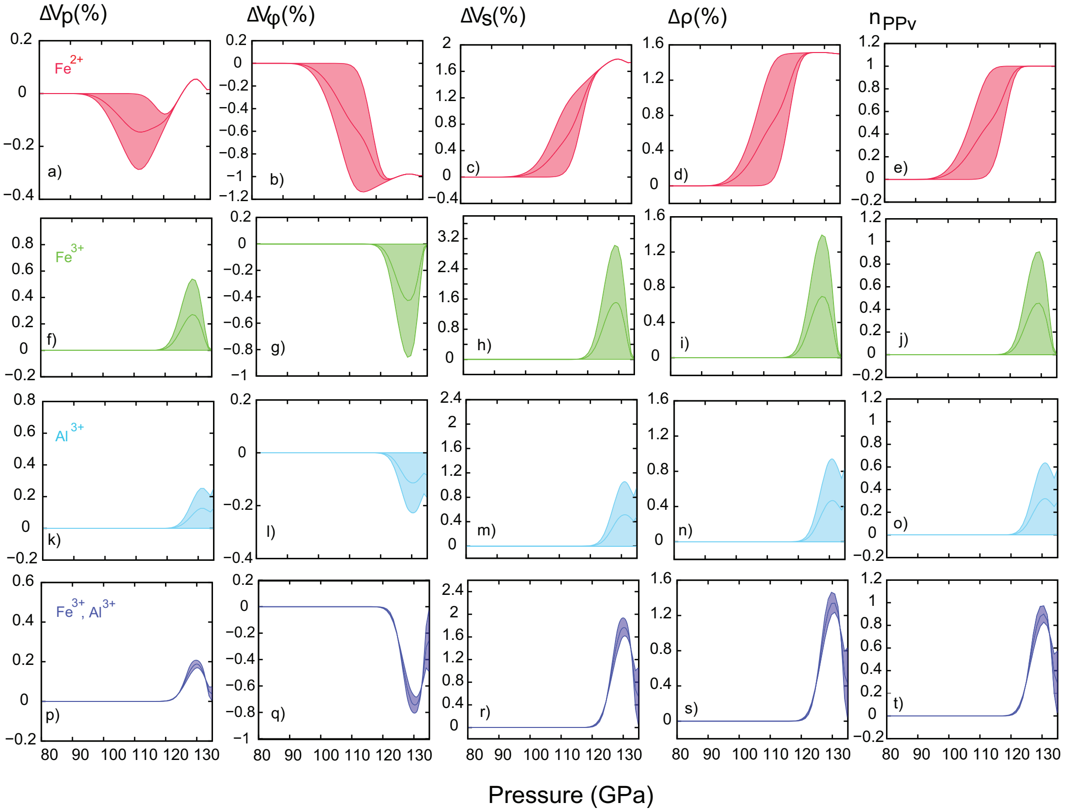

Figure A.11: Calculated contrasts $\Delta V_P(\%)$, $\Delta V_\phi(\%)$, $\Delta V_S(\%)$, $\Delta\rho(\%)$ and PPv fraction (n_{PPv}) in $Mg_{1-x}Fe^{2+}_xSiO_3$, $(Mg_{1-x}Fe^{3+}_x)(Si_{1-x}Fe^{3+}_x)O_3$, $(Mg_{1-x}Al_x)(Si_{1-x}Al_x)O_3$, and $(Mg_{1-x}Fe^{3+}_x)(Si_{1-x}Al_x)O_3$, respectively, with x=0.10. The contrasts are calculated along the Boehler Boehler temperature profile as: $\Delta M = 100 * (M_{agg} - M_{PV})/M_{PV}$, with M as: V_P, V_ϕ, V_S, and ρ.